NASA TECHNICAL NOTE

NASA TN D-2942

NASA TN D-2942

FAVORABLE INTERFERENCE EFFECTS ON MAXIMUM LIFT-DRAG RATIOS OF HALF-CONE DELTA-WING CONFIGURATIONS AT MACH 6.86

by David E. Fetterman

Langley Research Center

Langley Station, Hampton, Va.

NATIONAL AERONAUTICS AND SPACE ADMINISTRATION • WASHINGTON, D. C. • AUGUST 1965

NASA TN D-2942

FAVORABLE INTERFERENCE EFFECTS ON MAXIMUM LIFT-DRAG RATIOS OF HALF-CONE DELTA-WING CONFIGURATIONS AT MACH 6.86

By David E. Fetterman

Langley Research Center
Langley Station, Hampton, Va.

NATIONAL AERONAUTICS AND SPACE ADMINISTRATION

For sale by the Clearinghouse for Federal Scientific and Technical Information
Springfield, Virginia 22151 – Price $3.00

FAVORABLE INTERFERENCE EFFECTS ON MAXIMUM LIFT-DRAG RATIOS OF HALF-CONE DELTA-WING CONFIGURATIONS AT MACH 6.86

By David E. Fetterman
Langley Research Center

SUMMARY

The characteristics of half-cone delta-wing configurations is investigated under predominantly laminar boundary-layer conditions at a Mach number of 6.86 and Reynolds number based on model length of 1.43×10^6 to determine the availability of favorable interference effects for improving the maximum lift-drag ratio $(L/D)_{max}$. Simple modification to the half-cone body to provide more volume and better volume distribution are also considered. Approximate solutions for the characteristics of half-cone winged configurations are included in the appendixes.

The results indicate that only under certain criteria are favorable interference effects sufficient to cause the $(L/D)_{max}$ obtained by flat-top configurations to be superior to those obtained by flat-bottom configurations. Presently available theoretical methods are found to be inadequate to predetermine either the superiorities in flat-top $(L/D)_{max}$ due to favorable interference or the conditions under which they occur; however, experimentally determined configuration criteria for which these benefits appear to be available are established herein. Modifications to these half-cone delta-wing configurations decreased the $(L/D)_{max}$ for both flat-top and flat-bottom configurations and caused rapid deterioration in favorable interference benefits.

INTRODUCTION

A practical means of obtaining favorable interference benefits on maximum lift-drag ratios at high speeds was suggested by Eggers and Syvertson in reference 1. Their scheme employs a half-body—wing combination wherein the wing receives additional lift from the superimposed flow field from the body mounted beneath the wing. Optimum configurations are therefore obtained when the wing leading edge and body shock coincide.

To determine whether favorable interference benefits are being obtained by use of these so-called "flat-top" configurations, it is customary to compare

their results with those obtained with the use of configurations in the inverted or "flat-bottom" position. With this approach, experimental verification of the concept has been obtained in certain investigations (refs. 1 to 4) whereas in other investigations (refs. 5 and 6) negative results have been obtained. When plotted against free-stream Mach number, the maximum lift-drag data from these references tend to indicate that favorable interference benefits dissipate with Mach number and disappear entirely at about Mach number 12. Furthermore, confusing results exist at certain Mach numbers where some configurations show favorable interference benefits whereas others do not. Although it is true that many of the configurations of these investigations are not optimum, most of them, on the basis of available information, would be expected, a priori, to show some evidence of favorable interference benefits.

Since explanations of the observed behavior are not available in the literature, investigations have been undertaken at the Langley Research Center to attempt to gain additional insight into the favorable interference problem and to establish criteria which will enable the benefits to be extended to higher Mach numbers. A summary of pertinent results obtained to date from these investigations is presented in references 7 and 8. The purpose of this paper is to present the detailed results obtained from the investigation devoted to half-cone delta-wing configurations at a Mach number of 6.86 in air. Detailed results for a similar series of configurations at a Mach number of 20 in helium are presented in reference 9.

As a final remark it must be noted that the configurations of reference 4 contained misalinements (about 1°) between the force balance axis and the model angle-of-attack reference plane which were not corrected for in the final data. Because of the direction of these misalinements, the measured maximum lift-drag ratio data of reference 4 are slightly lower for the flat-top configurations and slightly higher for the flat-bottom configurations than those presented. These misalinements, therefore, do not significantly affect those comparisons in reference 4, that pertain to models with the wing in a given position; however, those comparisons that pertain to the relative performance of flat-top and flat-bottom configurations are sufficiently affected to provide an unreliable evaluation of favorable interference effects.

SYMBOLS

F_A	axial force
a	cone length on cone cylinder (see fig. 1)
b	wing span
C_A	axial-force coefficient, $\frac{F_A}{qS_p}$
$C_{A,0}$	axial-force coefficient at $\alpha = 0^\circ$

C_D	drag coefficient, $\frac{D}{qS_p}$
$C_{D,b,w}$	wing base drag coefficient, $\frac{1}{M^2}\frac{S_{b,w}}{S_p}$
$C_{D,0}$	drag coefficient at $\alpha = 0^\circ$
$C_{D,p}$	inviscid pressure drag coefficient
$C_{F,d}$	friction drag coefficient due to boundary-layer displacement
$C_{F,i}$	friction drag coefficient without displacement effects
C_L	lift coefficient, $\frac{L}{qS_p}$
$C_{L(L/D)_{max}}$	lift coefficient at maximum lift-to-drag ratio
C_m	pitching-moment coefficient, $\frac{M_Y}{qS_p\bar{c}}$
C_N	normal-force coefficient, $\frac{F_N}{qS_p}$
$C_{N,0}$	normal-force coefficient at $\alpha = 0^\circ$
C_p	pressure coefficient, $\frac{p - p_\infty}{q_\infty}$
$\bar{c}$	mean aerodynamic chord
d	wing dimension (see fig. 1)
D	drag
h	wing leading-edge height
L	lift
l	model length
$(L/D)_{max}$	maximum lift-drag ratio

M	Mach number
M_Y	pitching moment
M'_w	wing local Mach number
F_N	normal force
p	pressure
q	dynamic pressure
R_l	Reynolds number based on model length
r_b	base radius of body
$S_{b,w}$	base area of wing
S_p	reference area (planform)
t	maximum wing thickness
V	total internal volume (including wings)
x	location of neutral point from configuration apex
y_{le}	leading-edge spanwise location (see fig. 19)
y_s	cone-shock spanwise location (see fig. 19)
α	angle of attack, referenced to flat surface of wing or body
α_{SD}	angle of attack for leading-edge shock detachment
$\alpha_{(L/D)_{max}}$	angle of attack at maximum lift-drag ratio
δ	wing wedge angle
θ	cone semiapex angle
θ_s	cone shock angle
τ	cone offset angle
Λ	wing leading-edge sweep angle
ϵ	wing leading-edge semiapex angle

ϕ	cone radial angle (referenced from cone windward ray)
γ	ratio of specific heats

Subscripts:

0, 1, 2, 3	spanwise stations on configuration (see fig. 19)
b	base
B	body
c	cone
fp	flat-plate portion of wing following wedge
l	lower
le	leading edge
u	upper
w	wing
∞	free stream

Abbreviations:

l.e.	leading edge
FB	flat-bottom orientation (wing on bottom)
FT	flat-top orientation (wing on top)

APPARATUS AND TESTS

The tests were conducted in the Langley 11-inch hypersonic tunnel. The nozzle, which is two-dimensional and constructed of invar to reduce thermal expansion effects, provided a Mach number of about 6.86 at the conditions of the tests. A calibration of the invar nozzle can be obtained from reference 10 and further details of the Langley 11-inch hypersonic tunnel may be found in references 11 and 12.

Most of the tests were performed on half-cone delta-wing combinations obtained by combining the various basic components for which the geometric properties are shown in figure 1. For these half-cone delta-wing combinations, the wing leading-edge sweep angles ranged from 65° to 85° with half-cone angles of 3° to 9° as indicated in the table in figure 1. A few tests were also made to determine the effects of offsetting the cone axis from the wing plane, as

was done in references 1, 2, and 4. The models for these tests consisted of a 5° half-cone offset 1°, 2°, or 3° from a 75° swept leading-edge delta wing by means of the wedge sections shown in figure 1. In addition, a series of tests were also performed to determine the effects of providing a more favorable body-volume distribution than that afforded by a half-cone. For these tests, bodies were formed by varying the cylindrical afterbody lengths on the constant-volume constant-length half-cone-cylinder combinations shown in figure 1. These bodies were tested alone and also with 81° and 75° swept delta wings.

All delta wings had wedge-slab sections with a 1° wedge angle in the streamwise plane and square leading edges with a height of about 0.01 inch. For the model lengths considered, these heights result in h/l values ranging from about 1/500 to 1/800.

All models were tested with wing on top (designated flat top) and inverted (designated flat bottom) to determine their optimum attitude. Body-alone tests, which did not include the flat-side bevel present on the winged configurations, were also conducted in similar upright and inverted positions.

The tests were conducted at a stagnation temperature of 1110° R and various stagnation pressures, depending on model length, to give a constant Reynolds number based on length for all models. The test conditions chosen result in an average Reynolds number of 1.43×10^6. A few tests on representative configurations were also made over a range of Reynolds numbers to determine the boundary-layer conditions existing over the models. The Reynolds numbers of these tests ranged from 0.26×10^6 to 1.43×10^6. Water-condensation effects were prevented by keeping the absolute humidity of the air less than 1.87×10^{-5} pounds of water per pound of dry air for all tests.

Forces and moments on the models were measured by a water-cooled external three-component strain-gage balance. The balance sting was shielded to within 0.040 inch of the model base in all tests to eliminate forces and moments on the balance sting. Body base pressures were measured during all tests, and adjustments to the axial forces were made to correct these pressures to free-stream pressure. Wing base pressures were not measured; however, because of the thinness of the wing, the effects of these pressures should be small.

The model angle of attack was set by means of an optical system wherein a small prism embedded in the body surface reflected a beam of light onto a calibrated screen. With this system, the true model angle of attack was obtained irrespective of balance deflection due to load.

The uncertainty in angle of attack was $\pm 0.2^\circ$ and in Mach number ± 0.01. The errors in the data resulting from these uncertainties and those associated with measuring the forces, moments, and base pressures on the models are estimated to be as follows:

C_N	±0.001
C_L	±0.001
C_A	±0.0004
C_D	±0.0004
C_m	±0.001
L/D	±0.20

The values of Reynolds number did not vary more than $\pm 0.03 \times 10^6$ from the average values of 1.43×10^6.

RESULTS AND DISCUSSION

The pertinent results from these tests are shown in figures 2 to 15. The basic data from which these results were obtained are presented for the half-cone delta wings in figure 16, for the half-cone wedge delta wings in figure 17, and for half-cone-cylinder delta wings in figure 18.

The effects of varying Reynolds number on the drag coefficient at an angle of attack of zero $C_{D,0}$ for three representative configurations are shown in figure 2. Separate points are included for both flat-top and flat-bottom configurations and the differences in $C_{D,0}$ are indicative of data accuracy. In addition to experimental data, theoretical calculations of $C_{D,0}$ are also included. These calculations contain laminar skin-friction estimates obtained by the methods of references 13 and 14, and in which, on the basis of results in reference 15, cone displacement effects have been neglected. At the test Reynolds number of 1.43×10^6, the calculations indicate that the viscous drag at zero angle of attack ranged from 2 to 5 times the inviscid drag; and the good agreement between theory and experiment implies that the boundary layer was predominantly laminar over the length of the models.

Half-Cone Delta-Wing Combinations

The effects of increasing the half-cone angle at constant wing-leading-edge sweep on the characteristics at maximum lift-drag ratios are shown in figure 3. In general, increasing cone angle results in decreases in the maximum lift-drag ratio (fig. 3(a)) and increases in the lift coefficient (fig. 3(b)) at $(L/D)_{max}$ for both model orientations. The most significant exception to this trend occurs for the very slender round-bottom half-cones alone which deviate very markedly from their flat-bottom counterparts. This behavior is attributed to a significant reduction in lifting efficiency on the round bottom as the cones become very slender. Increasing the cone angle invariably results in a decrease in the angle of attack for $(L/D)_{max}$ for the flat-top case (fig. 3(c)) whereas increases occur when the configurations are inverted.

At extreme sweep angles, increasing the wing leading-edge sweep at constant cone angle causes significant reductions in $(L/D)_{max}$ (fig. 4(a)) as the half-cone alone is approached; and in this region the flat-bottom configurations generally show superior performance. At lower sweep angles, when the cone flow field covers a relatively small part of the wing, the $(L/D)_{max}$ values appear to be only slightly affected by changes in leading-edge sweep ($\Lambda = 65^\circ$ to 70°; $\theta = 5^\circ$, 7.5°; fig. 4(a)); and the best $(L/D)_{max}$ values are again, in general, given by the flat-bottom orientation. At the intermediate sweep angles ($\Lambda = 70^\circ$ to 81°), various results are seen to occur wherein depending on cone angle and orientation, $(L/D)_{max}$ increases ($\theta = 4^\circ$, 5°; FT), decreases ($\theta = 7.5^\circ$, 9°), or remains essentially constant ($\theta = 4^\circ$, 5°; FB) with increasing wing-leading-edge sweep. Favorable interference benefits are also occurring in this sweep-angle range as shown by the superiority of the flat-top arrangements at $\theta = 4^\circ$ and 5°. The leading-edge sweep angle then, as foreseen by Eggers and Syvertson in reference 1, is one important factor which dictates the availability of favorable interference effects.

With constant cone angle, the lift coefficient at $(L/D)_{max}$ (fig. 4(b)) is, in general, reduced with increasing leading-edge sweep; and the angle of attack for $(L/D)_{max}$ (fig. 4(c)) is increased for flat-bottom configurations but generally reduced for flat-top configurations. Exceptions to these trends occur for the larger cone-alone flat-bottom configurations and the smaller cone-alone flat-top configurations.

When the performances of these configurations are compared, the volume parameter $V^{2/3}/S_p$ is used as a basis. The results are shown in figure 5. The faired lines connect points for constant leading-edge sweep. Along these lines as $V^{2/3}/S_p$ increases, the cone angles also increase. For clarity, sweep angles above 81° have been omitted from this figure.

At the top of the figure the data show the usual behavior wherein $(L/D)_{max}$ decreases with increasing $V^{2/3}/S_p$. However, a large effect of leading-edge sweep angle is evident; this effect invalidates the single-function $\left((L/D)_{max} \text{ as a function of } V^{2/3}/S_p\right)$ correlations shown in previous investigations (refs. 16 and 17). At a given value of $V^{2/3}/S_p$, increasing the leading-edge sweep angle provides a significant increase in $(L/D)_{max}$; but, as shown in the lower portion of the figure, this increase is accompanied by a sizable decrease in lift coefficient at $(L/D)_{max}$. Favorable interference benefits $\left(\text{flat-top } (L/D)_{max} \text{ superiority}\right)$ which occur only at the higher sweep angles (as was shown previously in fig. 4(a)) are further restricted to certain values of $V^{2/3}/S_p$. This volume parameter, then, is another important factor which controls the availability of favorable interference benefits.

In an effort to predict these trends in $(L/D)_{max}$, the theoretical calculations described in appendix A were made for a large number of these models. Representative results of these calculations for cone half-angles of 5° and 7.5° and various leading-edge sweep angles are shown in figure 6. The tick marks on figures 6(b) and 6(c) indicate the angles of attack for $(L/D)_{max}$. The $(L/D)_{max}$ results (fig. 6(a)) indicate remarkable agreement between the calculated and experimental results for the flat-top configurations. (A simple linear method for flat-top configuration gives comparable agreement with experimental results and is described in appendix B.) Regions of interference benefits, however, are not predicted because of the significant overestimation of the flat-bottom experimental results at the higher sweep angles. These overestimations for the flat-bottom configurations apparently result from overpredictions of the normal-force coefficients (figs. 6(b) and 6(c); $\Lambda = 75^\circ$ and 81°) for both values of θ and also underpredictions of the axial-force coefficients for $\theta = 7.5^\circ$ (fig. 6(c); $\Lambda = 70^\circ$, 75°, and 81°). Since the calculated axial-force variations with angle of attack for the flat-bottom configurations are due primarily to the change in cone pressures with angle of attack, these underpredictions of C_A are caused by underestimations of the lee-side cone pressures. These low predicted lee-side cone pressures, of course, can also contribute to overpredictions of the normal forces. However, the relatively good C_A predictions for $\theta = 5^\circ$ (fig. 6(b)) up to $\alpha_{(L/D)_{max}}$ indicate that for small cone angles the lee-side cone effects are relatively small and therefore, are not the principal cause of the overpredicted C_N values for the $\theta = 5^\circ$ flat-bottom configurations at the higher sweep angles (fig. 6(b); $\Lambda = 75^\circ$ and 81°).

In figure 7 data for the $\theta = 5^\circ$ configurations are presented in which for comparative purposes, the normal-force coefficient at an angle of attack of 0° has been deleted. The data for both flat-top and flat-bottom configurations show a decrease in normal forces as the sweep angle increases and the points at which these decreases start to occur are near the angles of attack for leading-edge shock detachment. (Leading-edge-diameter effects on shock detachment are not considered herein.) This behavior is similar to that for delta wings alone which was reported in reference 18. The theoretical predictions which were calculated from attached shock conditions show good agreement with experimental results for $\Lambda = 65^\circ$ and 70° on which the leading-edge shock is attached, but show a trend opposite to that of the data at higher sweep angles. These overpredictions of the normal-force coefficients for highly swept configurations (fig. 6(a)), are therefore attributed primarily to the effects of leading-edge shock detachment.

The effects of leading-edge shock detachment on L/D are inferred in figure 8(a) where L/D is shown as a function of C_L for both flat-top and flat-bottom configurations with $\theta = 5^\circ$ and $\Lambda = 81^\circ$ over which the leading-edge shock is detached at all values of C_L. Theoretical calculations are also presented to indicate results which would be obtained if the leading-edge shock were attached; and the angles of attack for both data and calculations are included. The results show that, for these configurations, shock-detachment

effects on $C_{L(L/D)_{max}}$ are small. With the reduced normal-force characteristics available under detached shock conditions, then, a higher angle of attack is required to attain this C_L. This condition, of course, increases the drag and lowers the $(L/D)_{max}$. Since highly swept flat-top configurations utilize favorable interference to achieve $C_{L(L/D)_{max}}$ at low angles of attack where angle-of-attack effects on drag are small, shock-detachment effects on $(L/D)_{max}$ are seen to be slight. Because of unfavorable interference effects the flat-bottom configurations, on the other hand, attain $C_{L(L/D)_{max}}$ at higher angles of attack where angle-of-attack effects on drag are significant and severe penalties occur in $(L/D)_{max}$ because of shock detachment.

Figure 8(b) shows similar information for $\theta = 5^\circ$ and $\Lambda = 75^\circ$ for which the angle of attack for leading-edge shock detachment α_{SD} occurs above $\alpha_{(L/D)_{max}}$ for the flat-top configuration, but below this angle for the flat-bottom configuration. Note also that in this instance, the flat-top configuration produces the superior $(L/D)_{max}$. This result implies that leading-edge shock detachment on flat-bottom configurations may have some effect on the availability of favorable interference effects so that when $\frac{\alpha_{SD}}{\alpha_{(L/D)_{max,FB}}} > 1$, $\frac{(L/D)_{max,FT}}{(L/D)_{max,FB}} < 1$ but when $\frac{\alpha_{SD}}{\alpha_{(L/D)_{max,FB}}} < 1$, $\frac{(L/D)_{max,FT}}{(L/D)_{max,FB}} > 1$.

The behavior of these ratios obtained from available data is shown in figure 9. The data, in general, support the suspected trend and show a definite effect of leading-edge shock detachment $\frac{\alpha_{SD}}{\alpha_{(L/D)_{max,FB}}} < 1$ on the availability of favorable interference benefits $\frac{(L/D)_{max,FT}}{(L/D)_{max,FB}} > 1$. Considerable dispersion, however, exists in the data, which is believed to be due to the uncontrolled variations in Mach number, Reynolds number, and volume parameter $V^{2/3}/S_p$.

To eliminate Mach number and Reynolds number variations, the data of the present investigation are considered; and the two pertinent ratios of figure 9 are shown as a function of $V^{2/3}/S_p$ in figure 10. Points at constant values of $V^{2/3}/S_p$ from the fairings of these data are shown in figure 11 and the results indicate that favorable interference benefits are generally available only when the leading-edge shock on flat-bottom configurations is detached and at low values of the volume parameter. The dotted line, which was obtained from cross plots of the data from figure 10, represents optimum configurations wherein the wing-leading-edge and cone shock coincide at $\alpha = 0^\circ$ and indicates

that only under the lower volume parameter restrictions $\left(\frac{V^{2/3}}{S_p} < 0.2\right)$ are favorable interference benefits available even to these configurations. On the other hand, the data to the right of the dotted line indicate that favorable interference benefits are available with sweep angles lower than optimum as long as the shock-detachment and low-volume-parameter criteria are satisfied.

An example of gains in $(L/D)_{max}$ from favorable interference benefits with optimum and off-optimum leading-edge sweep angles is shown for the $\theta = 5^\circ$ half-cone in figure 12. In addition to the present data, data from reference 4 corrected for model-balance misalinements are also included. The data indicate that some improvement in $(L/D)_{max}$ from favorable interference is available at wing-leading-edge sweep angles from 72° to 82°, a maximum increment of about 10 percent occurring at the optimum sweep angle. Note that the optimum leading-edge sweep angle is lower than the inviscid cone shock angle at $\alpha = 0^\circ$. This condition may be due to the effects of angle of attack and/or cone boundary-layer displacement which tend to increase the cone shock angle. The approximate nature of the methods of analysis available to date, however, preclude an accurate determination of this sweep angle a priori. Favorable interference benefits dissipate with off-optimum sweep angles, of course, because the wing is becoming too large (lower sweep angles) or too small (higher sweep angles) to take full advantage of the interference flow field. The approach of attached shock conditions at lower sweep angles also contributes to this dissipation.

The criteria of detached shock conditions and low-volume-parameter values dictate that favorable interference benefits are limited to increasingly higher sweep angles and lower angle cones (higher fineness ratio bodies) as the Mach number increases. This trend is supported to some extent by the helium data of reference 9 on a similar set of configurations which show, for the same range of Λ and θ variables, no evidence of favorable interference effects at a Mach number of 20.

In addition to the criteria of detached leading-edge shock conditions and low-volume-parameter values, the availability of favorable interference benefits will probably be affected by such factors as variations in Reynolds number and increases in wing leading-edge diameter. Although these factors were not considered in detail in this study, their effects can be examined by considering the lift-drag polars, with $C_{D,0}$ removed, shown in figure 13. The values of $C_{D,0}$ are shown to the left of the polars. The data is for the flat-top and flat-bottom versions of the $\theta = 4^\circ$, $\Lambda = 81^\circ$ configuration which satisfies the aforementioned geometric criteria and for which the flat-top version shows the superior $(L/D)_{max}$ at the test Reynolds number of 1.43×10^6. These polars show typical behavior for highly swept flat-top and flat-bottom configurations (see basic data, fig. 16) and indicate that where favorable interference results in a superior $(L/D)_{max}$, these benefits are available only over a limited portion of the polar because of the higher drag rise due to lift of flat-top configurations at larger values of C_L. A limited amount of data

at Reynolds numbers other than 1.43×10^6 are included which suggest that under laminar boundary-layer conditions and as long as displacement effects are not large, Reynolds number variations affect the lift-drag polars primarily by an increase in $C_{D,0}$. Similarly, the major effect of increasing leading-edge diameter should be to increase $C_{D,0}$. By assuming various values of $C_{D,0}$, $(L/D)_{max}$ values can then be calculated and the effects of Reynolds number and wing leading-edge diameter on the availability of favorable interference effects can be inferred.

The ratio $\frac{(L/D)_{max,FT}}{(L/D)_{max,FB}}$ and $(L/D)_{max,FT}$ obtained by this procedure are shown as a function of $C_{D,0}$ in the insert in figure 13. These results indicate that favorable interference benefits, $\frac{(L/D)_{max,FT}}{(L/D)_{max,FB}} > 1$, decrease with increasing $C_{D,0}$ (decreasing Reynolds number or increasing leading-edge diameter); and if the viscous effects at low Reynolds numbers or large leading-edge diameters increase $C_{D,0}$ sufficiently, favorable interference benefits become unavailable even though the geometric criteria of leading-edge shock detachment (leading-edge-diameter effects being ignored) and low volume parameter are satisfied. Furthermore, since $(L/D)_{max}$ is a strong function of $C_{D,0}$ (see insert, fig. 13), there appears to be a limiting value of $(L/D)_{max}$ (about 4) below which favorable interference benefits are unavailable.

Conversely, the results also indicate the interesting possibility that favorable interference benefits may increase markedly with an increase in Reynolds number $\left(\text{decreasing } C_{D,0}\right)$ above 1.43×10^6. The reader is reminded, however, that the observed behavior of the lift-drag polars was produced under predominantly laminar boundary-layer conditions and this inference should be avoided until further work establishes the behavior of these polars under the influence of transitional and turbulent boundary layers.

Configuration Modifications

In several investigations the half-cone was offset from the wing by a wedge angle of 1°. (See refs. 1, 2, and 4.) Although the reasons for this offset are not set forth in the literature, the object apparently is to increase the wing-interference flow field and obtain additional volume. The effects of offsetting the half-cone are shown in figure 14. The data on the left indicate that $(L/D)_{max}$ for both wing positions is significantly decreased and favorable interference benefits are counteracted by cone offsets. As seen in the data to the right an increase in volume is more efficiently accomplished by increasing cone angle rather than by offsetting the cone.

The volume distribution of a half-cone is relatively poor; and since the center of volume (representative of center-of-gravity location) is at the

0.75l station and the aerodynamic center for these half-cone delta-wing configurations is generally between 0.6l and 0.667 (see basic data, fig. 16), center-of-gravity location problems for a stable aircraft may be encountered. The results of tests on constant-length configurations with constant-volume half-cone-cylinder bodies of varying cylinder length for improving the volume distribution are shown in figure 15. Increasing the cylinder length causes a significant decrease in $(L/D)_{max}$ for both wing positions, less penalty occurring at the lower sweep angles. Favorable interference benefits also deteriorate with increasing cylinder length, probably because the strength of the wing interference region is lessened by the flow expansion around the cone-cylinder juncture. The aerodynamic center for the winged configurations is relatively unaffected by increasing cylinder length; however, it approaches the center of volume only at the longer cylinder lengths.

CONCLUSIONS

An investigation of the characteristics of half-cone delta-wing configurations under predominantly laminar boundary-layer conditions at a Mach number of 6.86 and a Reynolds number based on model length of 1.4×10^6 gave the following conclusions:

1. The maximum lift-drag ratio $(L/D)_{max}$ of both flat-top and flat-bottom half-cone delta-wing configurations is increased at a given value of the volume parameter $\left(\frac{\text{Volume}}{\text{Planform area}}\right)^{2/3}$ by increasing the wing-leading-edge sweep angle as long as the wing semiapex angle does not closely approach the cone half-angle.

2. Because favorable interference effects cause the $(L/D)_{max}$ of flat-top configurations to occur at significantly lower angles of attack than those for flat-bottom configurations, a detached wing-leading-edge shock can incur significant penalties on the $(L/D)_{max}$ of flat-bottom configurations but affect, only slightly, those for flat-top configurations.

3. Favorable interference benefits (flat-top superiority in $(L/D)_{max}$) are generally available only at wing-leading-edge sweep angles for which the wing-leading-edge shock detaches at an angle of attack below that for flat-bottom $(L/D)_{max}$ but then only over a restricted range of the volume parameter (for these tests up to about 0.20 depending on wing-leading-edge sweep). However, if the drag coefficient at zero angle of attack $C_{D,0}$ is increased sufficiently by decreases in Reynolds number and/or increases in wing leading-edge diameter, favorable interference benefits may become unavailable even though these geometric criteria are satisfied.

4. Within these restrictions, favorable interference provides a maximum improvement in $(L/D)_{max}$ over the flat-bottom configuration at an optimum

sweep angle which, in general, is lower than that given by the inviscid cone shock at zero angle of attack.

5. The criteria of detached leading-edge shock conditions and low-volume-parameter values dictate that favorable interference benefits are limited to increasingly higher leading-edge sweep angles and lower angle cones (higher fineness ratio bodies) as the Mach number increases.

6. Present-day theoretical methods are adequate for predicting the level of $(L/D)_{max}$ for both flat-top and flat-bottom configurations when attached leading-edge shock conditions exist, but because of the absence of detached shock solutions, the improvements in $(L/D)_{max}$ over the flat-bottom configuration due to favorable interference, and the geometric conditions under which they occur, are not predictable.

7. Modifications to these half-cone delta-wing configurations to increase volume by offsetting the cone from the wing or to provide a more favorable volume distribution by changing the half-cone to half-cone-cylinders at constant volume and length significantly decrease the $(L/D)_{max}$ for both flat-top and flat-bottom configurations and cause rapid deterioration of favorable interference benefits.

Langley Research Center,
National Aeronautics and Space Administration,
Langley Station, Hampton, Va., April 9, 1965.

APPENDIX A

THEORETICAL CALCULATIONS OF THE AERODYNAMIC CHARACTERISTICS OF HALF-CONE ARROW- OR DELTA-WING CONFIGURATIONS

Flat-Top Configurations

Savin's approximate solution for flat-top configurations[1] (ref. 19), which is restricted to the attached leading-edge shock case, considers a single shock pattern to be formed under the configurations. The experimental data of reference 5 shown in figure 19, however, indicate that below leading-edge shock detachment, a double shock pattern is formed which coalesces to a single shock pattern at and above leading-edge shock detachment. Goebel, in reference 17, presents a solution for the double shock case; however, the results are restricted to a half-cone delta-wing configuration. A double shock solution for arrow- or delta-winged half-cone configurations is therefore presented herein.

Consider the following generalized configuration:

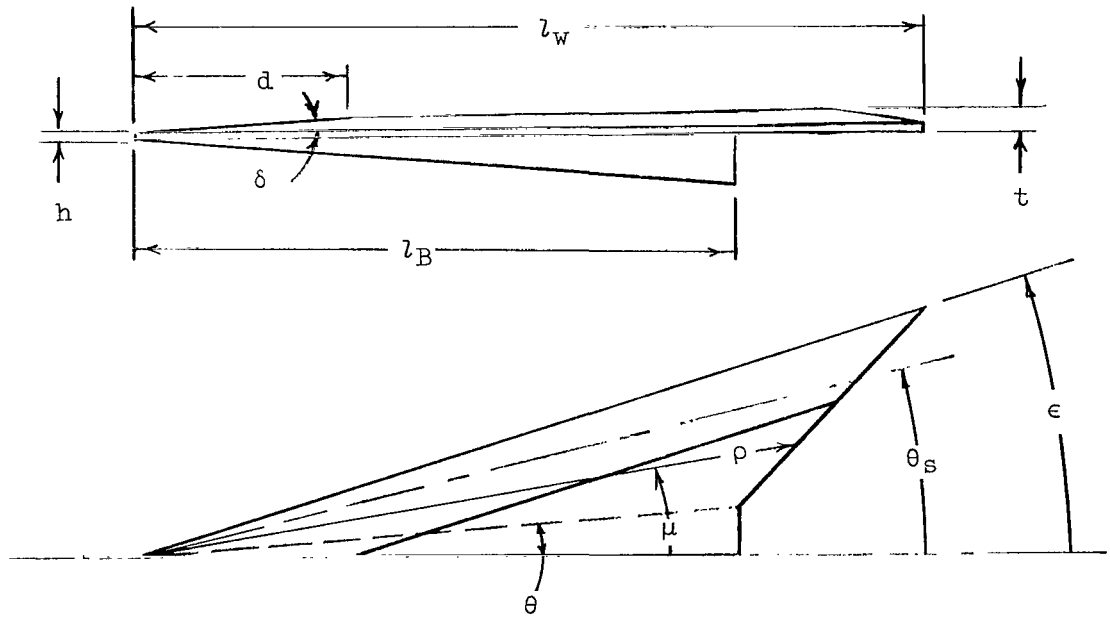

[1]During the final stages of preparing this report, the work of Mandl (ref. 20) was published in which hypersonic approximations are utilized to solve the equations of flow about these configurations. A double shock formation is considered; however, because of the time required to program the solutions on an electronic computer, comparisons of the results of the method with the included data have not been made.

where

$$\rho = \frac{l_w l_B(\tan \epsilon - \tan \theta)\sec \mu}{l_w \tan \epsilon - l_B \tan \theta - (l_w - l_B)\tan \mu}$$

and

$$S_p = l_B\left[l_w \tan \epsilon - (l_w - l_B)\tan \theta\right]$$

The wing semiapex angle ϵ instead of the sweep angle Λ is used here because of the simpler expressions provided.

On the cone the variation of surface pressure coefficient is assumed to be given by (see fig. 19)

$$C_{p,c} = C_{p,0} \cos^2\phi + C_{p,1} \sin^2\phi$$

where

$C_{p,0}$ pressure coefficient for cone lower surface

$C_{p,1}$ pressure coefficient for cone-wing juncture

Between the cone-wing juncture and cone-shock—wing juncture, the wing lower surface spanwise pressure coefficient variation is assumed to be parabolic so that

$$C_{p,w,l} = C_{p,1} - (C_{p,1} - C_{p,2})\left(\frac{\tan \mu - \tan \theta}{\tan \theta_s - \tan \theta}\right)^2$$

where $C_{p,2}$ is the pressure coefficient at cone-shock—wing juncture. Outboard of the cone-shock—wing juncture, the wing lower surface pressure coefficient is assumed to be constant at the value of $C_{p,3}$.

Integrating these pressure coefficient variations over the pertinent areas results in the following expressions for the force coefficients:

$$C_{N,c} = \frac{2C_{p,0} + C_{p,1}}{3\left[\frac{l_w}{l_B}\left(\frac{\tan \epsilon}{\tan \theta} - 1\right) + 1\right]} \qquad (A1)$$

APPENDIX A

$$C_{A,c} = \frac{\pi\left(C_{p,0} + C_{p,1}\right)\tan\theta}{4\left[\frac{l_w}{l_B}\left(\frac{\tan\epsilon}{\tan\theta} - 1\right) + 1\right]} \tag{A2}$$

$$C_{N,w,l} = \frac{(\tan\epsilon - \tan\theta)^2(\tan\theta_s - \tan\theta)}{\left(\frac{l_w}{l_B} + \frac{l_B}{l_w} - 2\right)\left[\tan\epsilon - \left(1 - \frac{l_B}{l_w}\right)\tan\theta\right]}\left\{\frac{C_{p,1}}{(G - \tan\theta_s)(G - \tan\theta)}\right.$$

$$\left. - \frac{C_{p,1} - C_{p,2}}{(\tan\theta_s - \tan\theta)^2}\left[1 + \frac{G - \tan\theta}{G - \tan\theta_s} - \frac{2(G - \tan\theta)}{\tan\theta_s - \tan\theta}\log_e\frac{G - \tan\theta}{G - \tan\theta_s}\right]\right\}$$

$$+ \frac{\left(1 - \frac{\tan\theta_s}{\tan\epsilon}\right)\left(1 - \frac{\tan\theta}{\tan\epsilon}\right)C_{p,3}}{\left[1 - \left(1 - \frac{l_B}{l_w}\right)\frac{\tan\theta_s}{\tan\epsilon} - \frac{l_B}{l_w}\frac{\tan\theta}{\tan\epsilon}\right]\left[1 - \left(1 - \frac{l_B}{l_w}\right)\frac{\tan\theta}{\tan\epsilon}\right]} \tag{A3}$$

where

$$G = \frac{\tan\epsilon}{1 - \frac{l_B}{l_w}} - \frac{\tan\theta}{\frac{l_w}{l_B} - 1}$$

For a delta-wing configuration where $l_w = l_B$, equation (A3) is indeterminant. For this case,

$$C_{N,w,l} = \frac{1}{3}\left(\frac{\tan\theta_s}{\tan\epsilon} - \frac{\tan\theta}{\tan\epsilon}\right)\left(2C_{p,1} + C_{p,2}\right) + \left(1 - \frac{\tan\theta_s}{\tan\epsilon}\right)C_{p,3} \tag{A3a}$$

For the upper wing surface if $\frac{d}{l_B} \leqq 1 - \frac{\tan\theta}{\tan\epsilon}$,

$$C_{N,w,u} = -\left\{C_{p,fp} + \left(C_{p,wedge} - C_{p,fp}\right)\left[2\,\frac{l_w}{l_B} - \frac{d}{l_B}\left(\frac{\frac{l_w}{l_B} - \frac{\tan\theta}{\tan\epsilon}}{1 - \frac{\tan\theta}{\tan\epsilon}}\right)\right]\frac{\frac{d}{l_B}}{\frac{l_w}{l_B} - \left(\frac{l_w}{l_B} - 1\right)\frac{\tan\theta}{\tan\epsilon}}\right\} \tag{A4}$$

but if $\frac{d}{l_B} \geqq 1 - \frac{\tan\theta}{\tan\epsilon}$,

$$C_{N,w,u} = -\left\{C_{p,fp} + \left(C_{p,wedge} - C_{p,fp}\right)\left[1 - \frac{\left(1 - \frac{d}{l_B}\right)^2}{\frac{l_w}{l_B} - \left(\frac{l_w}{l_B} - 1\right)\frac{\tan\theta}{\tan\epsilon}}\right]\right\} \tag{A4a}$$

where

$C_{p,wedge}$ pressure coefficient on wedge portion of wing

$C_{p,fp}$ pressure coefficient on flat-plate portion of wing

The wing axial-force coefficient, when $\frac{d}{l_B} \leqq 1 - \frac{\tan\theta}{\tan\epsilon}$ is given by

$$C_{A,w} = \frac{\frac{t - h}{l_B}\,C_{p,wedge}}{\frac{l_w}{l_B} - \left(\frac{l_w}{l_B} - 1\right)\frac{\tan\theta}{\tan\epsilon}}\left(2\,\frac{l_w}{l_B} - \frac{d}{l_B}\,\frac{\frac{l_w}{l_B} - \frac{\tan\theta}{\tan\epsilon}}{1 - \frac{\tan\theta}{\tan\epsilon}}\right) \tag{A5}$$

but if $\frac{d}{l_B} \geqq 1 - \frac{\tan\theta}{\tan\epsilon}$,

$$C_{A,w} = \frac{\frac{t - h}{l_B}\,C_{p,wedge}}{\frac{l_w}{l_B} - \left(\frac{l_w}{l_B} - 1\right)\frac{\tan\theta}{\tan\epsilon}}\left[1 - \frac{d}{l_B} + \frac{\tan\theta}{\tan\epsilon} - \frac{l_B}{d}\left(1 - \frac{\tan\theta}{\tan\epsilon}\right)\left(1 - \frac{d}{l_B} - \frac{l_w}{l_B}\right)\right] \tag{A5a}$$

APPENDIX A

For the leading edge

$$C_{A,le} = \frac{2C_{p,le}\frac{h}{l_B}}{\sin \epsilon - \left(1 - \frac{l_B}{l_w}\right)\tan \theta \cos \epsilon} \tag{A6}$$

Finally, the total-force coefficients are given by

$$C_N = C_{N,c} + C_{N,w,l} + C_{N,w,u} \tag{A7}$$

$$C_A = C_{A,c} + C_{A,w} + C_{A,le} + C_{A,friction} \tag{A8}$$

In the application of these equations to the configurations of this report, $C_{p,0}$ was calculated from tangent cone theory $C_{p,le}$ from Newtonian theory, and $C_{p,3}$, $C_{p,wedge}$, and $C_{p,fp}$ from shock-expansion theory applied in streamwise planes.

For $\gamma = 1.4$, values of $C_{p,0}$ can be obtained approximately from

$$C_{p,0}M_\infty^2 = 2.4(M_\infty \sin \theta)^{1.6309} \qquad \left(M_\infty \sin \theta \leqq 1\right) \tag{A9}$$

or

$$C_{p,0}M_\infty^2 = 2.4(M_\infty \sin \theta)^{1.9378} \qquad \left(M_\infty \sin \theta \geqq 1\right) \tag{A9a}$$

or more exactly from reference 21.

For other values of γ, from reference 22,

$$C_{p,0} = \sin \theta \left\{ \left[\frac{\gamma + 7}{4} + \left(\frac{\gamma - 1}{4}\right)^2 + \frac{6}{M_\infty^6} \right] \sin \theta + \frac{1}{M_\infty^2} - \frac{1}{M_\infty^4} \right\} \tag{A9b}$$

At the cone-wing juncture and the cone-shock—wing juncture, it was assumed that

$$C_{p,1} = C_{p,0}$$

and

$$C_{p,2} = \frac{C_{p,0} + C_{p,3}}{2} \tag{A10}$$

which give good approximations to the pressure data in reference 5 at angles of attack up to about 6°. Between $0 \leqq \frac{\alpha}{\alpha_{SD}} \leqq 1$, the cone-shock—wing juncture is obtained from

$$\frac{\tan \theta_s}{\tan \epsilon} = \frac{y_s}{y_{le}} = \left[1 - \left(\frac{\tan \theta_s}{\tan \epsilon}\right)_{\alpha=0}\right]\left(\frac{\alpha}{\alpha_{SD}}\right)^2 + \left(\frac{\tan \theta_s}{\tan \epsilon}\right)_{\alpha=0} \tag{A11}$$

which approximates reasonably well the data in figure 19, and where $(\theta_s)_{\alpha=0}$ is obtained from zero yaw cone solutions (ref. 21) or from

$$\sin^2(\theta_s)_{\alpha=0} = \frac{1}{M_\infty{}^2} + \frac{\gamma + 1}{2} \sin^2\theta \tag{A12}$$

from reference 22.

For cases where the leading-edge shock was detached, no solutions are available; therefore, $C_{p,3}$ in equation (A10) was still assumed to be given by attached two-dimensional oblique-shock solutions.

The final drag and axial-force values presented in figure 6 for the various configurations contain viscous drag increments $C_{A,friction}$ which were taken to be the difference between the calculated and experimental C_A values at an angle of attack of zero. For a given configuration this increment was assumed to be constant over the angle-of-attack range. Calculations indicate that this assumption is reasonable as long as the angle of attack is limited to 10° or less.

Flat-Bottom Configurations

Because of the complex lee-side flow field, no solutions for the flow about these configurations have as yet been proposed. For an approximate analysis, however, equations (A1) to (A8) were used by substituting negative angles of attack. To determine the pressure coefficients, the approach suggested in reference 4 was utilized in which the cone is considered to be operating at zero angle of attack in the lee-side flow field produced by the wing. With this assumption,

APPENDIX A

$$C_{p,0} = C_{p,1} = \left(\frac{p_0}{p_\infty} - 1\right)\frac{2}{\gamma M_\infty^2} \qquad \left(\frac{p_0}{p_\infty} = f_1\left(M_w', \theta\right)\right)$$

$$C_{p,3} = \left(\frac{p_3}{p_\infty} - 1\right)\frac{2}{\gamma M_\infty^2} \qquad \left(\frac{p_3}{p_\infty} = f_2\left(M_w', \theta\right)\right)$$

$$\theta_s = f_3\left(M_w', \theta\right)$$

where

$$M_w' = f(\alpha)$$

and M_w' can be found from flow-expansion solutions (ref. 23) and p_0/p_∞, p_3/p_∞, and θ_s from zero-yaw cone solutions (ref. 21).

APPENDIX B

LINEAR SOLUTION FOR FLAT-TOP CONFIGURATION

Since the angle of attack at which $(L/D)_{max}$ occurs for flat-top configurations is relatively low, it might be reasoned that the effects on $(L/D)_{max}$ of nonlinearities in the variations of C_N and C_A with angle of attack are secondary. If this is true, a simple linear solution for flat-top configurations should give acceptable predictions of $(L/D)_{max}$. Eggers and Syvertson, in reference 1, introduced the flat-top favorable-interference concept by means of a linear solution; however, their result, in general, yields excessive values of $(L/D)_{max}$. This condition occurs, it is believed, because inherent in their order of magnitude analysis is the assumption that the axial-force coefficient is invariant with angle of attack, but the C_A data in figure 6 indicate this assumption to be unrealistic.

To obtain a solution which contains this C_A variation, assume the following expressions to be valid over a small angle-of-attack range

$$C_N = C_{N,0} + k_N\alpha \tag{B1}$$

$$C_A = C_{A,0} + k_A\alpha \tag{B2}$$

where $C_{N,0}$ and $C_{A,0}$ are the normal and axial coefficients at zero angle of attack, respectively, k_N and k_A the respective normal and axial curve slopes at zero angle of attack, and α is measured in radians. The lift-drag ratio for slender configurations can be closely approximated by

$$\frac{L}{D} = \frac{C_N}{C_A + C_N\alpha} \tag{B3}$$

If this expression is maximized with respect to α and equations (B1) and (B2) substituted into the result, there is obtained

$$\alpha_{(L/D)_{max}} = \frac{1}{k_N}\left(\pm\sqrt{k_N C_{A,0} - k_A C_{N,0}} - C_{N,0}\right) \tag{B4}$$

where the positive sign preceding the radical refers to flat-top configurations at positive angles of attack and the negative sign for flat-bottom configurations at negative angles of attack. Since the $\alpha_{(L/D)_{max}}$ for flat-bottom

configurations, in general, occurs at angles of attack sufficiently high to make the force-coefficient nonlinearity effects significant, the negative sign is rejected and the analysis is restricted to flat-top configurations.

(Both flat-top and flat-bottom configurations could be treated by a similar analysis wherein the nonlinear terms were included by expressing C_N and C_A as polynomials in powers of α. This analysis is the general case of the one treated here. If powers of α greater than 1 are considered, however, the resulting expressions for $\alpha_{(L/D)_{max}}$ require reiterative solutions and are too complex to be useful in the simple analysis desired here.)

Substituting equations (B1), (B2), and (B4) into equation (B3) then gives

$$(L/D)_{max} = \frac{k_N}{2\sqrt{k_N C_{A,0} - k_A C_{N,0}} + k_A - C_{N,0}} \tag{B5}$$

for which if $k_A = 0$

$$(L/D)_{max} = \frac{k_N}{2\sqrt{k_N C_{A,0}} - C_{N,0}}$$

which agrees with the result of reference 1. Since in many cases

$$k_A C_{N,0} \ll k_N C_{A,0}$$

equation (B5) indicates the inclusion of the axial term can significantly lower the flat-top $(L/D)_{max}$.

To apply equation (B5) the various terms can be calculated at an angle of attack of zero through the use of the equations in appendix A and their derivations with respect to α. Since the derivatives involve only the pressure coefficient terms, the following equations are useful:

For tangent cone theory and using equation (A9)

$$\left.\frac{dC_{p,0}}{d\alpha}\right]_{\alpha=0} = \frac{dC_{p,0}}{d\theta} = \frac{3.91(\sin\theta)^{0.6309}}{(M_\infty)^{0.3691}} \qquad \left(M_\infty \sin\theta \leqq 1\right)$$

or

$$\left.\frac{dC_{p,0}}{d\alpha}\right]_{\alpha=0} = \frac{4.646(\sin\theta)^{0.9378}}{(M_\infty)^{0.0622}} \qquad \left(M_\infty \sin\theta \geq 1\right)$$

For flat-wing surfaces, of course

$$\left.\frac{dC_{p,fp}}{d\alpha}\right]_{\alpha=0} = -\left.\frac{dC_{p,3}}{d\alpha}\right]_{\alpha=0} = -\frac{2}{\beta} \qquad \left(\beta = \sqrt{M_\infty{}^2 - 1}\right)$$

and for wing upper surface wedge pressures from reference 24

$$\left.\frac{dC_{p,wedge}}{d\alpha}\right]_{\alpha=0} = \frac{dC_{p,wedge}}{d\delta}$$

$$= -\cos\delta\left[\frac{2}{\beta} + (\gamma+1)\left(\frac{M_\infty}{\beta}\right)^2 \sin\delta + \left(\frac{\gamma+1}{4}M_\infty{}^2\right)^2 \frac{3\sin^2\delta}{\beta^3} + \cdots\right]$$

Calculations based on equation (B5) are compared with experimental data for the flat-top delta-wing configurations of this paper ($M_\infty = 6.86$) and the arrow-winged configurations from reference 3 ($\theta = 5.71^\circ$) in the following tables:

Half-cone delta wings

Λ, deg	$(L/D)_{max}$	
	Experimental	Calculated
$\theta = 5^\circ$		
65	5.2	5.2
70	5.3	5.5
75	5.5	5.4
81	5.0	5.4
$\theta = 7.5^\circ$		
65	4.7	4.7
70	4.7	4.5
75	4.5	4.5
81	4.0	4.0
$\theta = 9.0^\circ$		
65	4.1	4.0
70	3.8	3.9
75	3.9	3.8

Half-cone arrow wings

M	$(L/D)_{max}$	
	Experimental	Calculated
$\Lambda = 75^\circ$		
3	7.2	7.7
4.24	6.9	6.5
5.05	6.3	5.9
6.28	4.6	4.6
$\Lambda = 77.5^\circ$		
3	6.7	6.8
5.24	6.5	6.4
5.05	6.1	6.1
6.28	4.5	4.6

In general, the method appears to yield reasonable results.

REFERENCES

1. Eggers, A. J., Jr.; and Syvertson, Clarence A.: Aircraft Configurations Developing High Lift-Drag Ratios at High Supersonic Speeds. NACA RM A55L05, 1956.

2. Syvertson, Clarence A.; Gloria, Hermilo R.; and Sarabia, Michael F.: Aerodynamic Performance and Static Stability and Control of Flat-Top Hypersonic Gliders at Mach Numbers From 0.6 to 18. NACA RM A58G17, 1958.

3. Syvertson, Clarence A.; Wong, Thomas J.; and Gloria, Hermilo R.: Additional Experiments With Flat-Top Wing-Body Combinations at High Supersonic Speeds. NACA RM A56I11, 1957.

4. Armstrong, William O.; and Ladson, Charles L. (With Appendix by Donald L. Baradell and Thomas A. Blackstock): Effects of Variation in Body Orientation and Wing and Body Geometry on Lift-Drag Characteristics of a Series of Wing-Body Combinations at Mach Numbers From 3 to 18. NASA TM X-73, 1959.

5. Mead, Harold R.; Koch, Frank; and Hartofilis, Stavros A.: Theoretical Prediction of Pressures in Hypersonic Flow With Special Reference to Configurations Having Attached Leading-Edge Shock. ASD TR 61-60, U.S. Air Force.
   Part II. Experimental Pressure Measurements at Mach 5 and 8, May 1962.
   Part III. Experimental Measurements of Forces at Mach 8 and Pressures at Mach 21, Oct. 1962. (Available from ASTIA as 291219.)

6. Geiger, Richard E.: Experimental Lift and Drag of a Series of Glide Configurations at Mach Numbers 12.6 and 17.5. J. Aerospace Sci., vol. 29, no. 4, Apr. 1962, pp. 410-419.

7. Fetterman, David E.; Henderson, Arthur, Jr., Bertram, Mitchel H.; and Johnston, Patrick J.: Studies Relating to the Attainment of High Lift-Drag Ratios at Hypersonic Speeds. NASA TN D-2956, 1965.

8. Becker, John V.: Studies of High Lift/Drag Ratio Hypersonic Configurations. International Council of the Aeronautical Sciences, Fourth Congress, Paris - 1964, Spartan and MacMillan & Co., Ltd., 1965.

9. Johnston, Patrick J.; Snyder, Curtis D.; and Witcofski, Robert D.: Maximum Lift-Drag Ratios of Delta-Wing—Half-Cone Combinations at a Mach Number of 20 in Helium. NASA TN D-2762, 1965.

10. Bertram, Mitchel H.: Exploratory Investigation of Boundary-Layer Transition on a Hollow Cylinder at a Mach Number of 6.9. NACA Rept. 1313, 1957. (Supersedes NACA TN 3546.)

11. McLellan, Charles H.; Williams, Thomas W.; and Bertram, Mitchel H.: Investigation of a Two-Step Nozzle in the Langley 11-Inch Hypersonic Tunnel. NACA TN 2171, 1950.

12. McLellan, Charles H.; Williams, Thomas W.; and Beckwith, Ivan E.: Investigation of the Flow Through a Single-Stage Two-dimensional Nozzle in the Langley 11-Inch Hypersonic Tunnel. NACA TN 2223, 1950.

13. Monaghan, R. J.: An Approximate Solution of the Compressible Laminar Boundary Layer on a Flat Plate. R. & M. No. 2760, British A.R.C., 1953.

14. Bertram, Mitchel H.: Boundary-Layer Displacement Effects in Air at Mach Numbers of 6.8 and 9.6. NASA TR R-22, 1959. (Supersedes NACA TN 4133.)

15. Probstein, Ronald F.: Interacting Hypersonic Laminar Boundary-Layer Flow Over a Cone. Tech. Rept. AF 2798/1 (Contract AF 33(161)-2798), Div. Eng., Brown Univ., Mar. 1955.

16. McLellan, Charles H.; and Ladson, Charles L.: A Summary of the Aerodynamic Performance of Hypersonic Gliders. NASA TM X-237, 1960.

17. Goebel, T. P.; Martin, J. J.; and Boyd, J. A.: Factors Affecting Lift-Drag Ratios at Mach Numbers From 5 to 20. AIAA J., vol. 1, no. 3, Mar. 1963, pp. 640-650.

18. Bertram, Mitchel H.; and McCauley, William D.: Investigation of the Aerodynamic Characteristics at High Supersonic Mach Numbers of a Family of Delta Wings Having Double-Wedge Sections With the Maximum Thickness at 0.18 Chord. NACA RM L54G28, 1954.

19. Savin, Raymond C.: Approximate Solutions for the Flow About Flat-Top Wing-Body Configurations at High Supersonic Airspeeds. NACA RM A58F02, 1958.

20. Mandl, Paul: A Theoretical Study of the Inviscid Hypersonic Flow About a Conical Flat-Top Wing-Body Combination. AIAA J., vol. 2, no. 11, Nov. 1964, pp. 1956-1964.

21. Bertram, Mitchel H.: Correlation Graphs For Supersonic Flow Around Right Circular Cones at Zero Yaw in Air as a Perfect Gas. NASA TN D-2339, 1964.

22. Simon, Wayne E.; and Walter, Louise A.: Approximations for Supersonic Flow Over Cones. AIAA J. (Tech. Notes), vol. 1, no. 7, July 1963, pp. 1696-1698.

23. Ames Research Staff: Equations, Tables, and Charts For Compressible Flow. NACA Rept. 1135, 1953. (Supersedes NACA TN 1428.)

24. Bertram, Mitchel H.; and Cook, Barbara S.: The Correlation of Oblique Shock Parameters For Ratios of Specific Heats From 1 to 5/3 With Application to Real Gas Flows. NASA TR R-171, 1963.

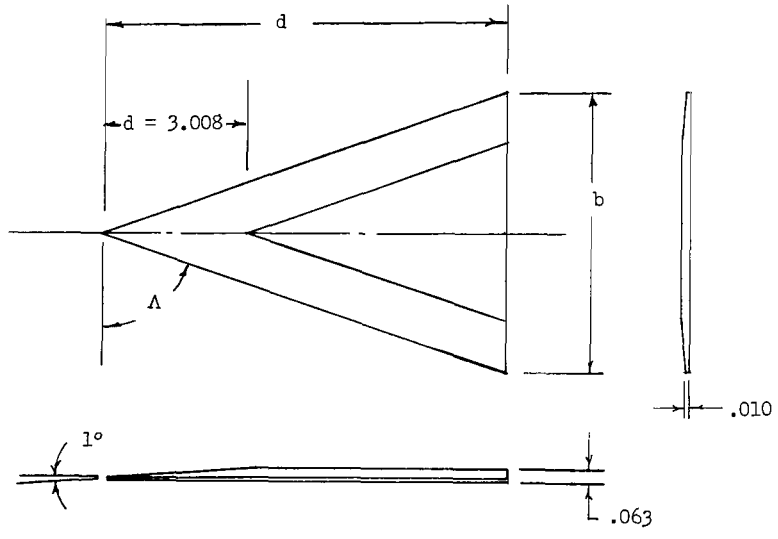

Delta wings

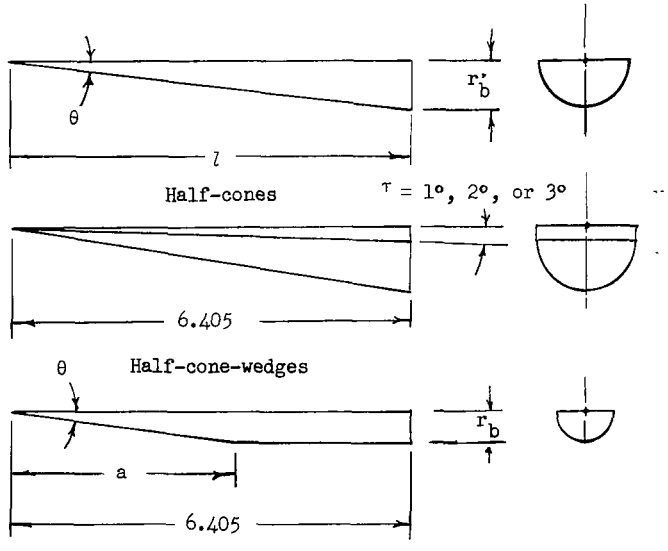

Half-cones

Half-cone-wedges

Half-cone-cylinders

Delta wings

Λ, deg	l	b	$\bar{c}$	S_p, in.^{2}	V, in.^{3}
85	8.340	1.459	5.560	6.120	0.281
85	6.404	1.120	4.270	3.590	0.151
83	8.340	2.048	5.560	8.540	0.395
83	6.404	1.573	4.270	5.040	0.212
81	8.340	2.638	5.560	11.000	0.509
81	6.404	2.028	4.270	6.500	0.273
81	4.855	1.538	3.235	3.730	0.100
75	6.404	3.432	4.270	11.000	0.462
75	4.855	2.600	3.235	6.310	0.169
70	4.855	3.534	3.235	8.580	0.229
65	4.855	4.528	3.235	10.980	0.294

Half-cones

θ, deg	l	r_b	$\bar{c}$	S_p, in.^{2}	V, in.^{3}
3.0	8.340	0.437	5.560	3.645	0.835
4.0	6.404	0.447	4.270	2.860	0.664
5.0	6.404	0.558	4.270	3.575	1.053
5.0	4.855	0.423	3.235	2.053	0.455
7.5	4.855	0.639	3.235	3.100	1.033
9.0	4.855	0.769	3.235	3.730	1.496

Half-cone-cylinders

θ, deg	α	r_b	$\bar{c}$	S_p, in.^{2}	V, in.^{3}
6.05	4.075	0.432	4.73	3.770	1.078
7.06	3.202	0.396	4.98	3.800	1.050
8.49	2.540	0.379	5.19	3.890	1.065
8.85	2.378	0.370	5.32	3.860	1.040

Figure 1.- Drawings and geometric properties of models. Dimensions are in inches unless otherwise noted.

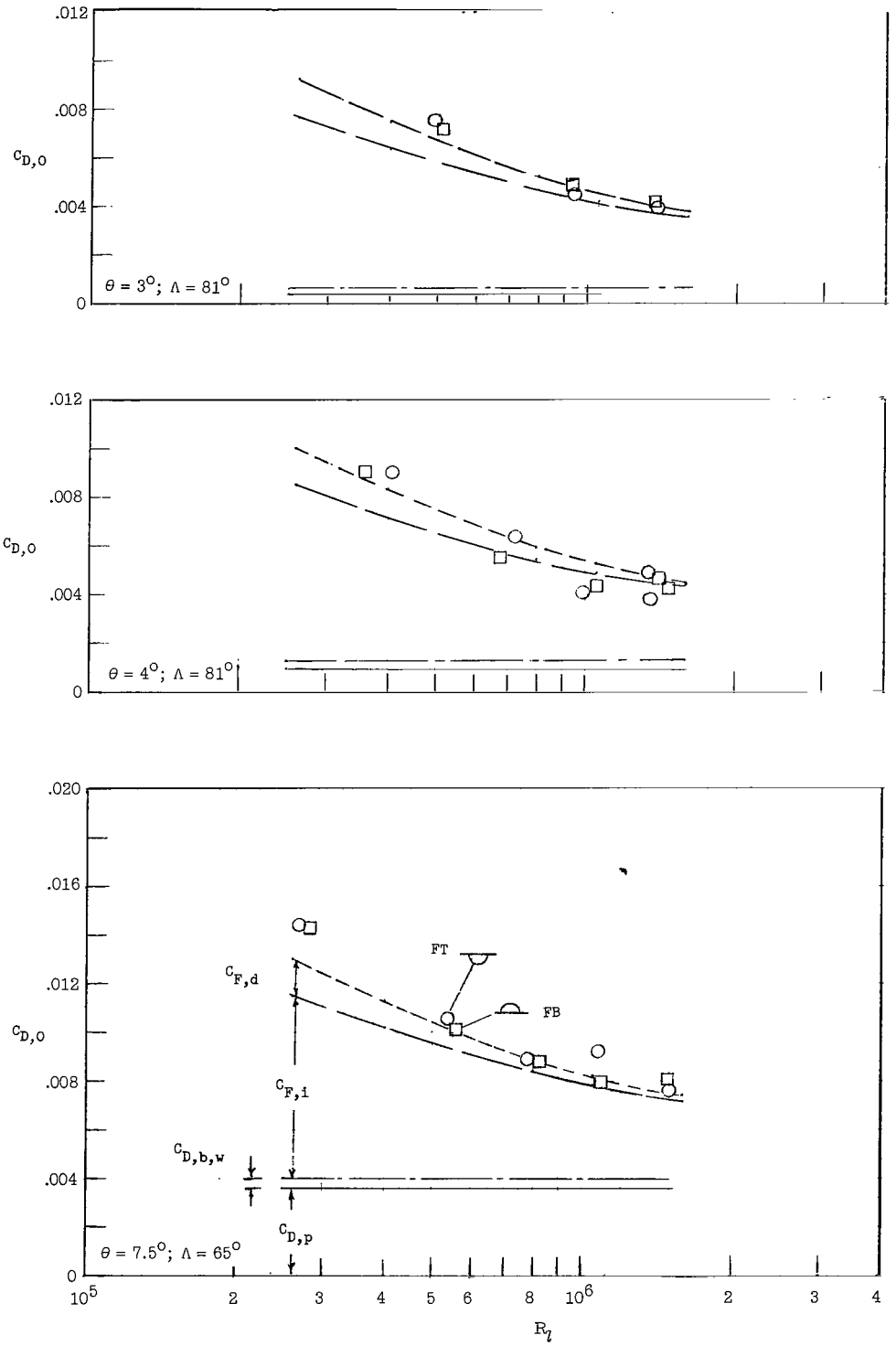

Figure 2.- Variation of zero angle-of-attack drag coefficient with Reynolds number for several half-cone delta-wing configurations.

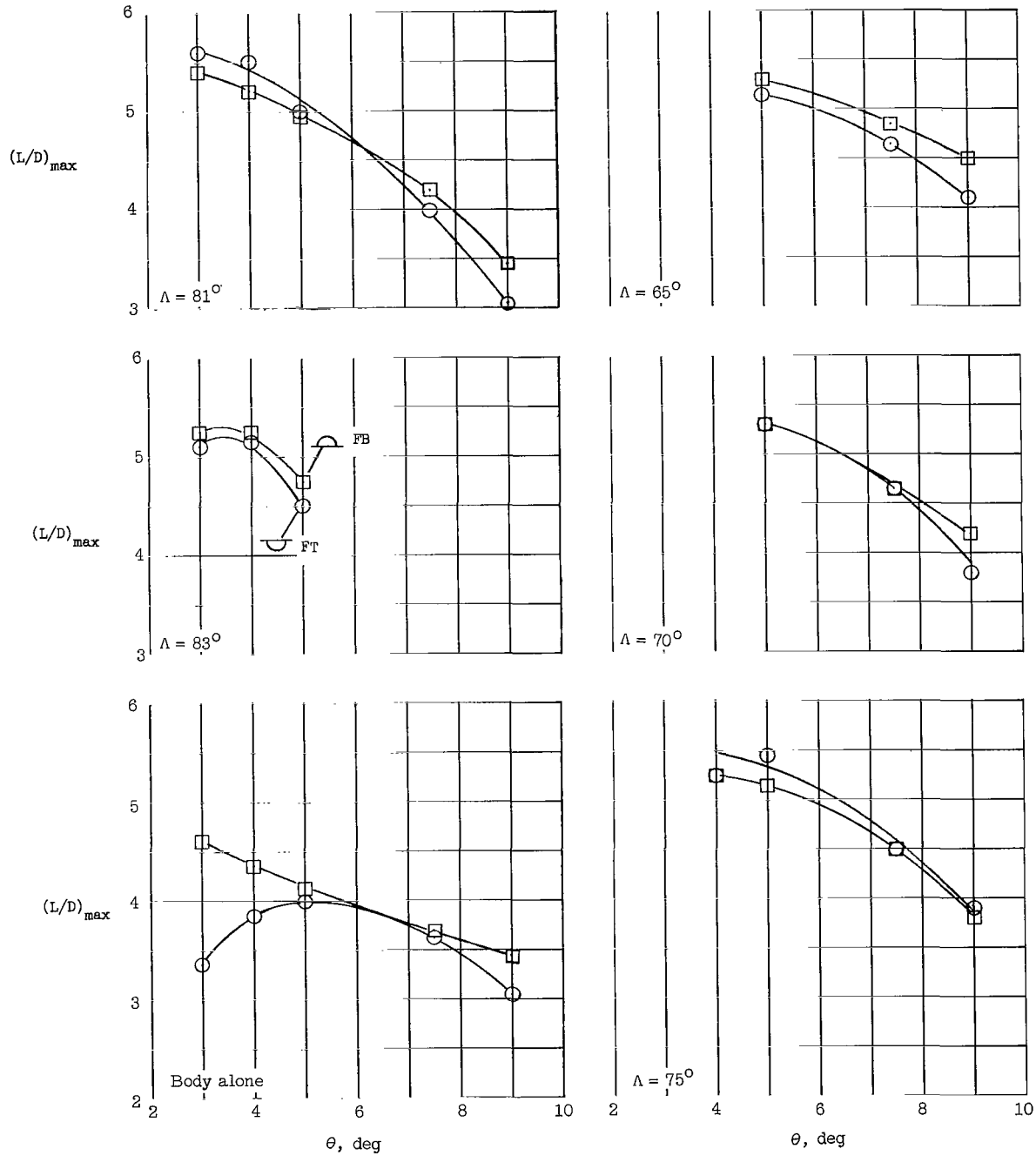

(a) $(L/D)_{max}$.

Figure 3.- Effect of cone angle on the maximum lift-drag-ratio characteristics of half-cone delta-wing configurations.

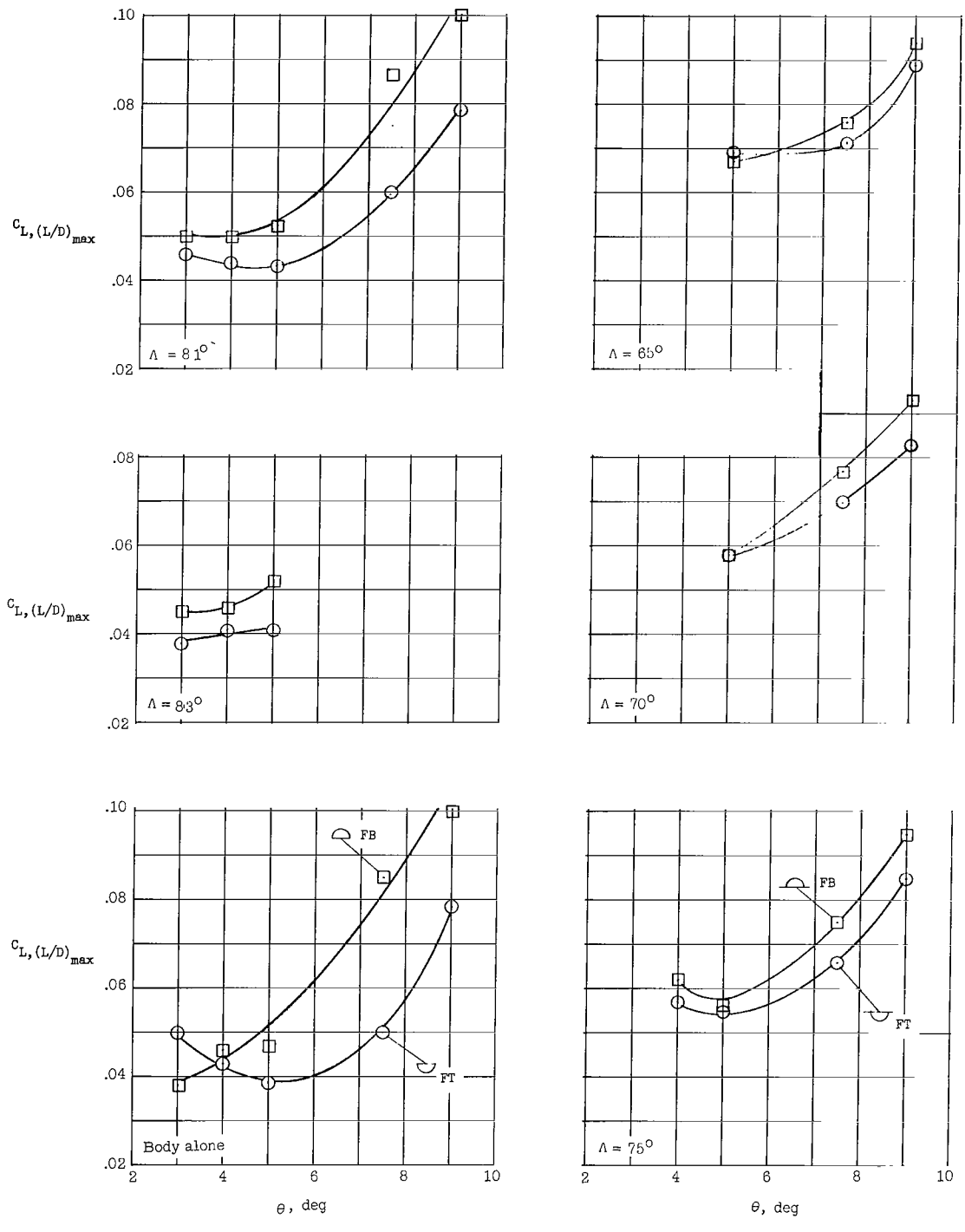

(b) $C_{L(L/D)_{max}}$.

Figure 3.- Continued.

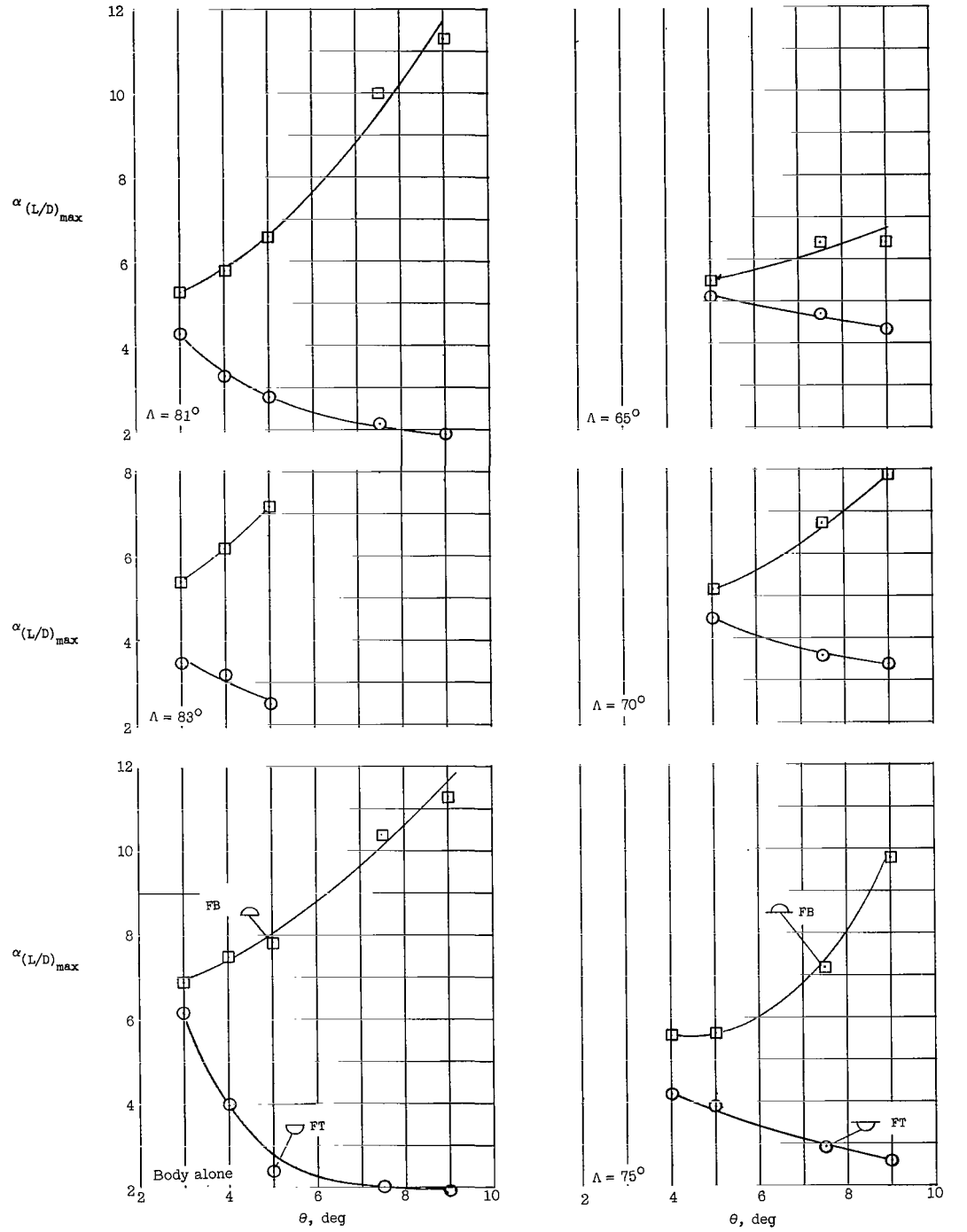

(c) $\alpha_{(L/D)_{max}}$.

Figure 3.- Concluded.

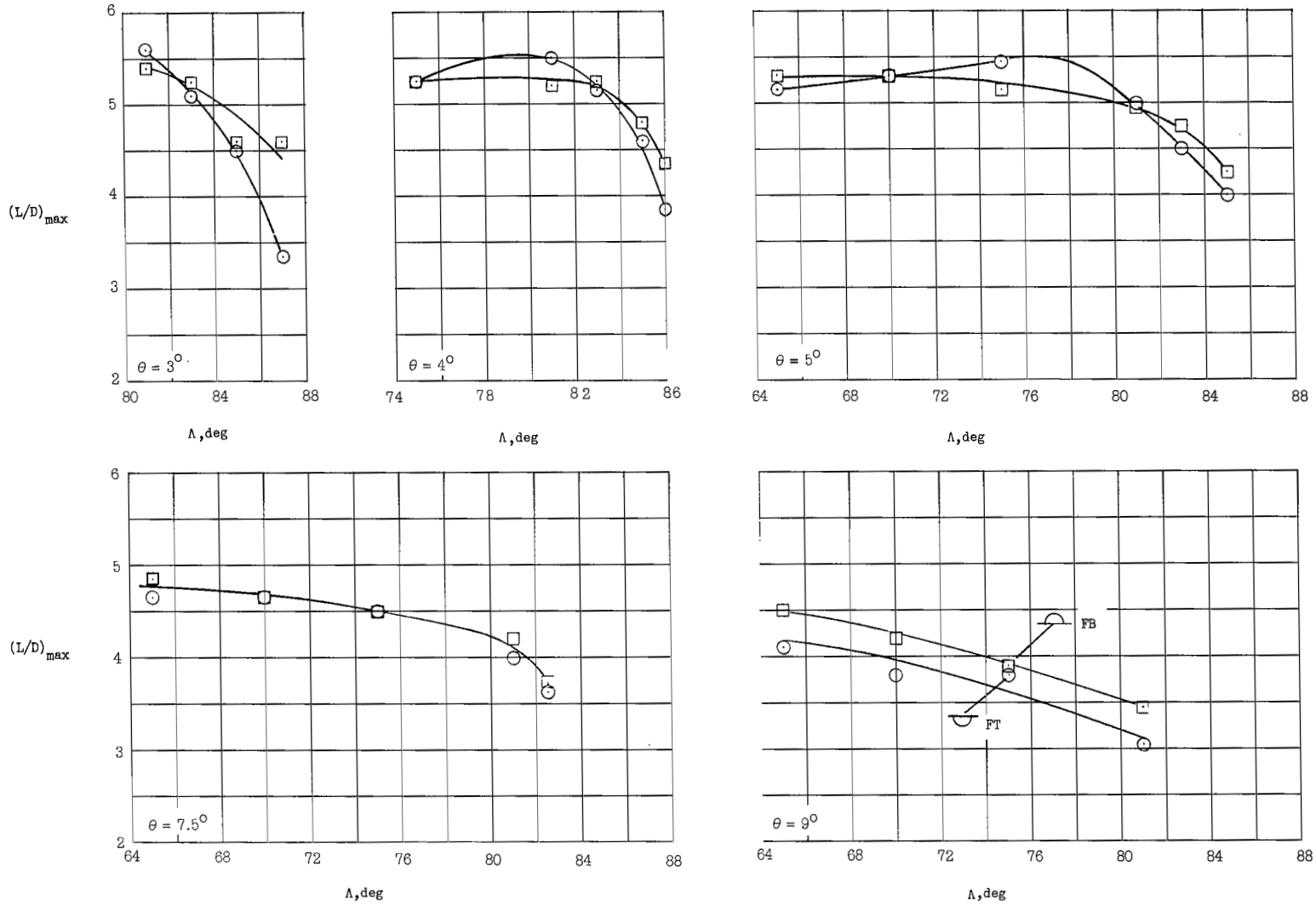

(a) $(L/D)_{max}$.

Figure 4.- Effect of leading-edge sweep angle on maximum lift-drag-ratio characteristics of half-cone delta-wing configurations.

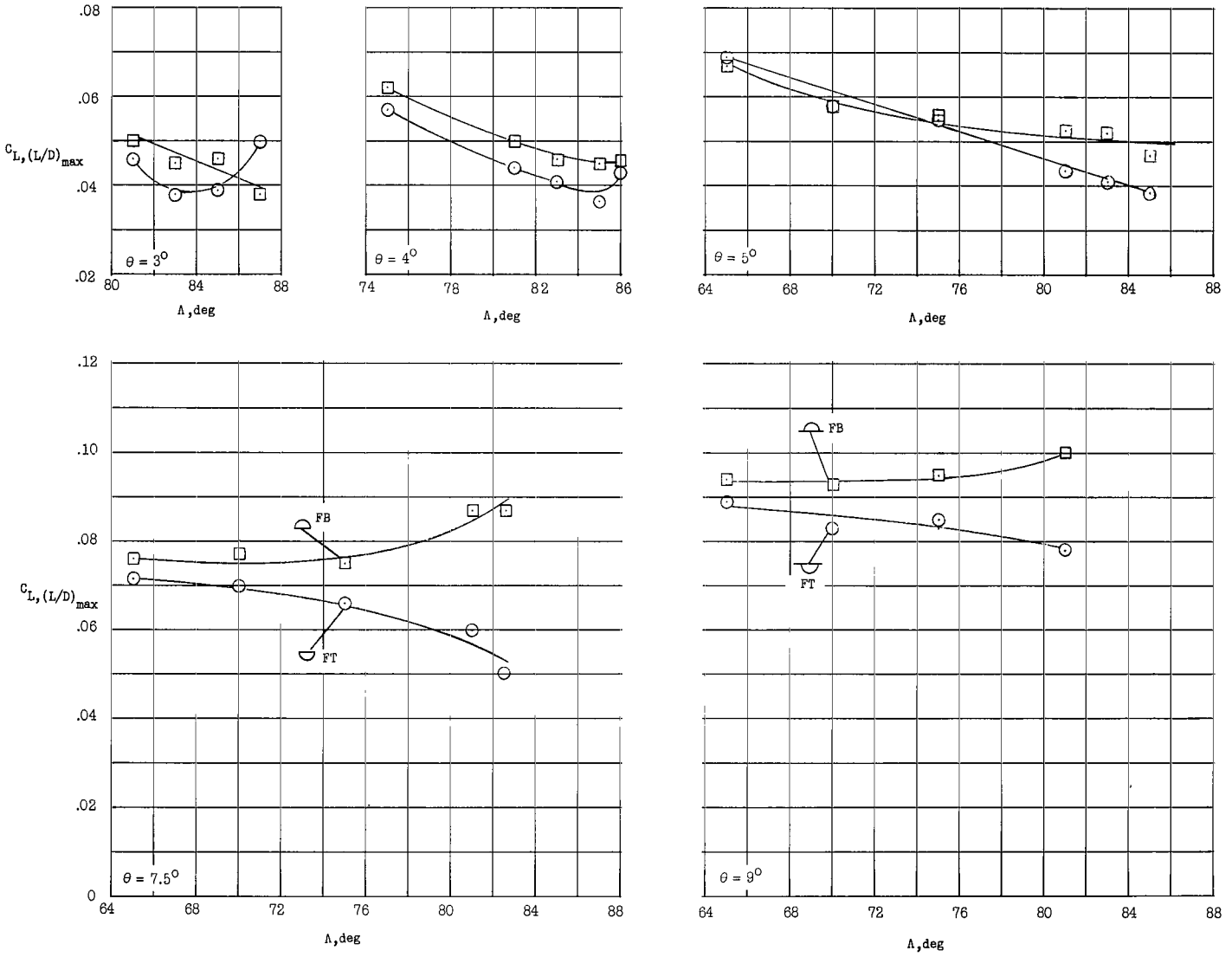

(b) $C_{L(L/D)_{max}}$.

Figure 4.- Continued.

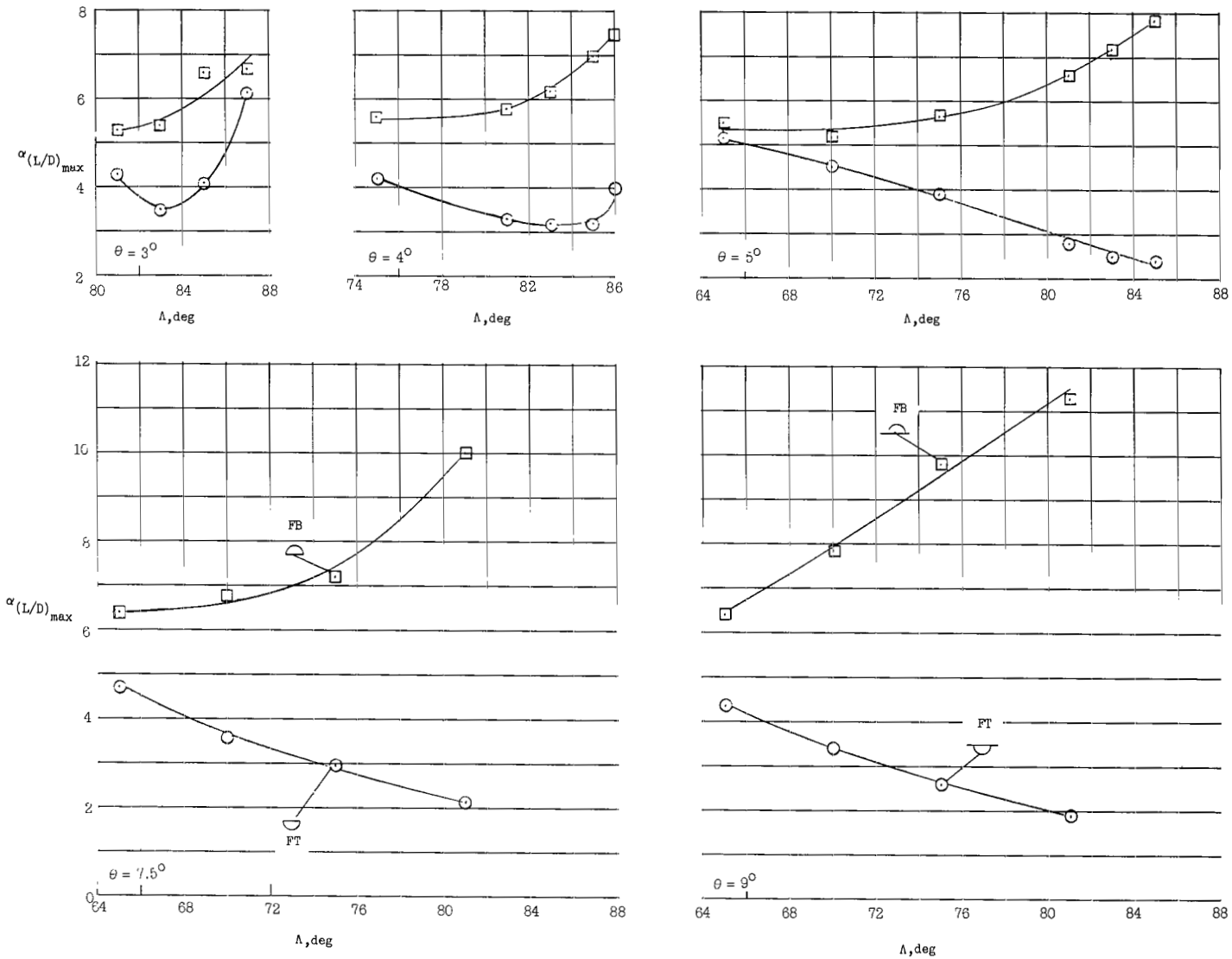

(c) $\alpha_{(L/D)_{max}}$.

Figure 4.- Concluded.

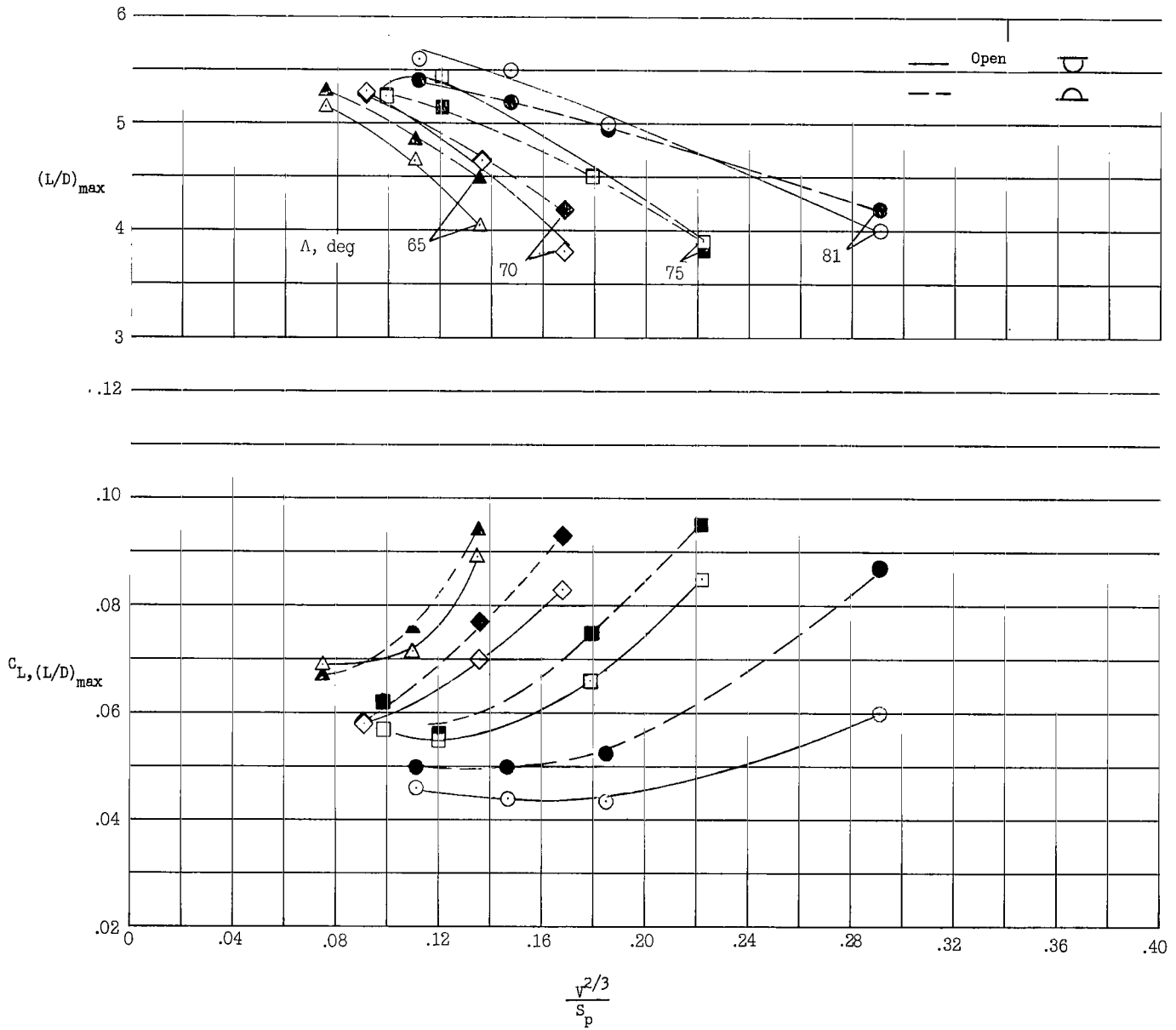

Figure 5.- Performance of half-cone delta-wing configurations.

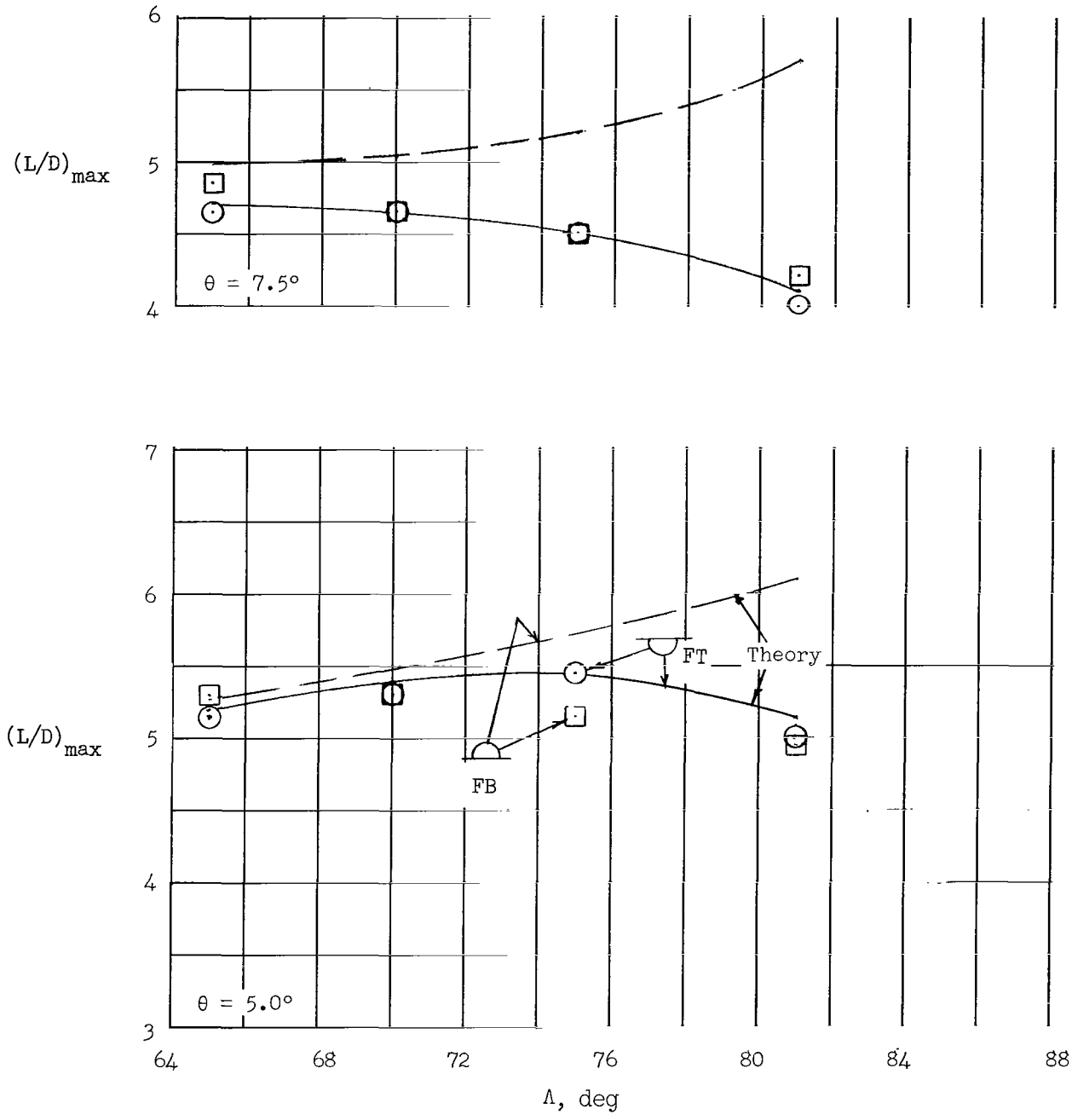

(a) Variation of $(L/D)_{max}$ with Λ.

Figure 6.- Comparison of experimental and theoretical characteristics of half-cone delta-wing configurations.

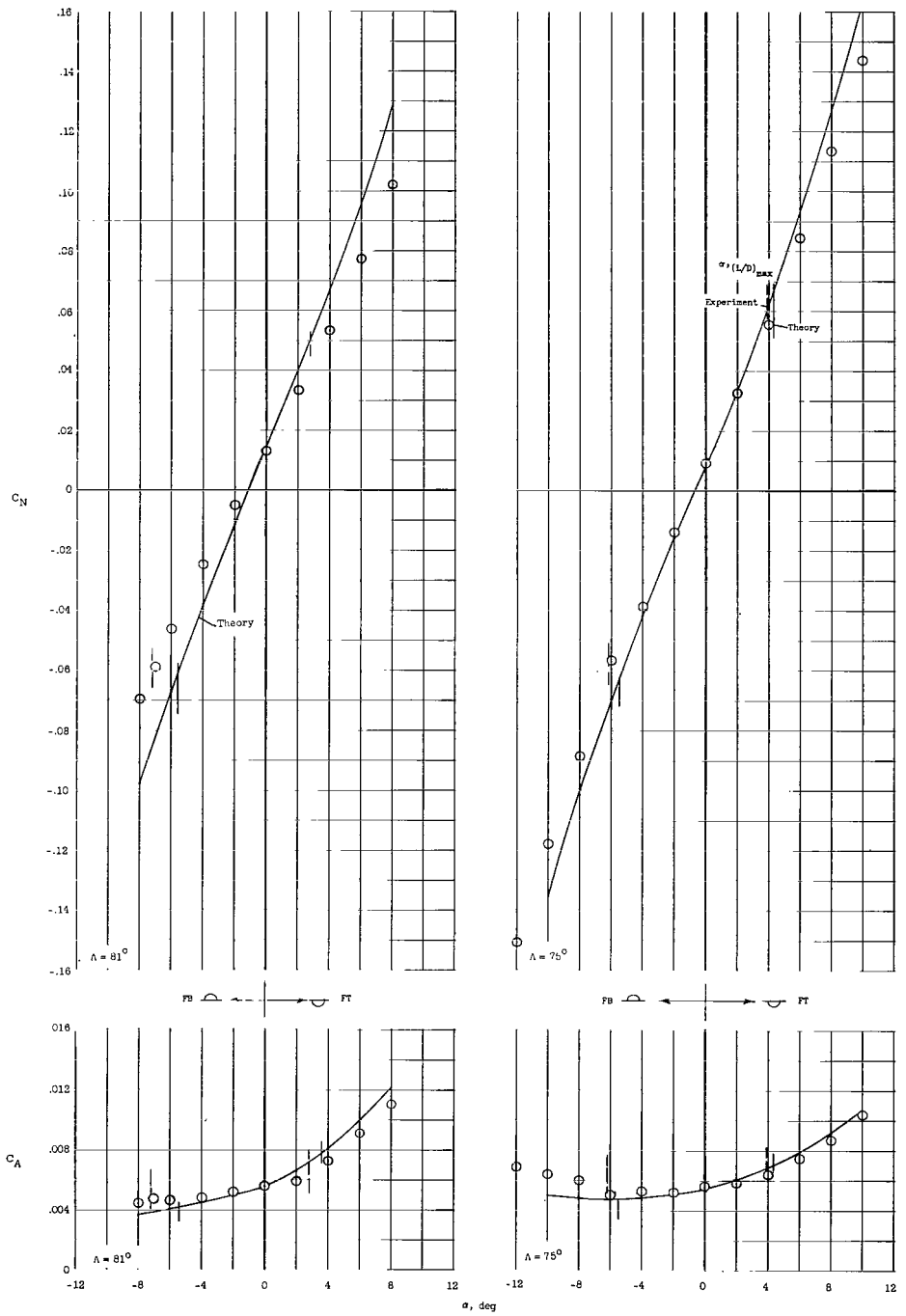

(b) Variation of C_N and C_A with α. $\theta = 5^\circ$.

Figure 6.- Continued.

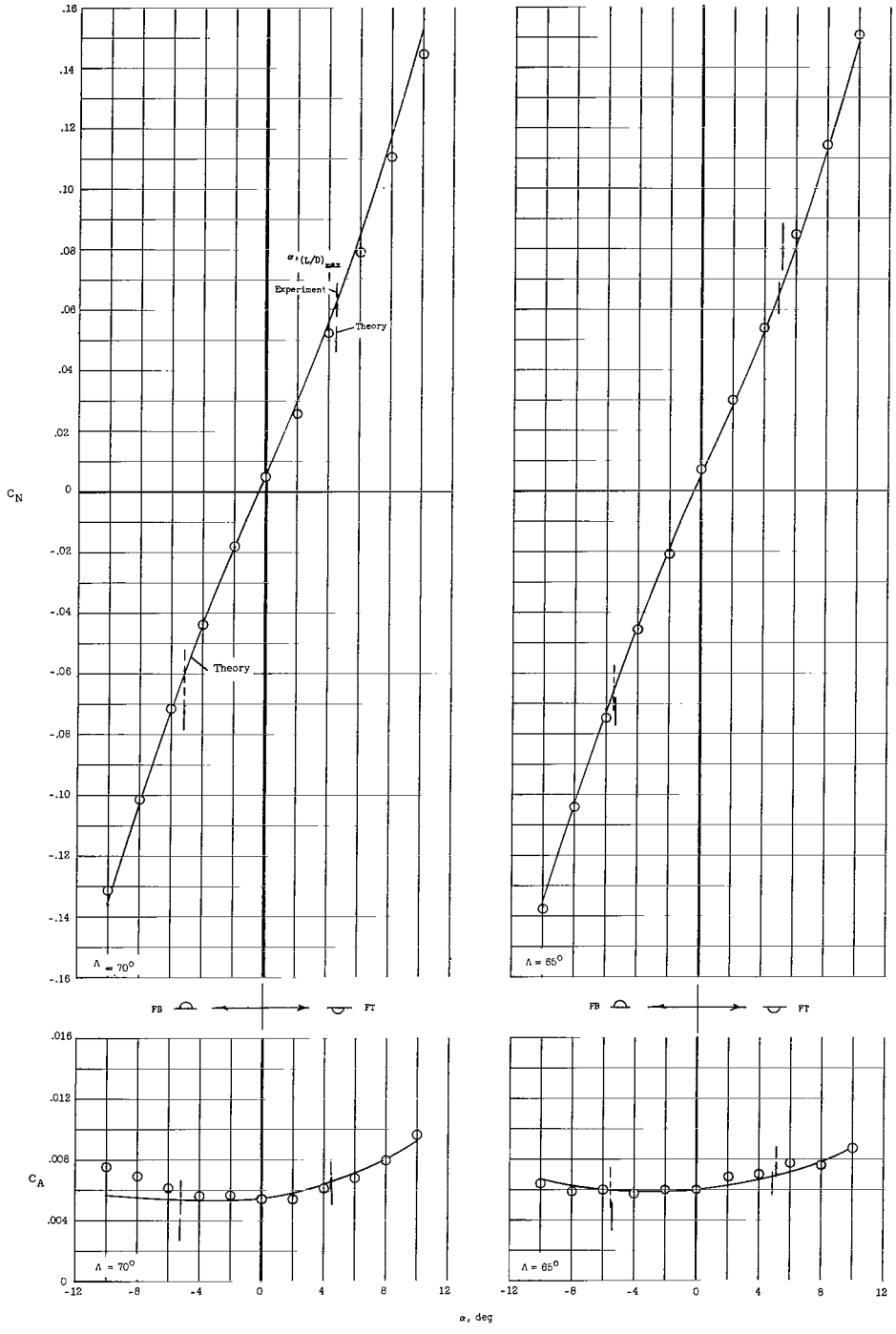

(b) Concluded.

Figure 6.- Continued.

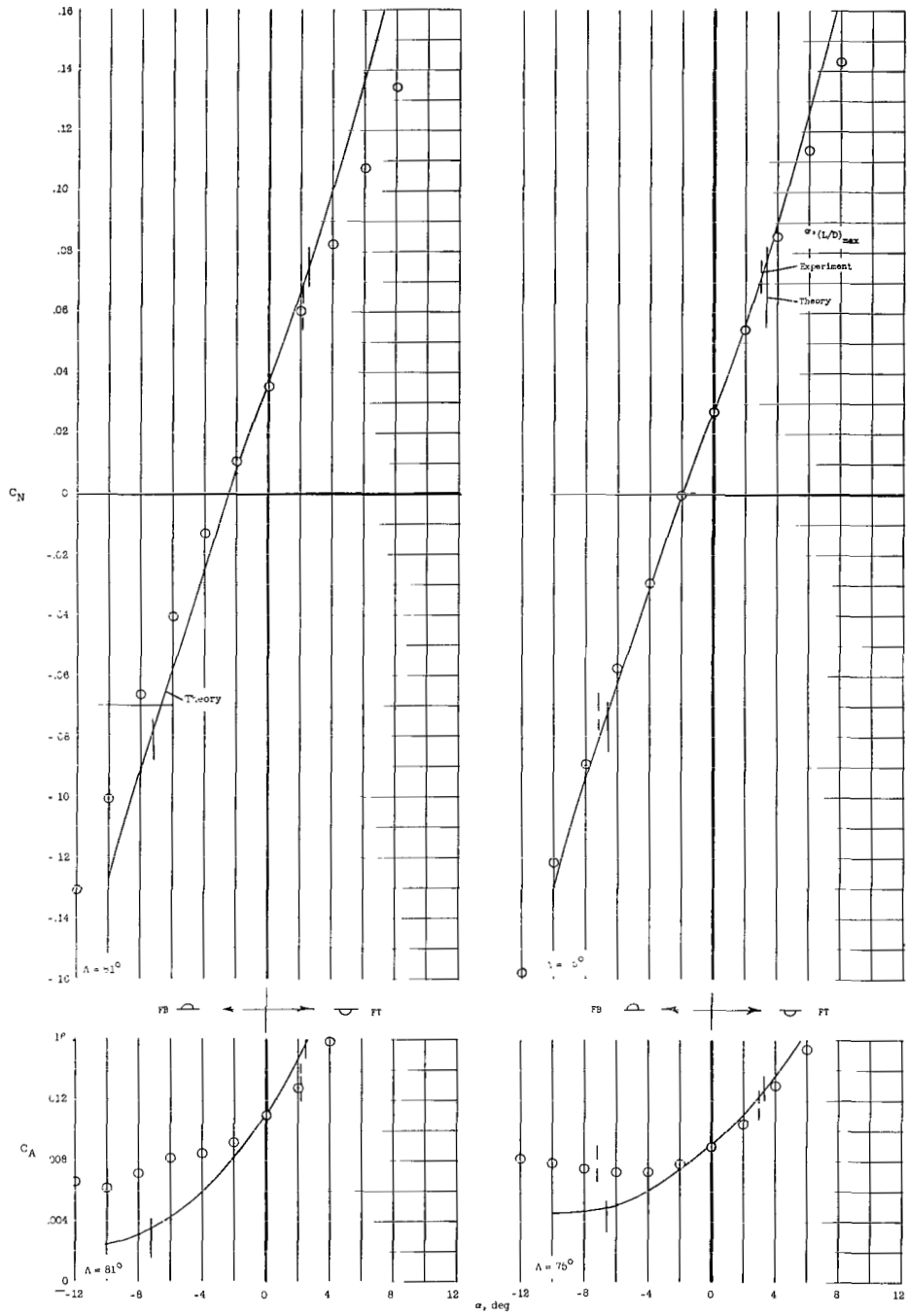

(c) Variation of C_N and C_A with α. $\theta = 7.5°$.

Figure 6.- Continued.

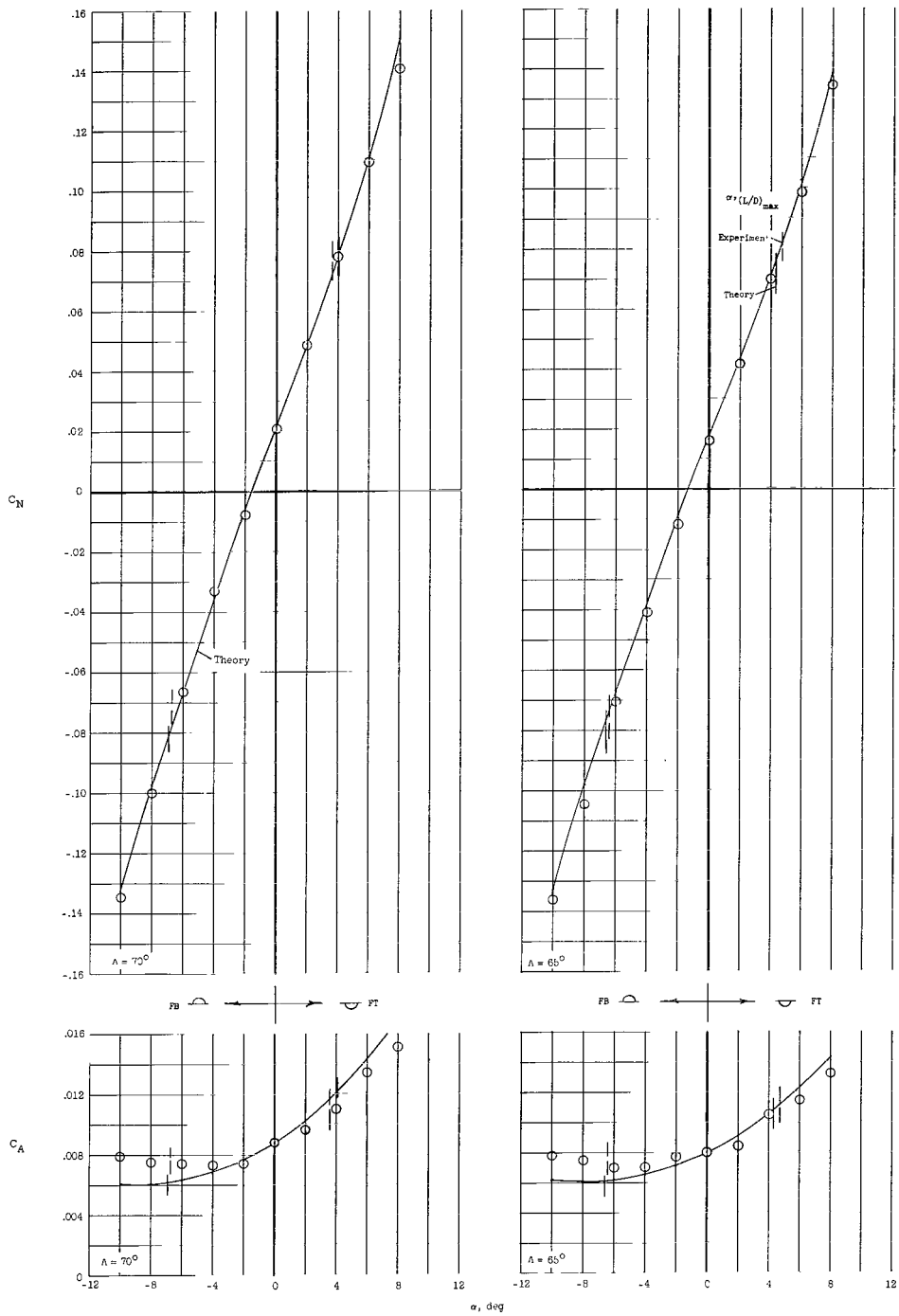

(c) Concluded.

Figure 6.- Concluded.

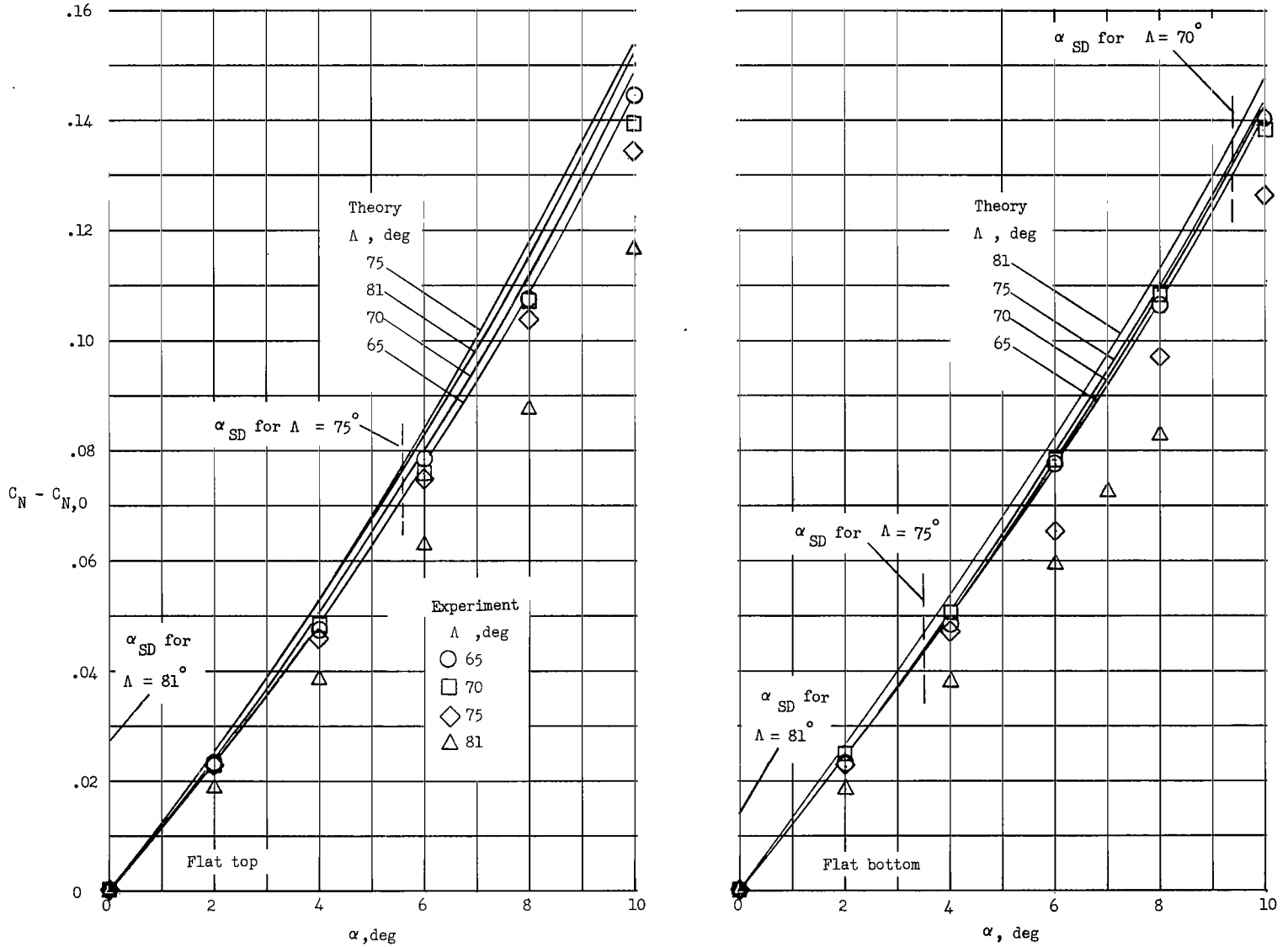

Figure 7.- Effect of leading-edge sweep on the normal-force characteristics of a 5° half-cone delta-wing combination.

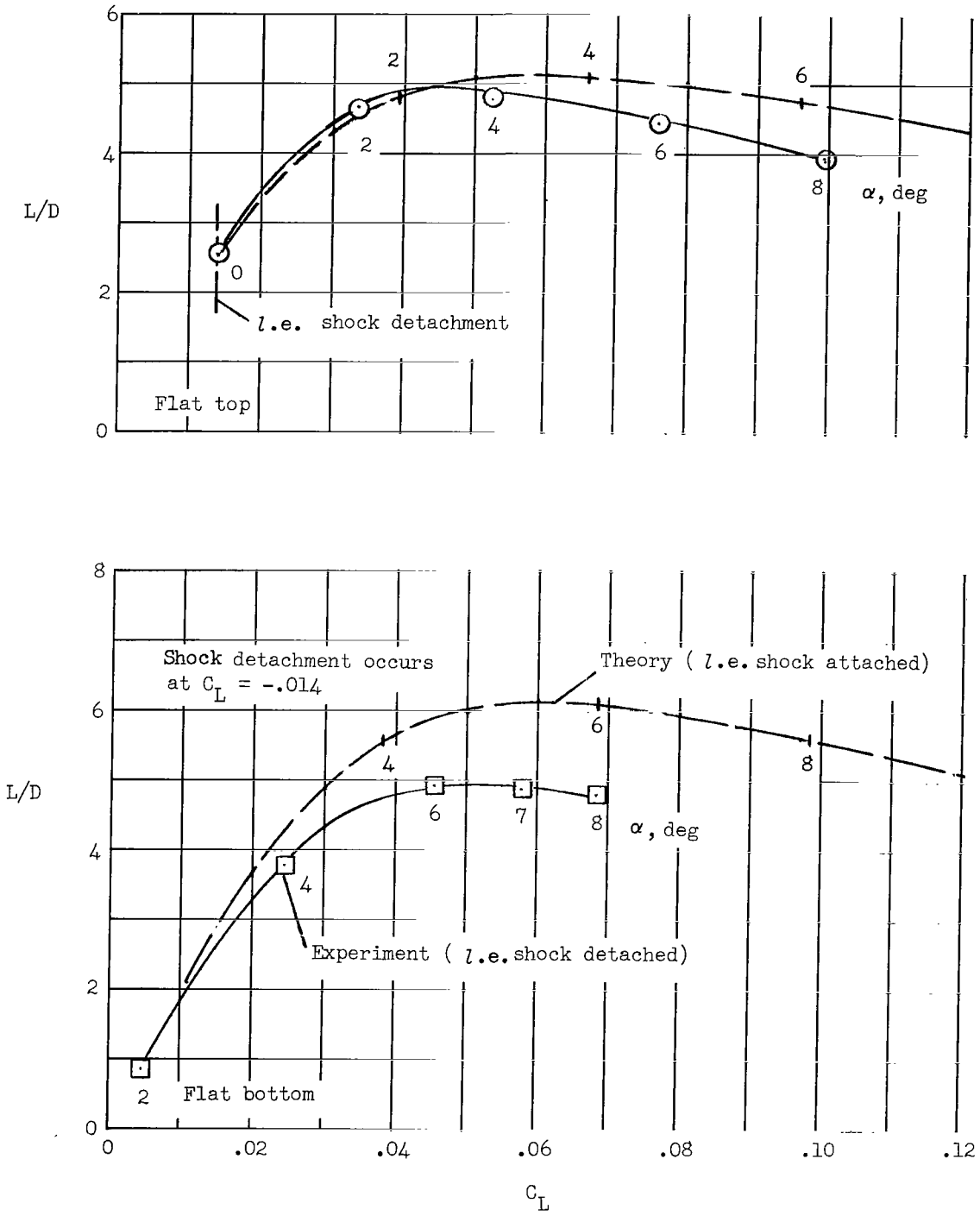

(a) $\Lambda = 81^\circ$.

Figure 8.- Lift-drag-ratio characteristics for a 5° half-cone delta-wing combination.

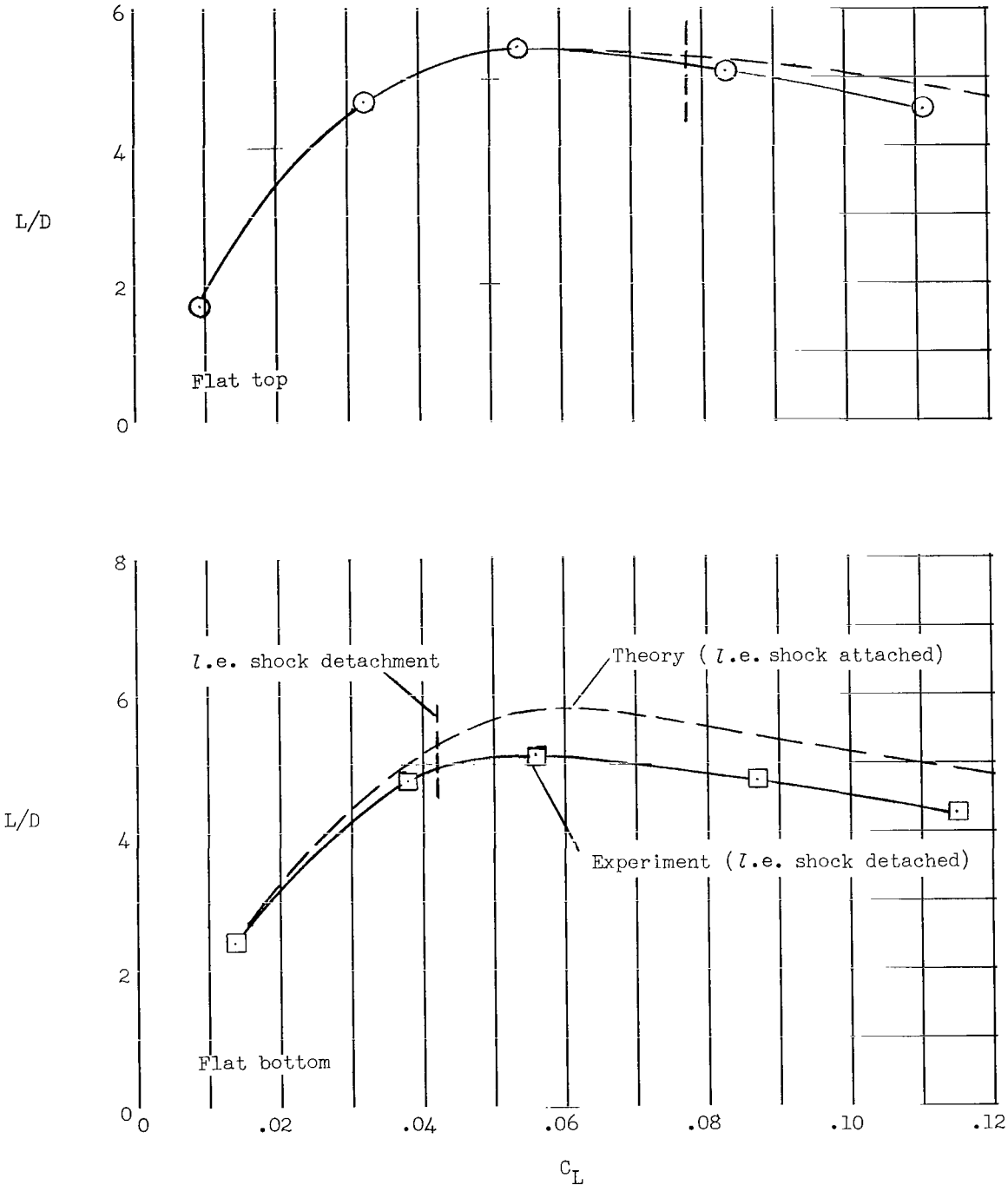

(b) $\Lambda = 75^{\circ}$.

Figure 8.- Concluded.

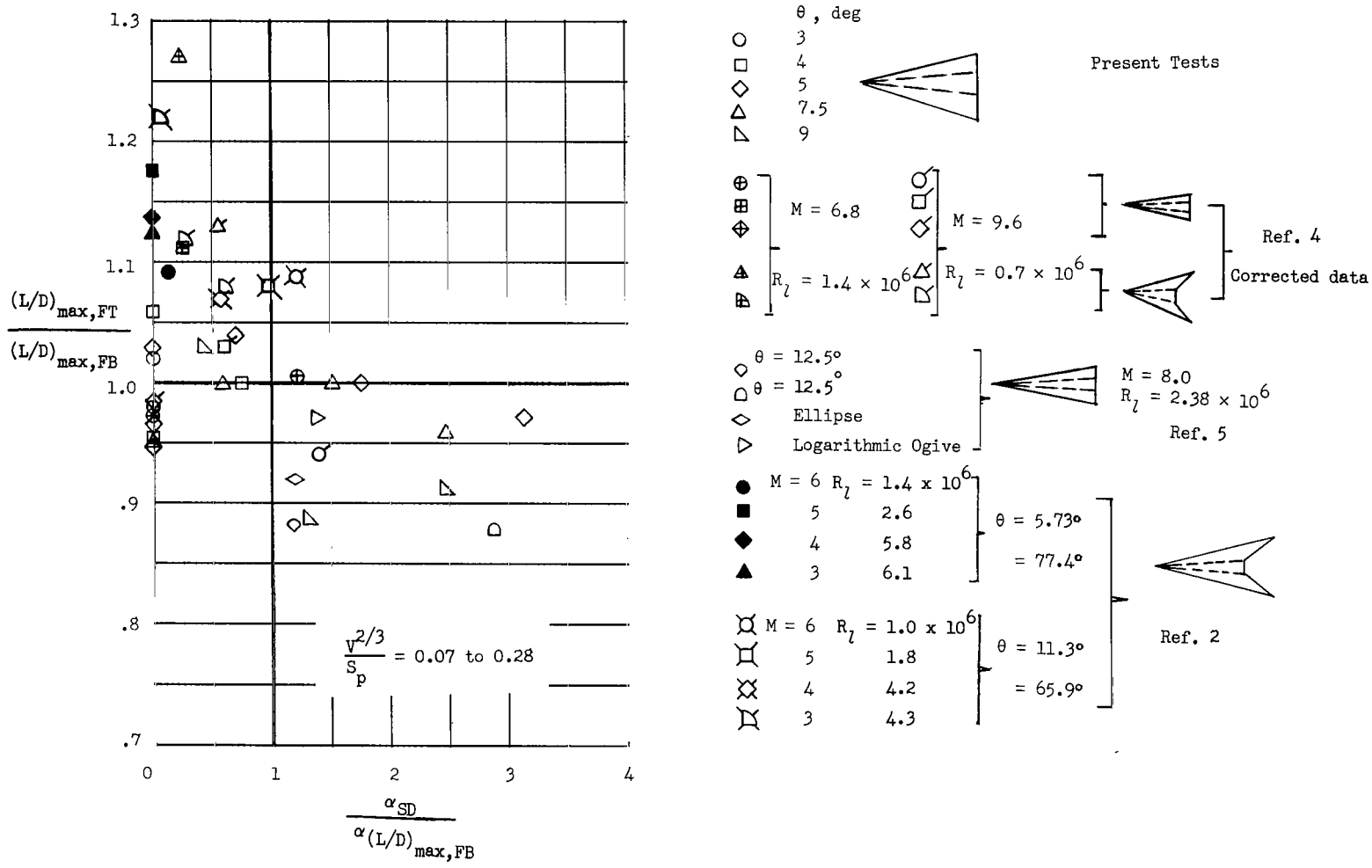

Figure 9.- Effect of leading-edge shock-detachment angle on the relative performance of half-cone delta-wing configurations.

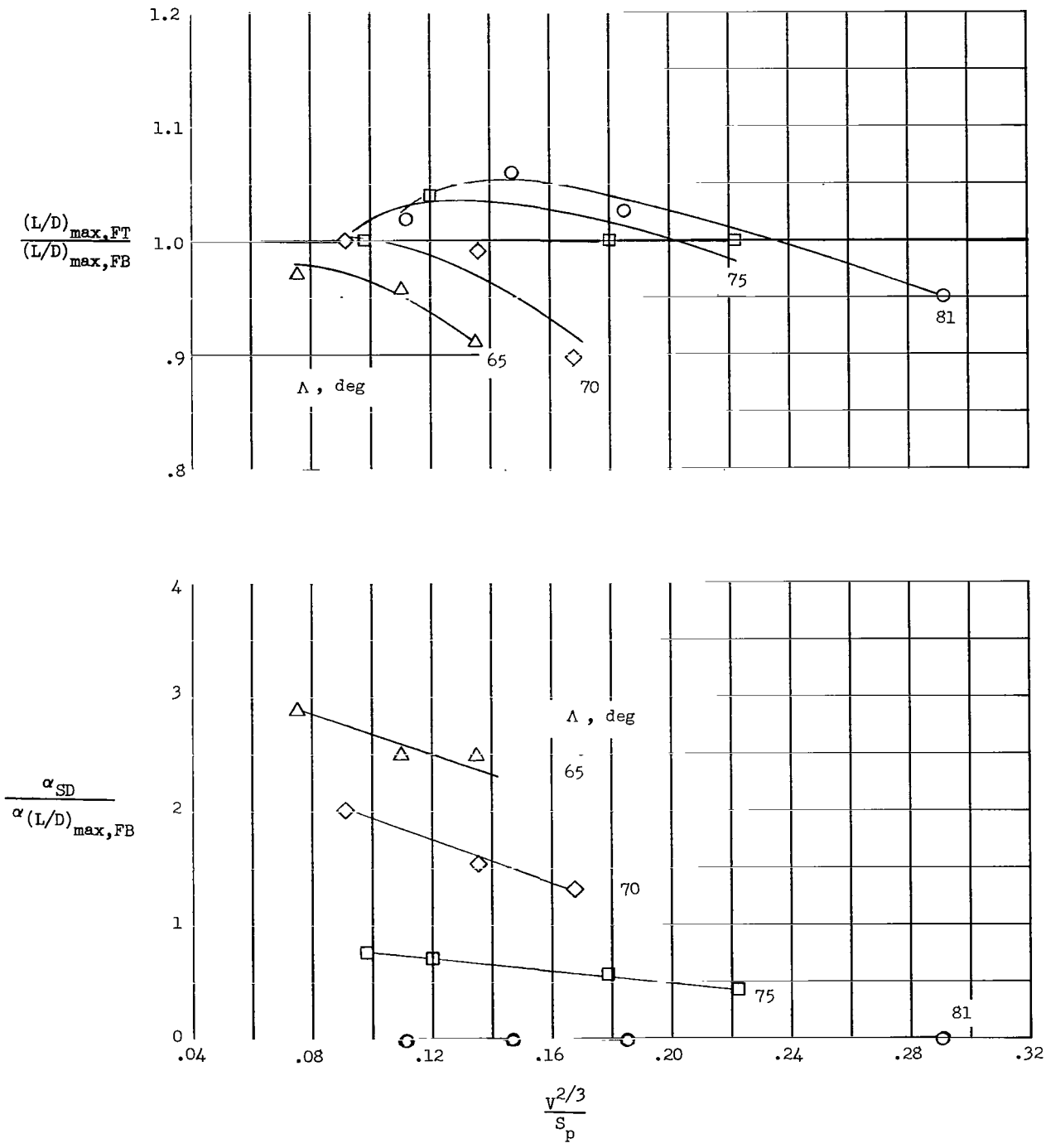

Figure 10.- Effect of volume parameter on relative performance and α-ratio for half-cone delta-wing configurations. M = 6.8; R_l = 1.4 × 10^6.

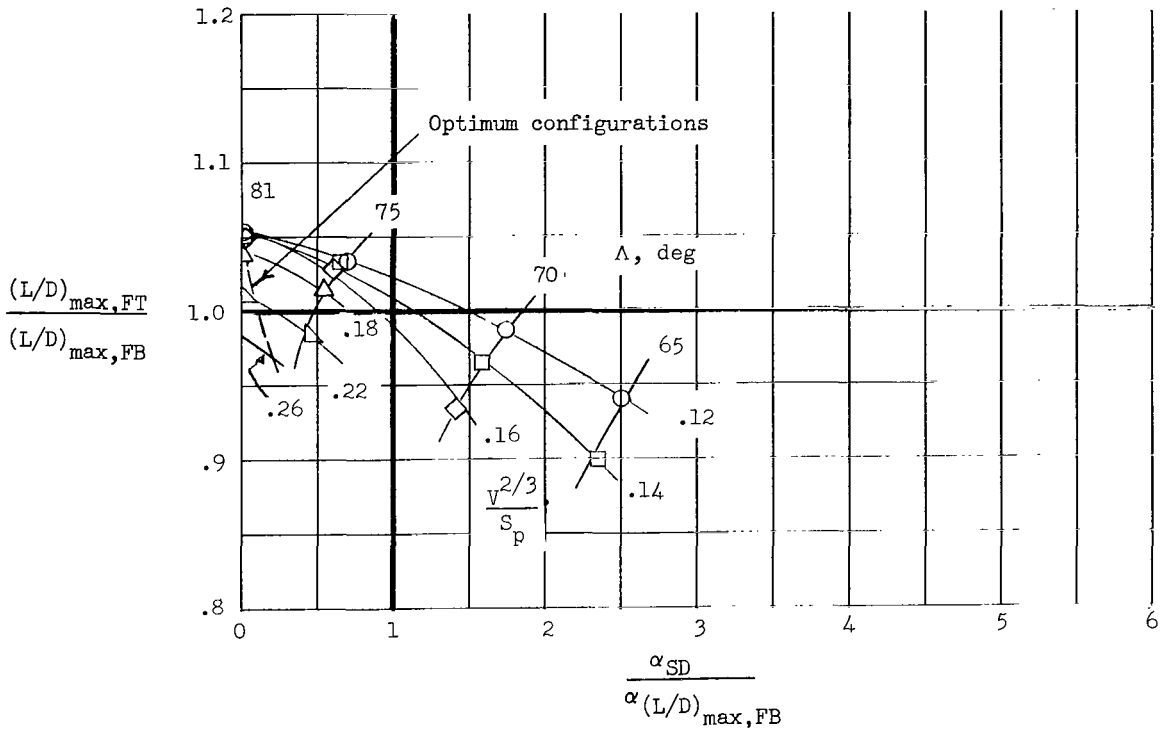

Figure 11.- Effect of leading-edge shock detachment. M = 6.8; $R_l = 1.4 \times 10^6$.

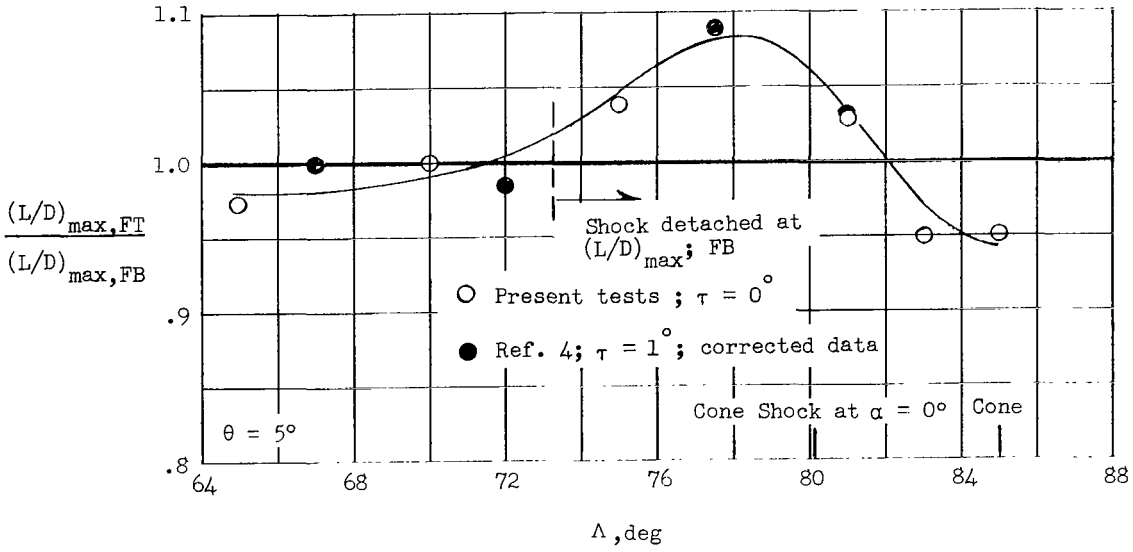

Figure 12.- Effect of wing-leading-edge sweep. M = 6.8; $R_l = 1.4 \times 10^6$.

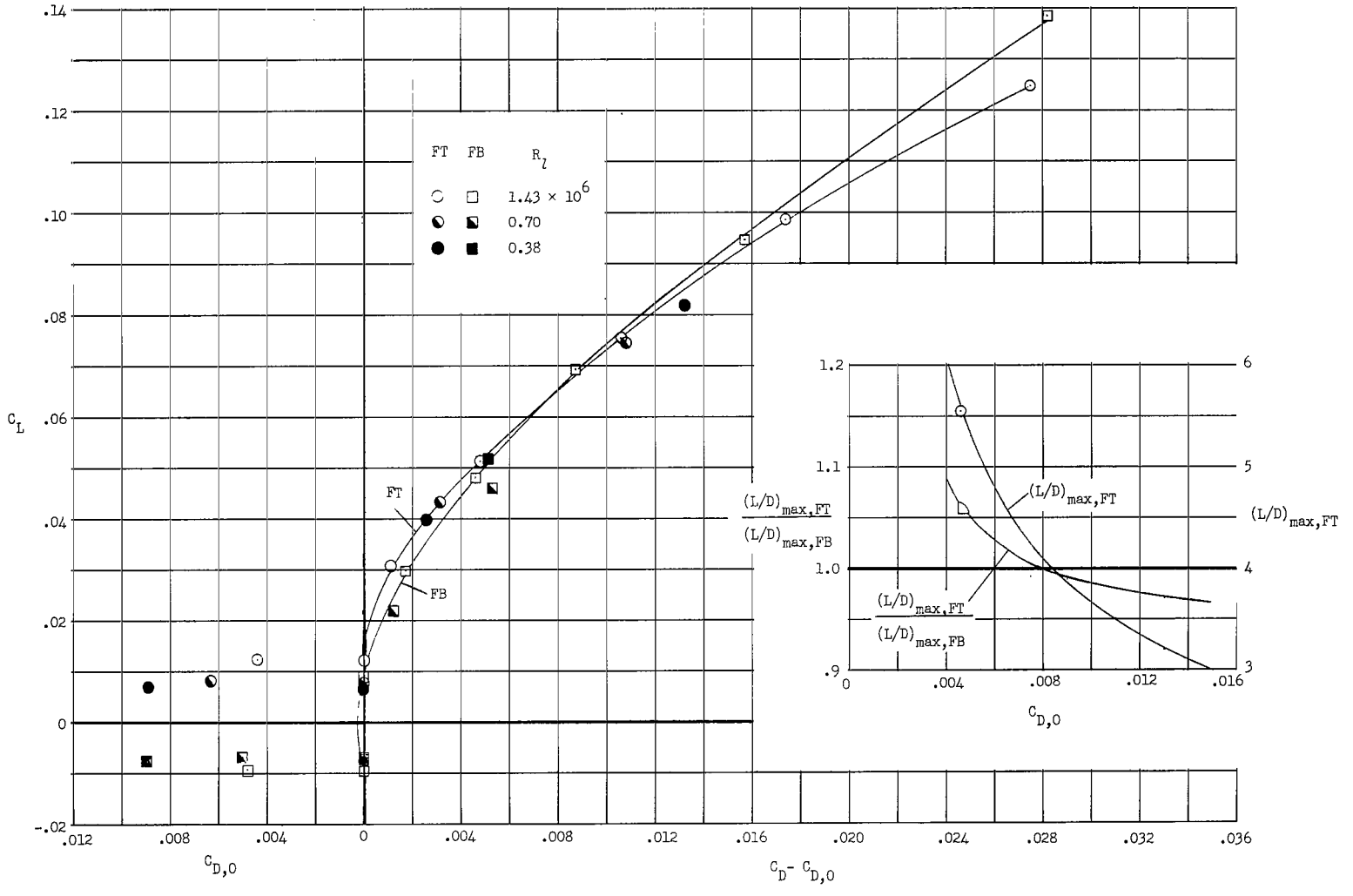

Figure 13.- Effect of $C_{D,0}$; $\theta = 4^o$; $\Lambda = 81^o$.

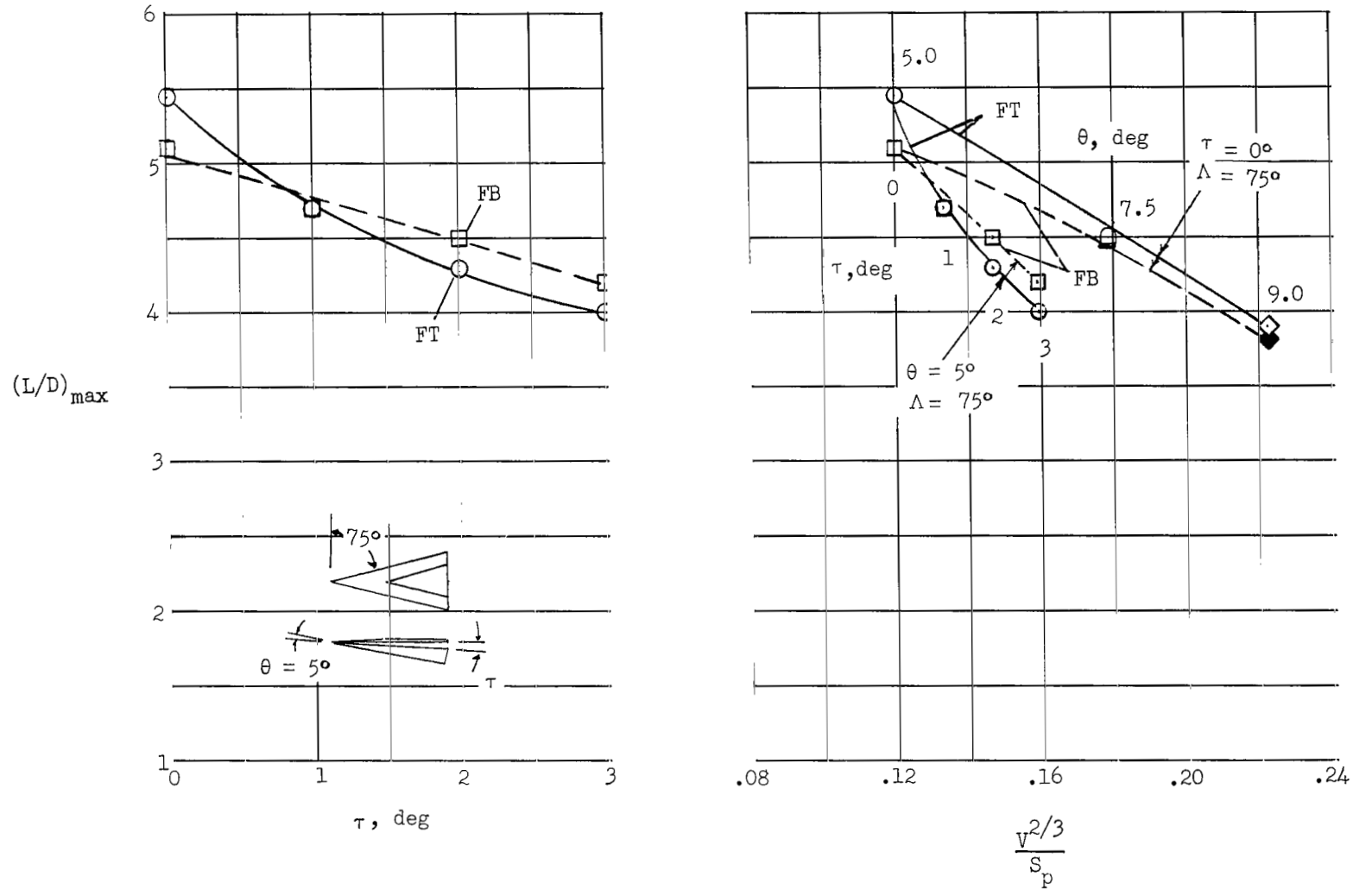

Figure 14.- Effect of cone offset on maximum lift-drag ratio.

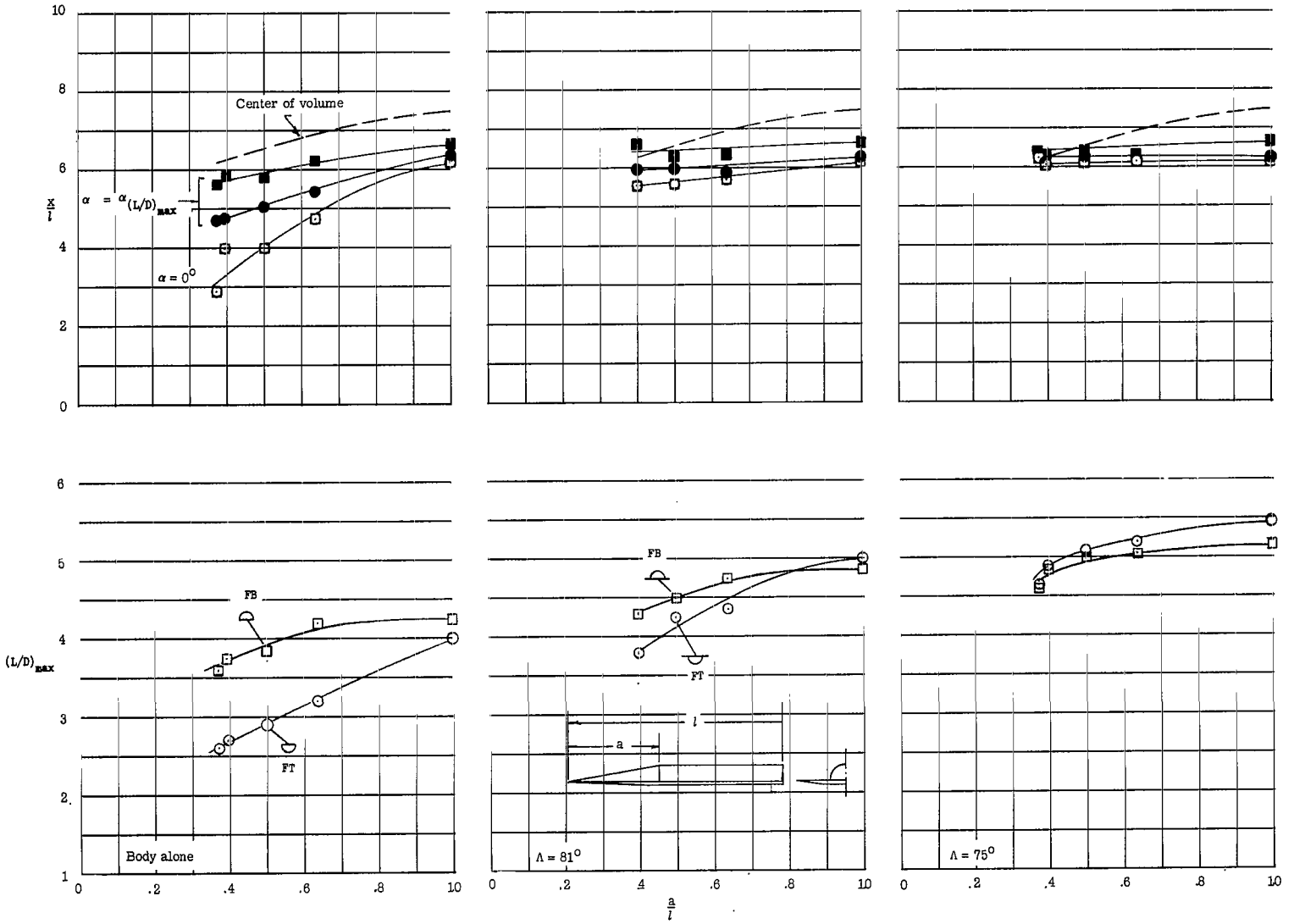

Figure 15.- Effect of changing body volume distribution on $(L/D)_{max}$ and aerodynamic-center location. Constant body volume.

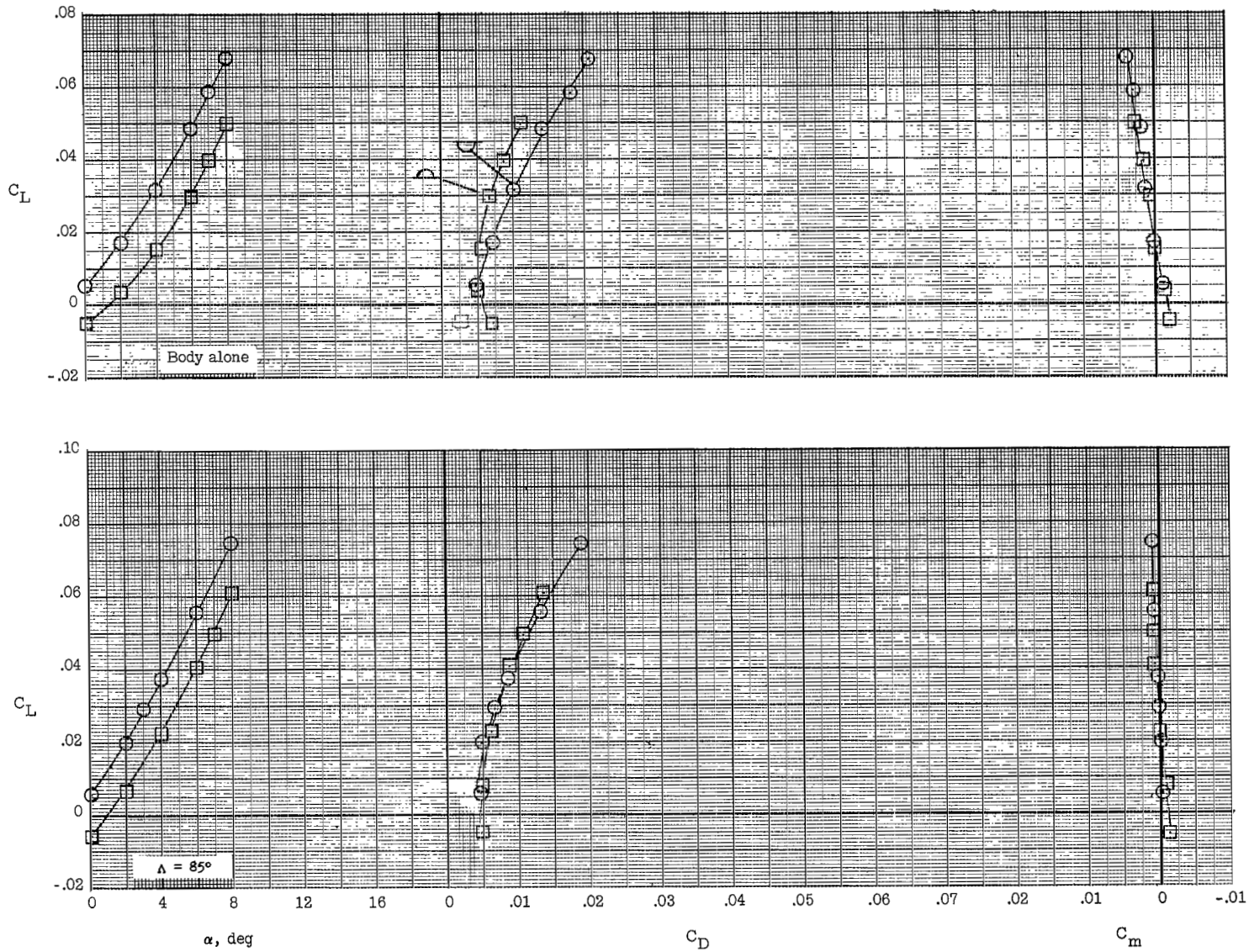

(a) $\theta = 3^{\circ}$.

Figure 16.- Aerodynamic characteristics in pitch for half-cone delta-wing combinations.

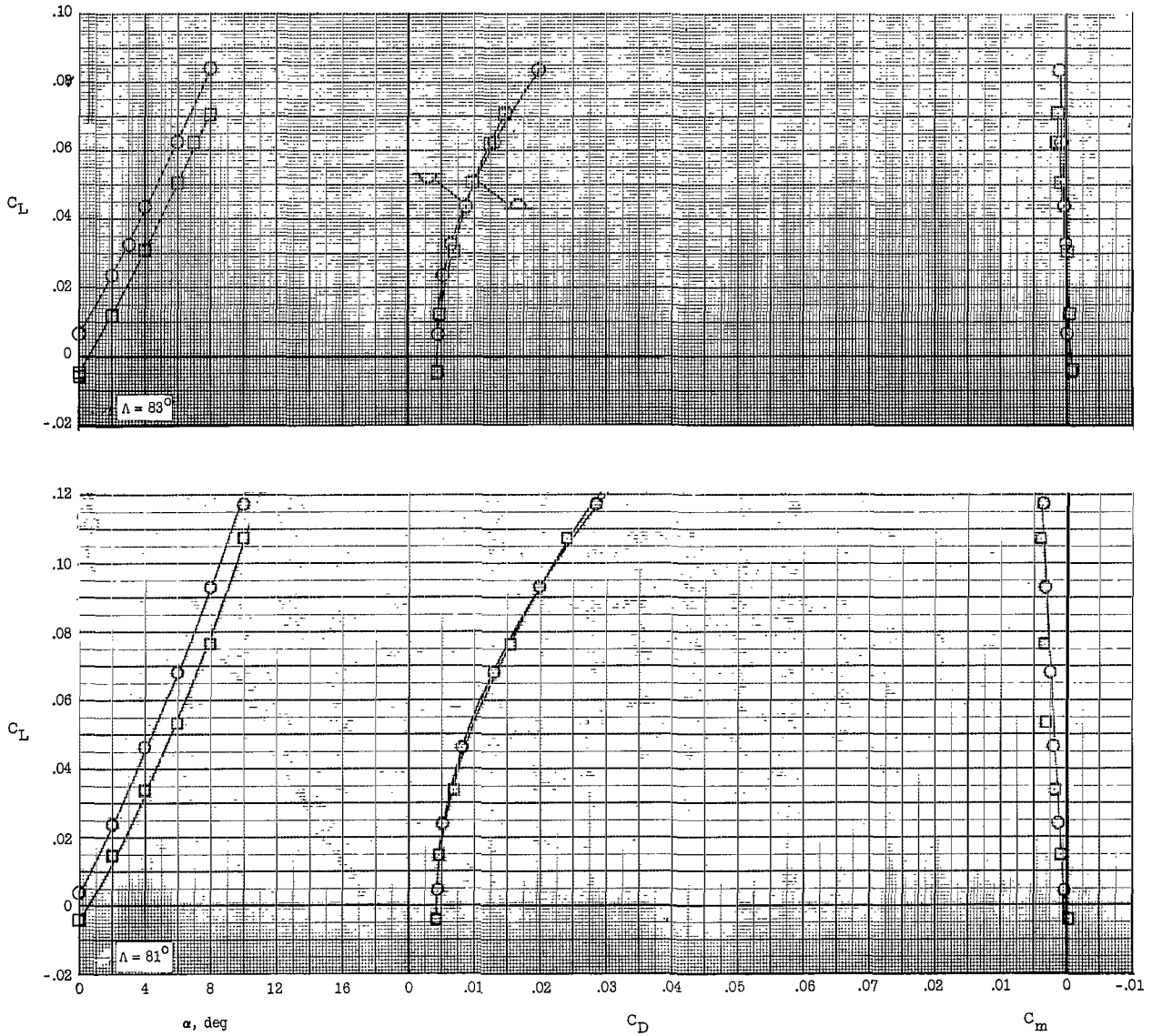

(a) Concluded.

Figure 16.- Continued.

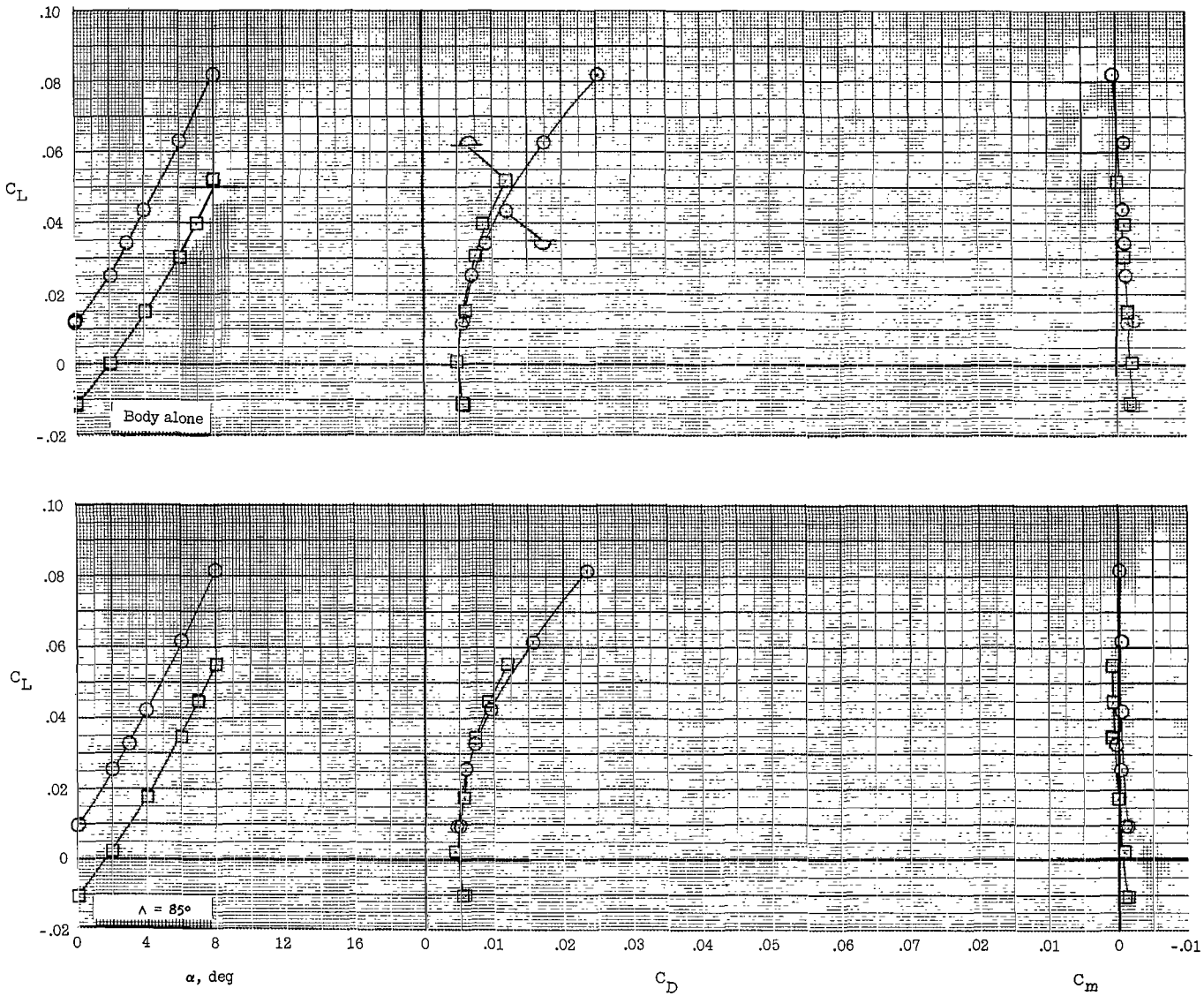

(b) $\theta = 4^\circ$.

Figure 16.- Continued.

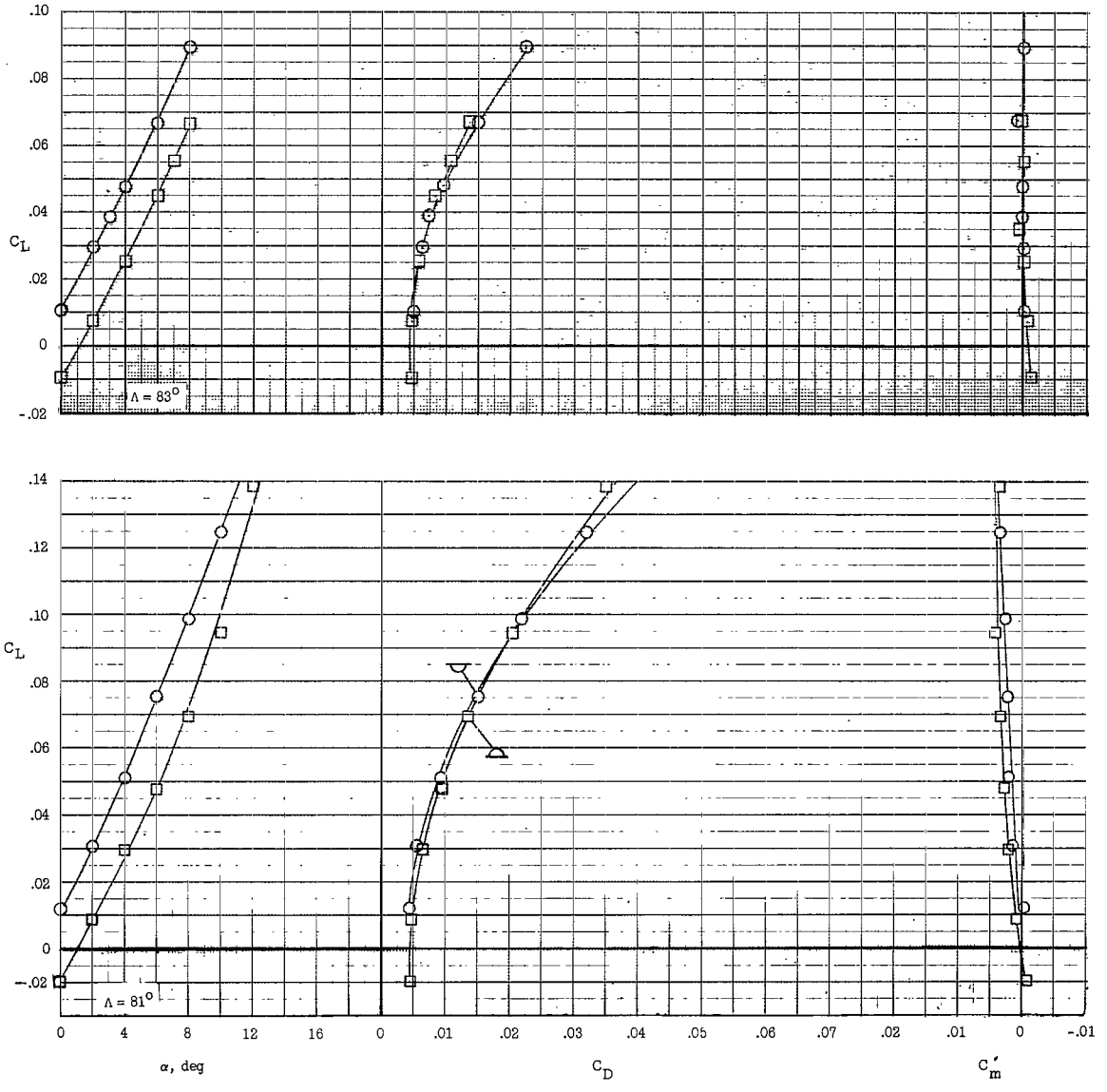

(b) Continued.

Figure 16.- Continued.

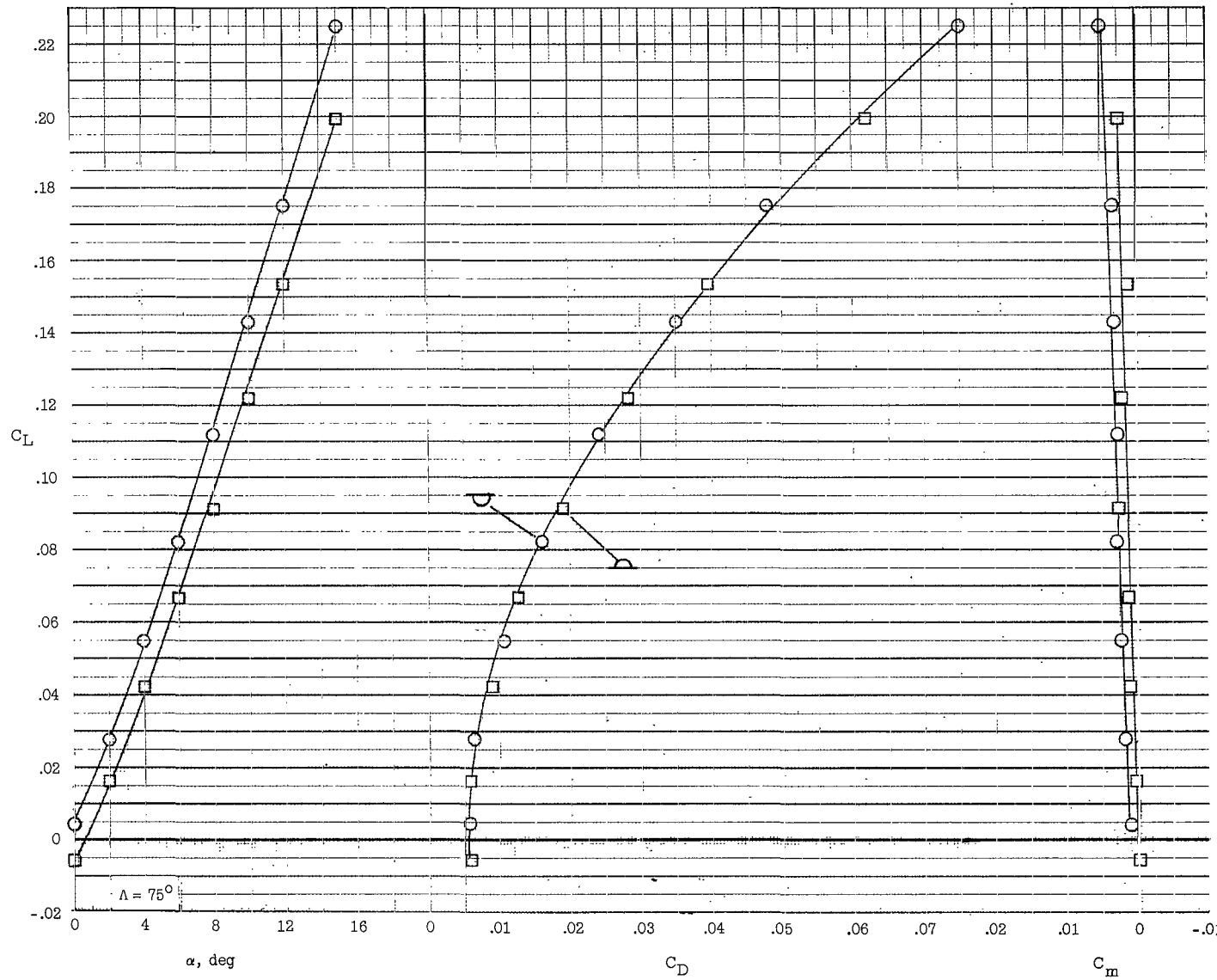

(b) Concluded.

Figure 16.- Continued.

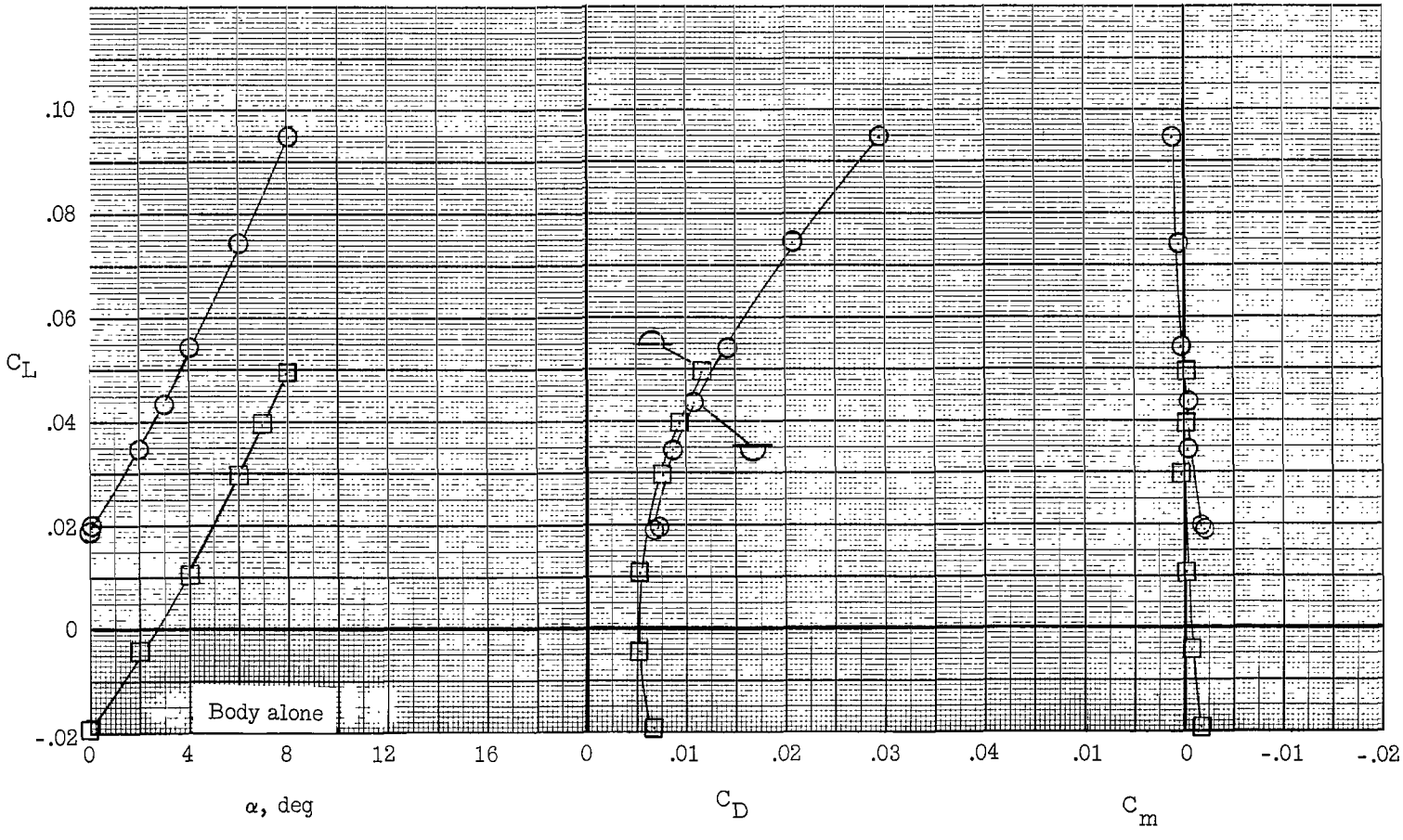

(c) $\theta = 5°$.

Figure 16.- Continued.

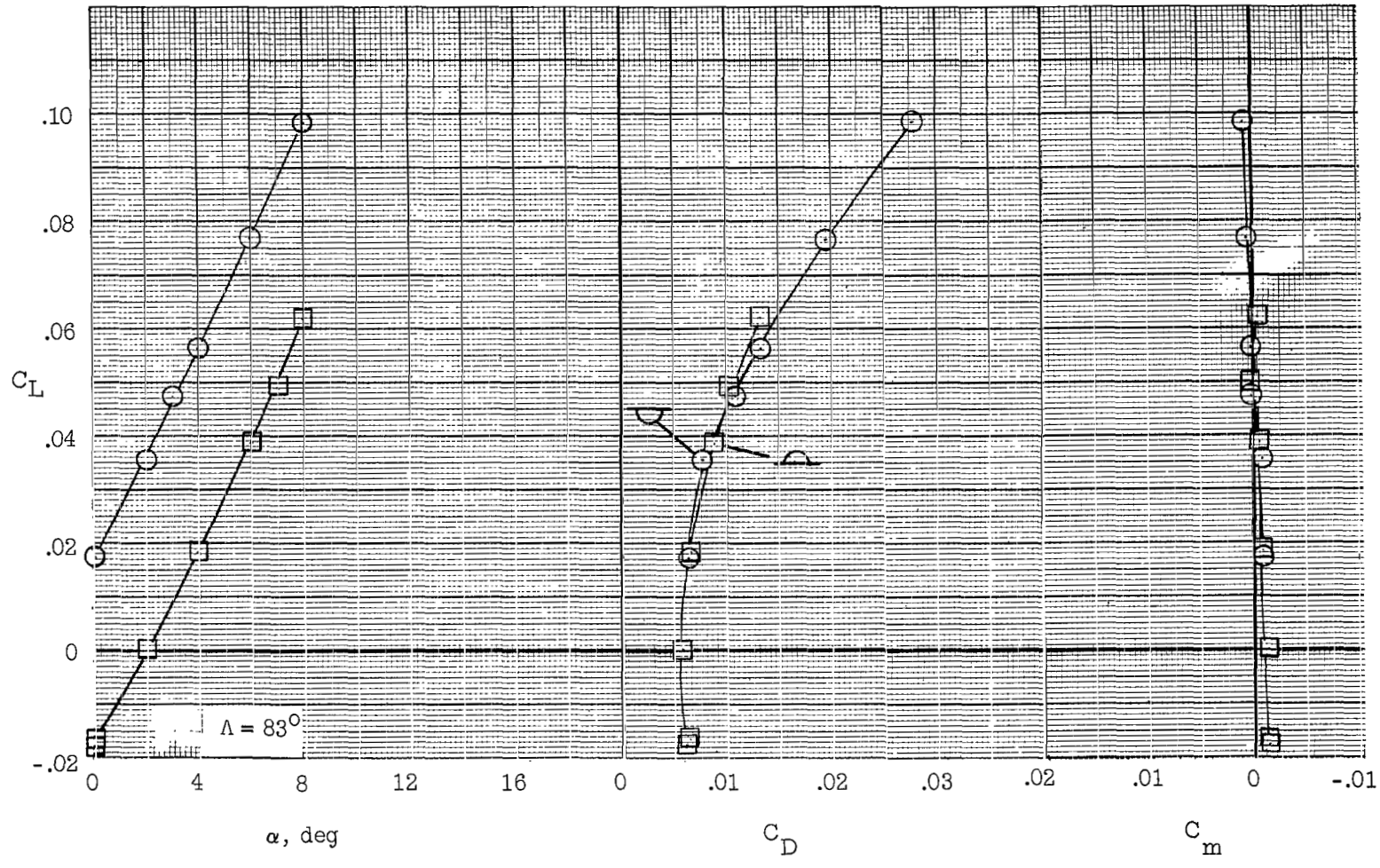

(c) Continued.

Figure 16.- Continued.

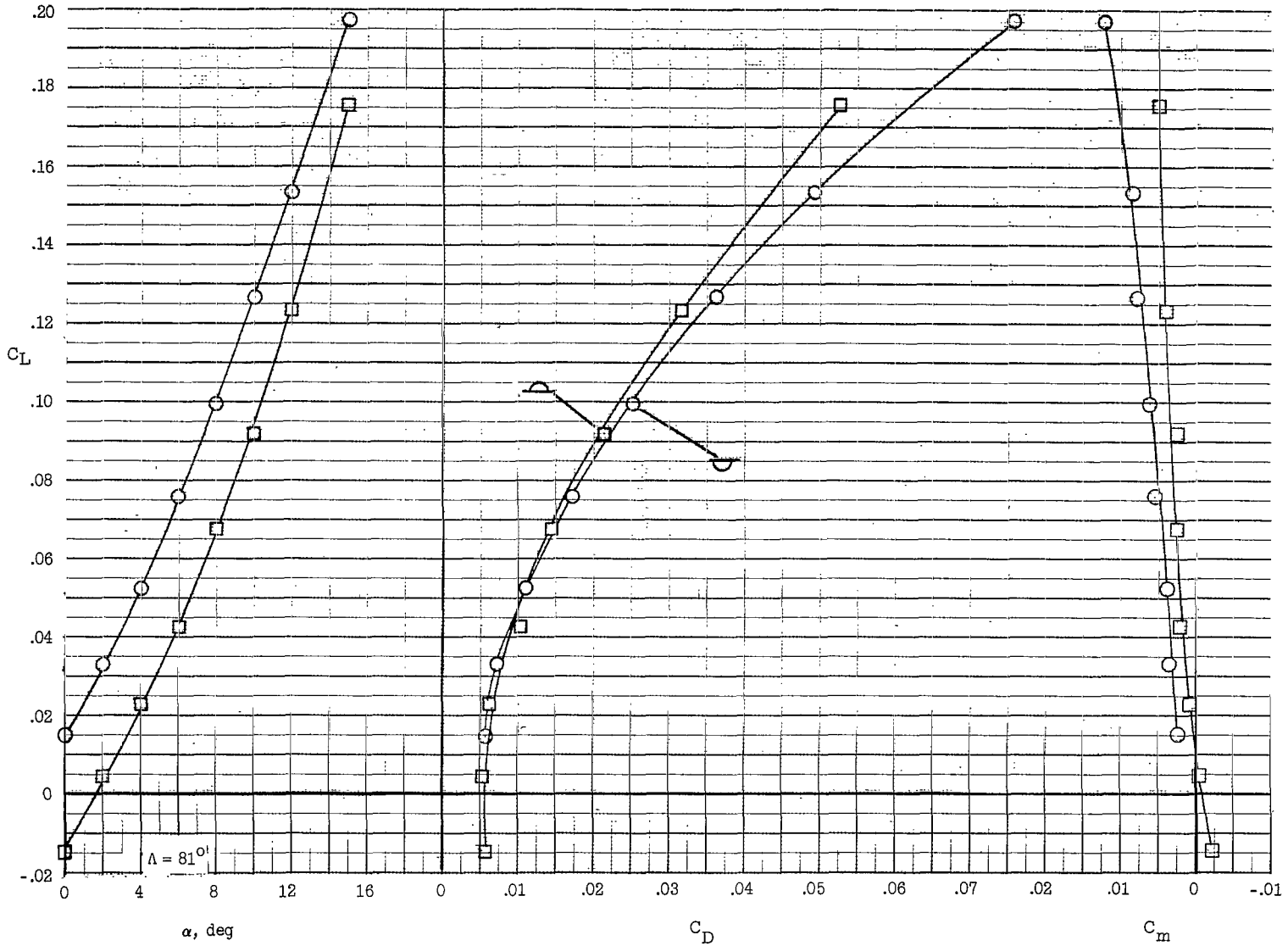

(c) Continued.

Figure 16.- Continued.

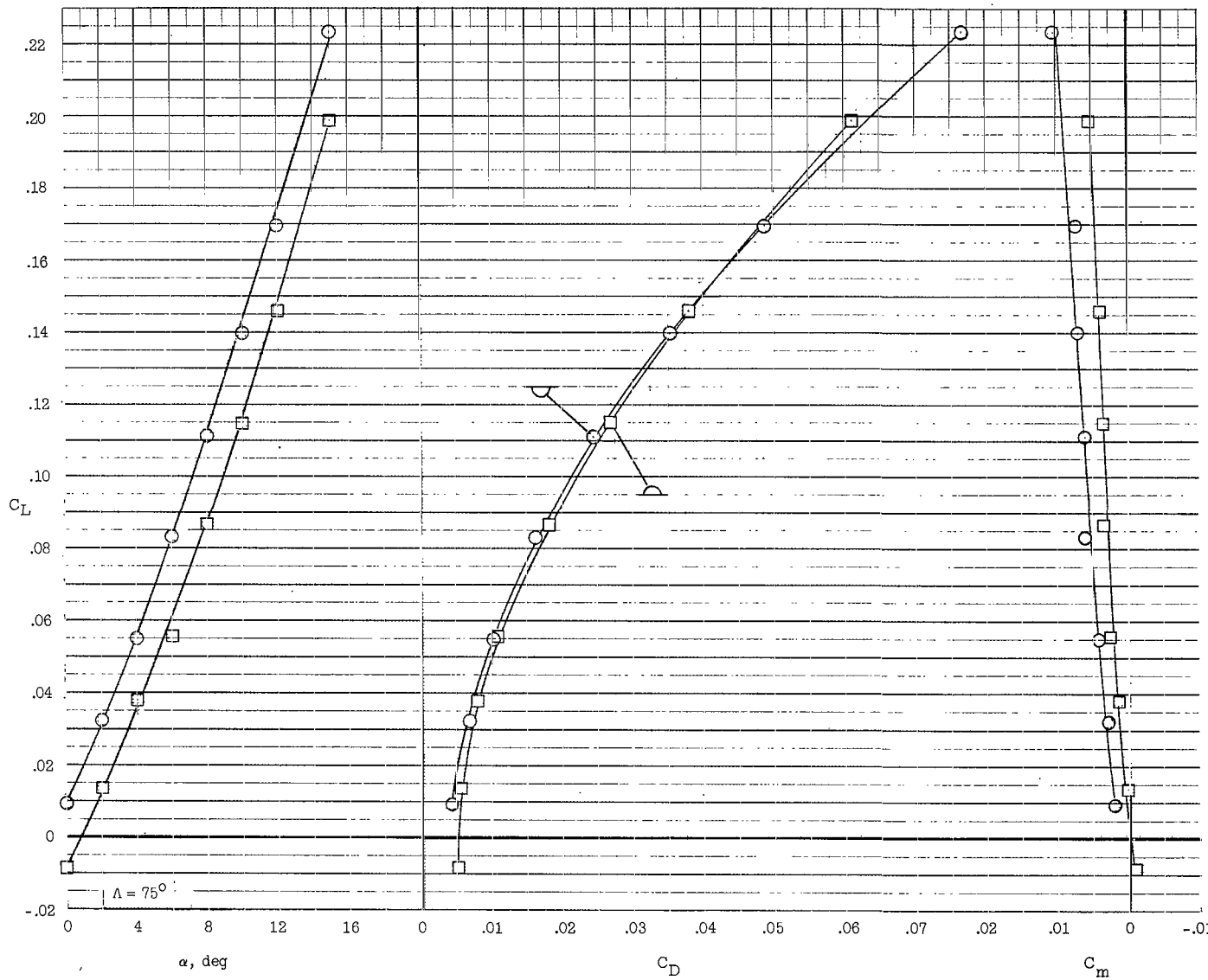

(c) Continued.

Figure 16.- Continued.

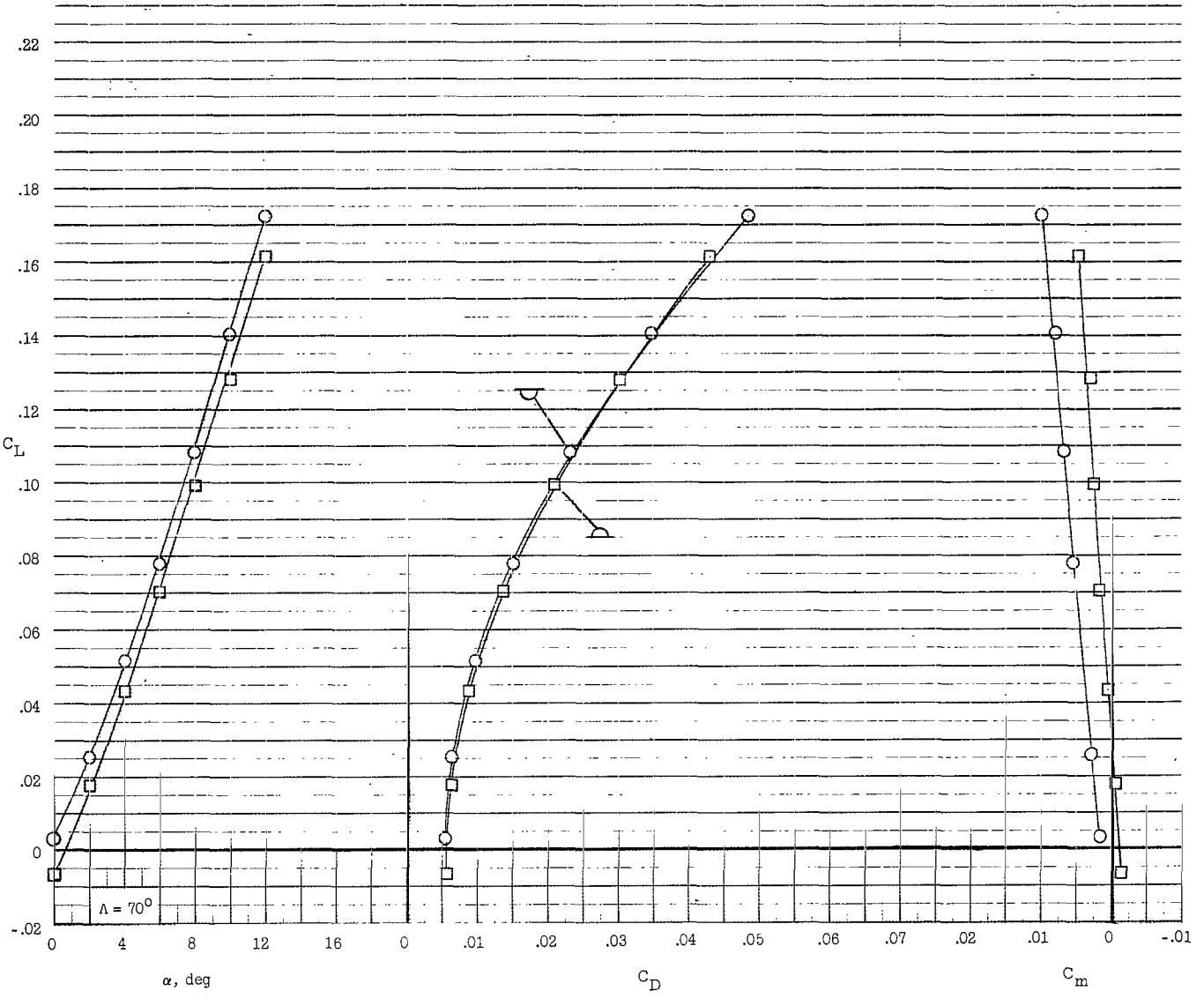

(c) Continued.

Figure 16.- Continued.

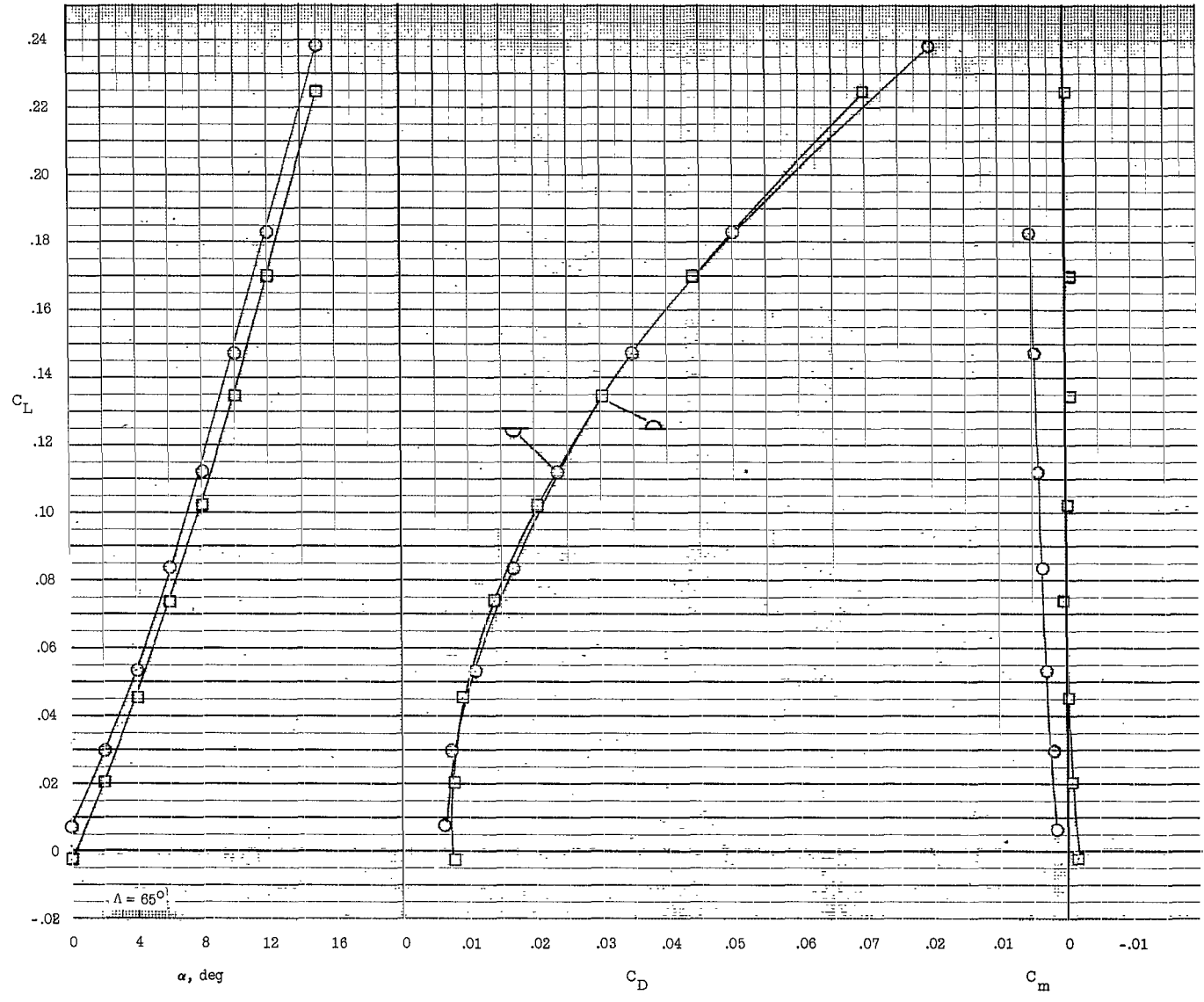

(c) Concluded.

Figure 16.- Continued.

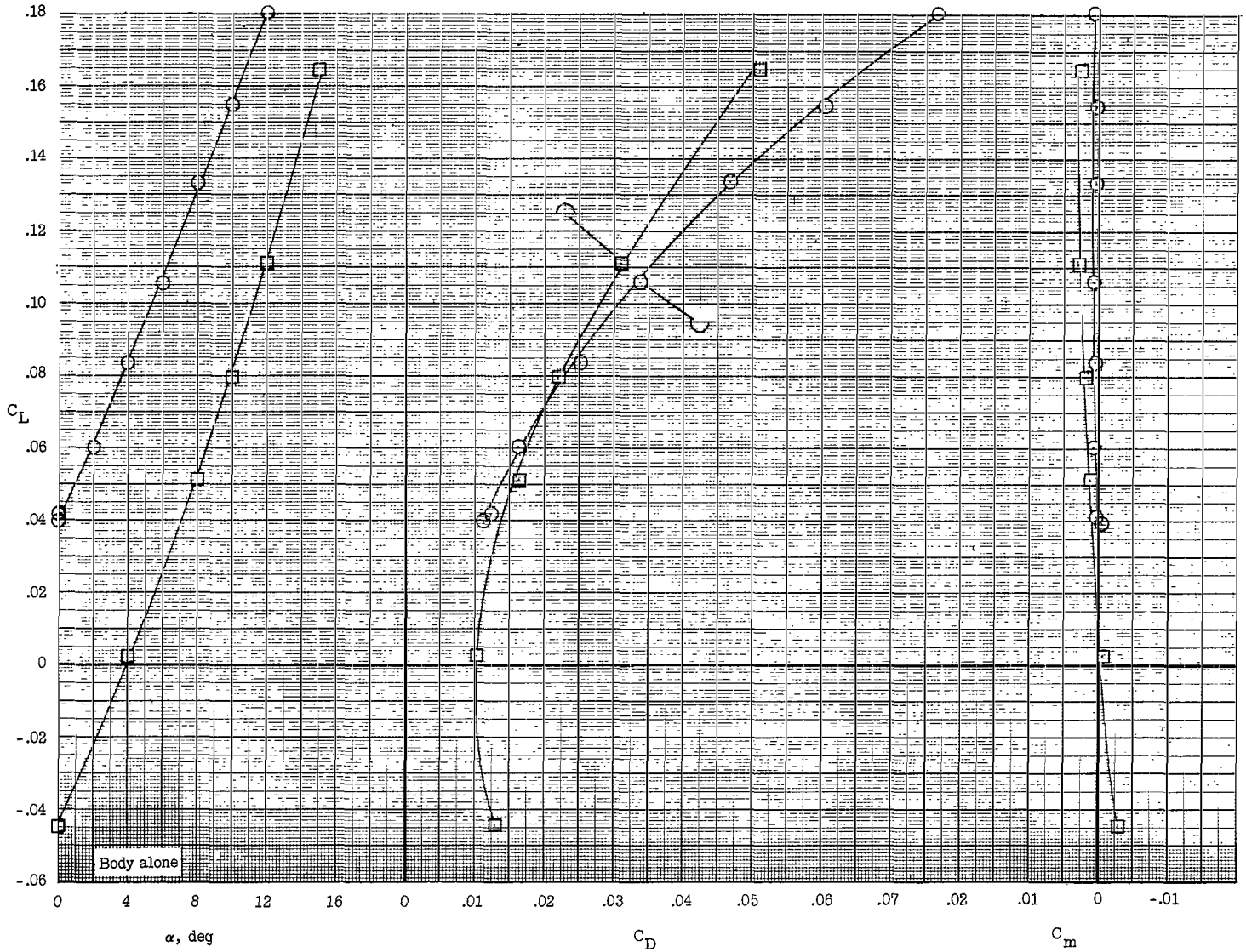

(d) $\theta = 7.5^{\circ}$.

Figure 16.- Continued.

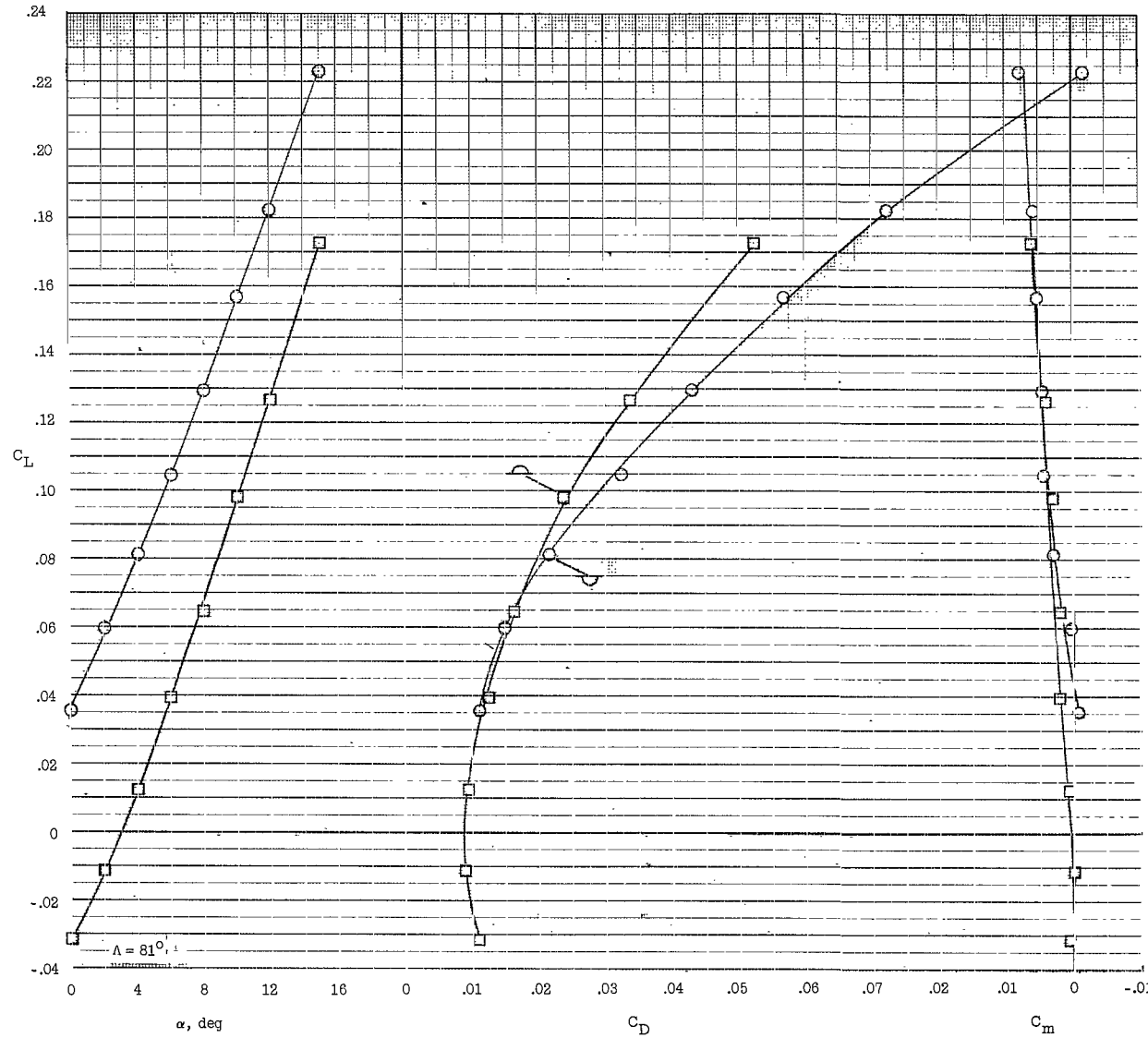

(d) Continued.

Figure 16.- Continued.

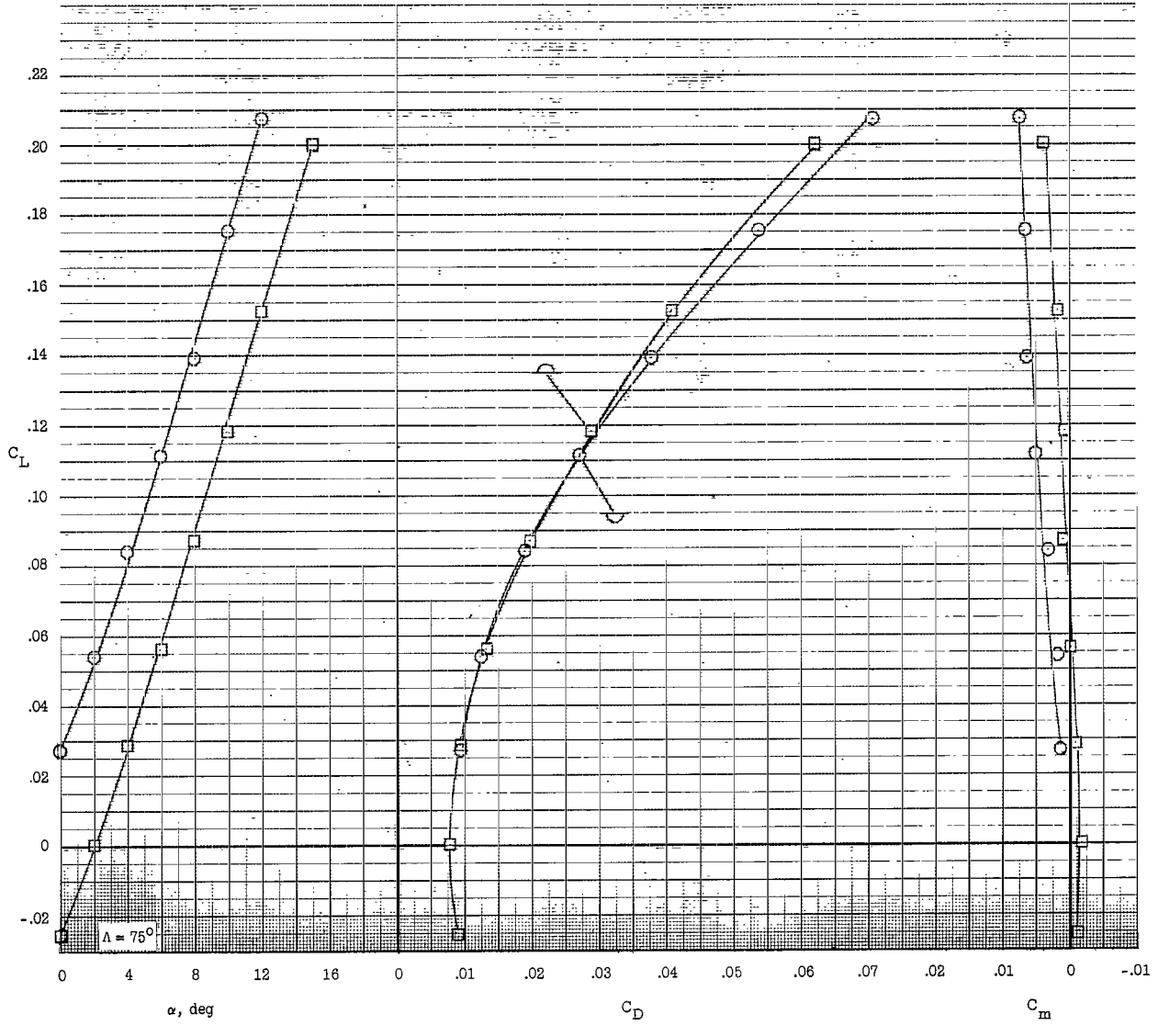

(d) Continued.

Figure 16.- Continued.

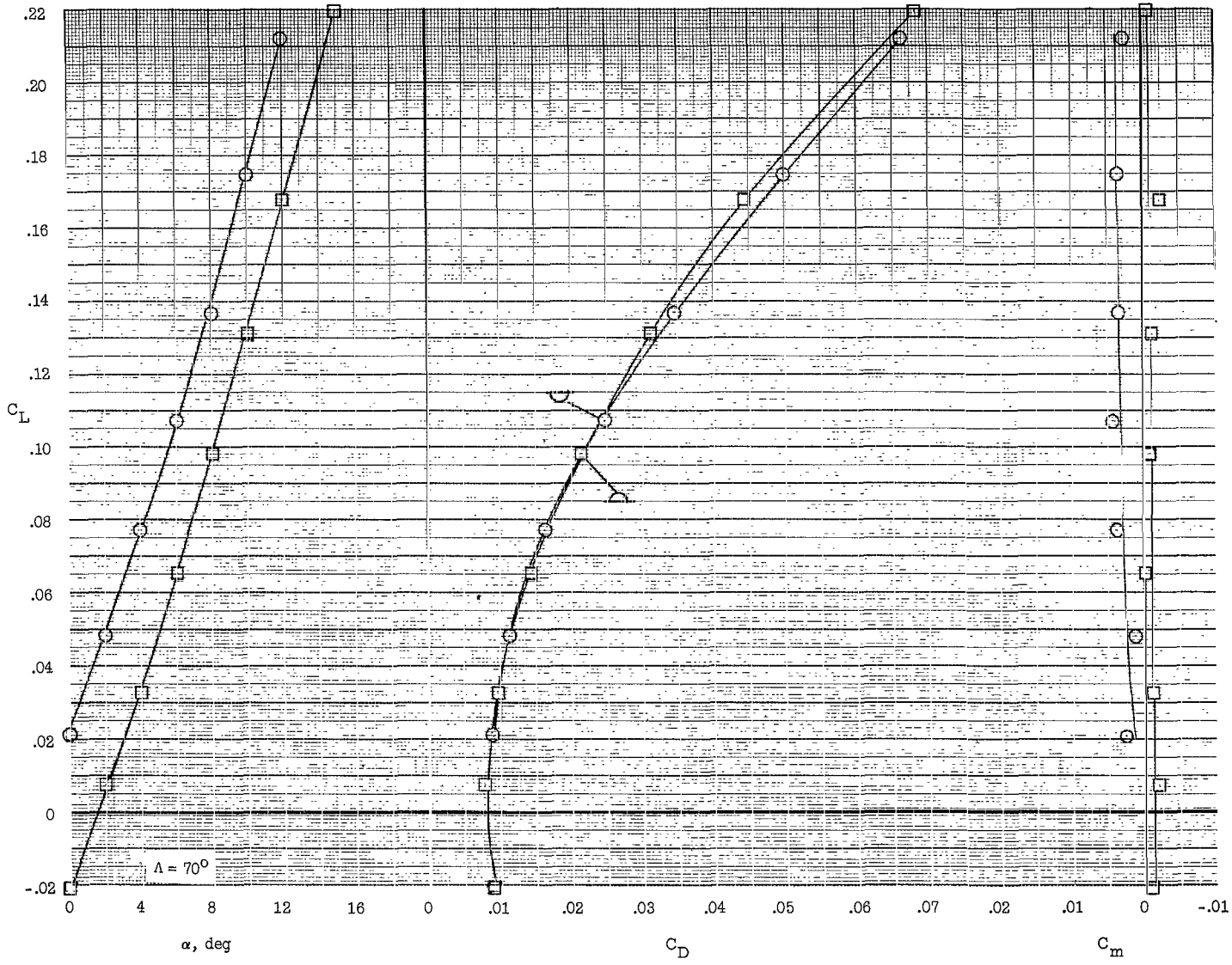

(d) Continued.

Figure 16.- Continued.

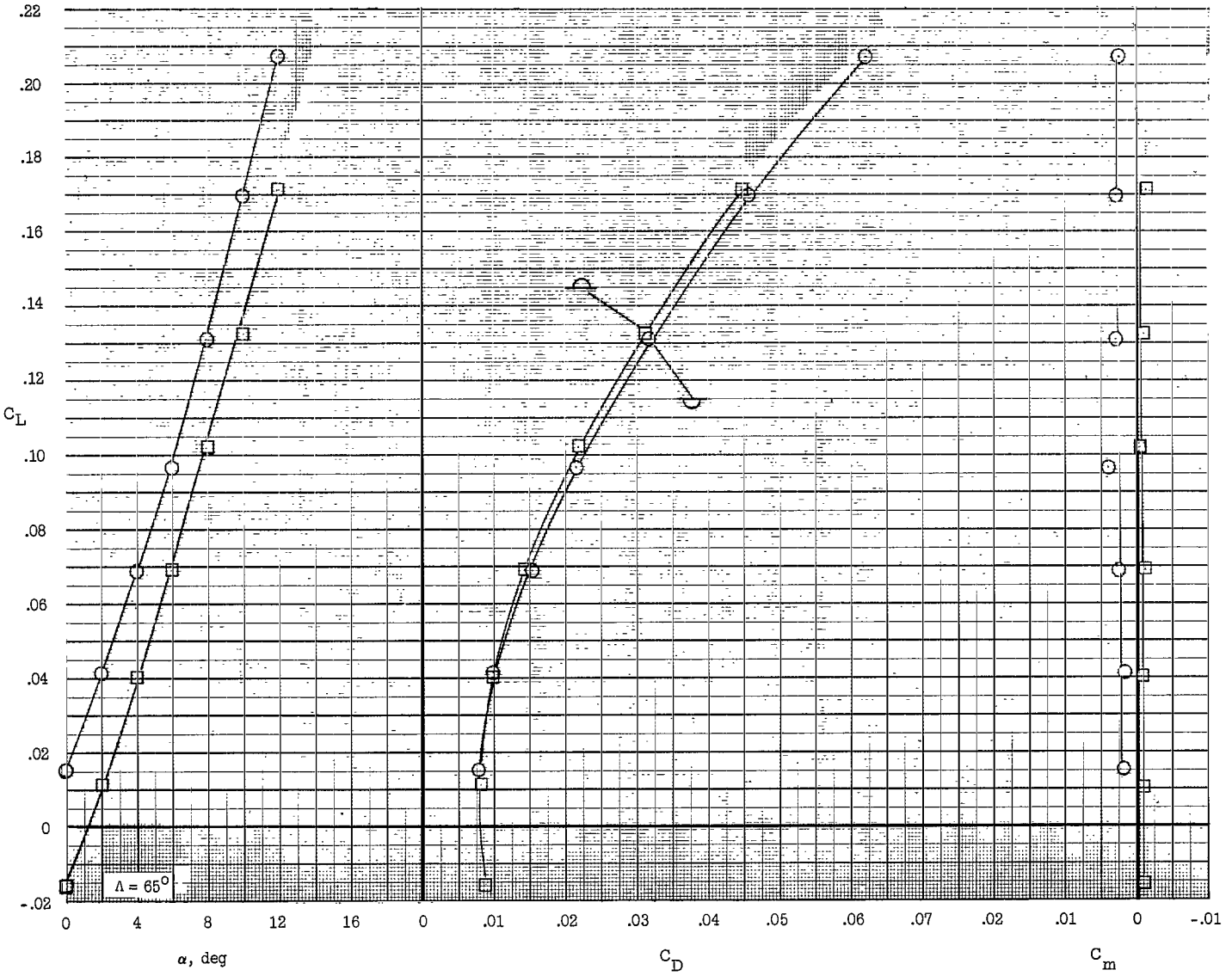

(d) Concluded.

Figure 16.- Continued.

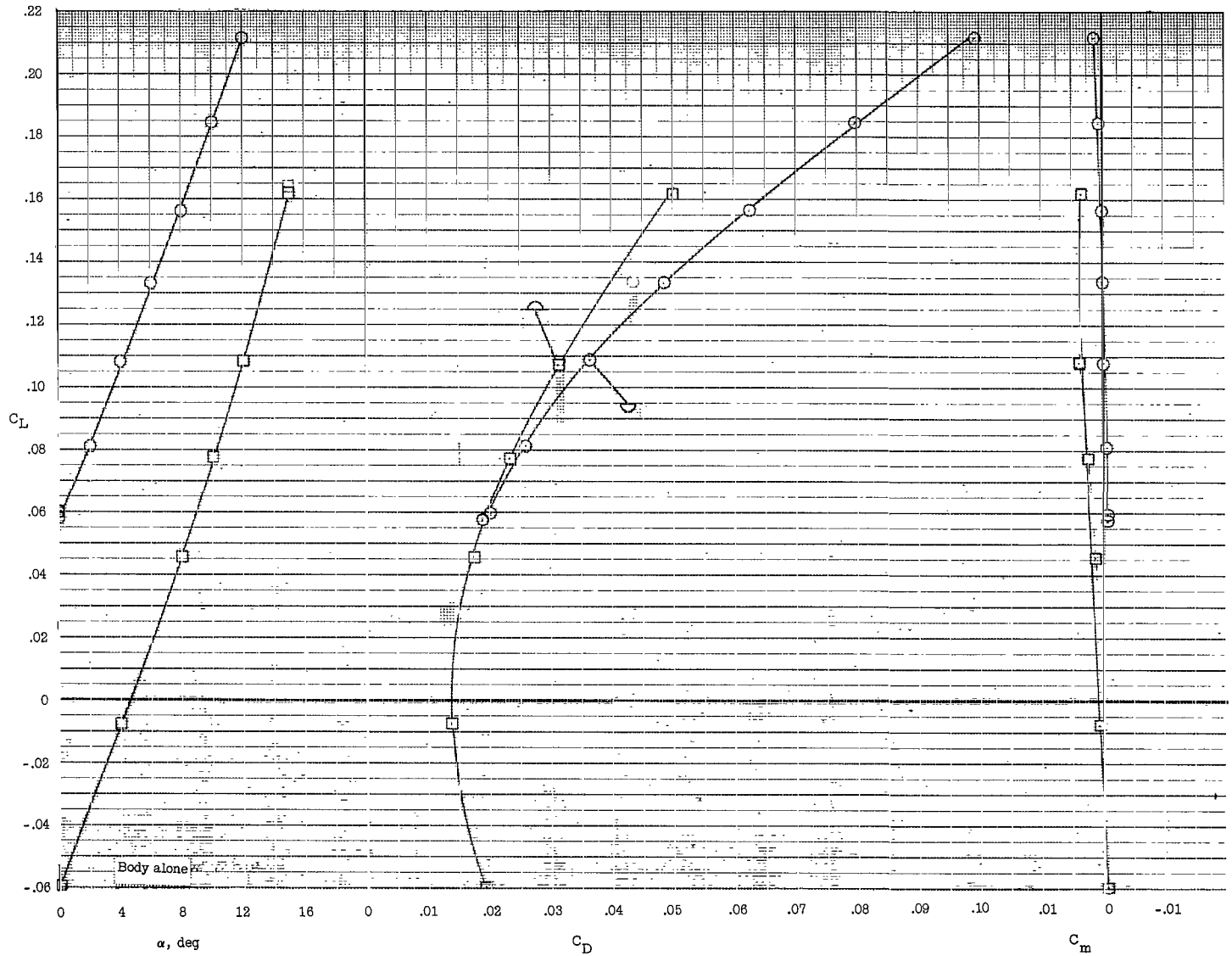

(e) $\theta = 9^\circ$.

Figure 16.- Continued

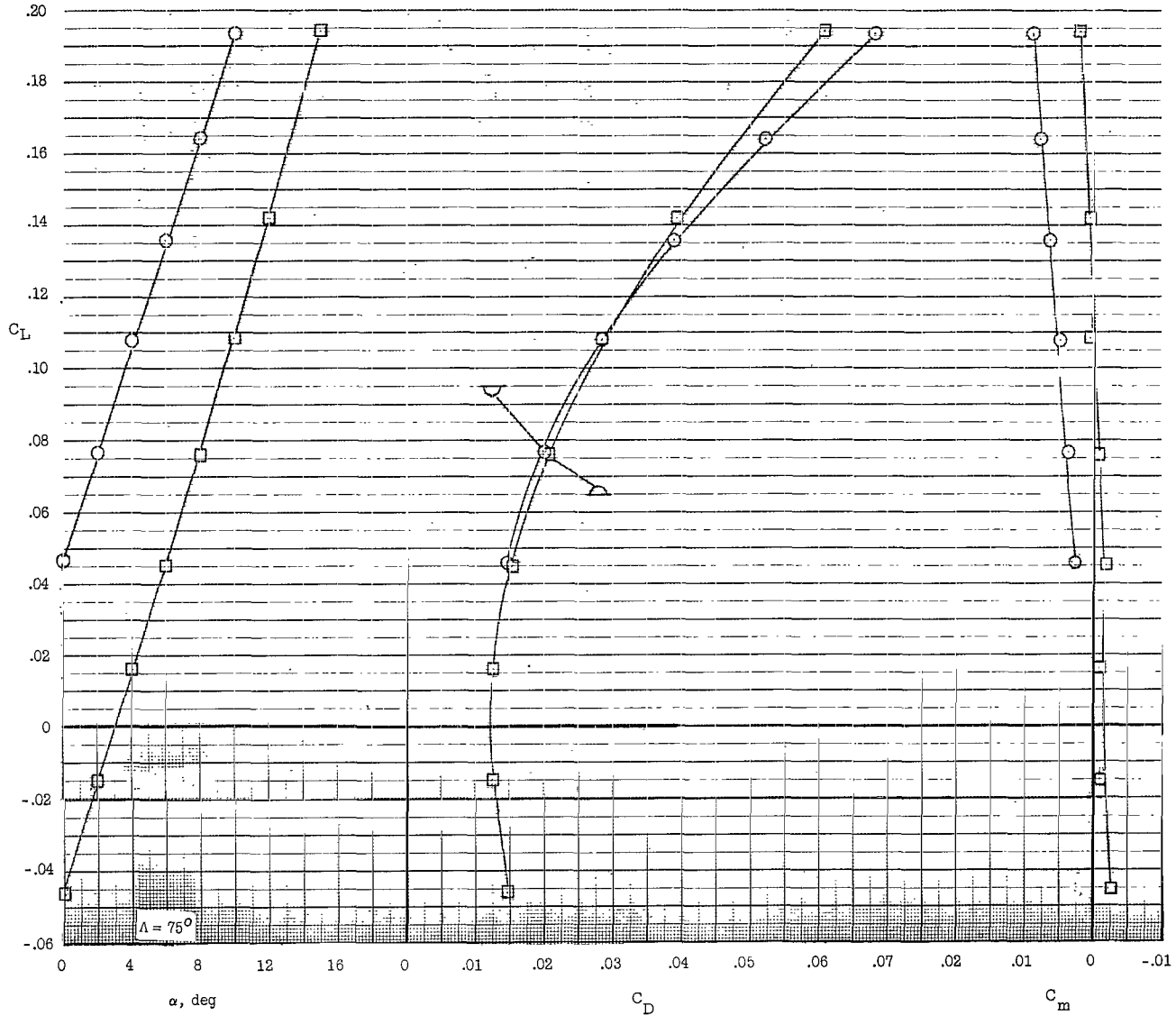

(e) Continued.

Figure 16.- Continued.

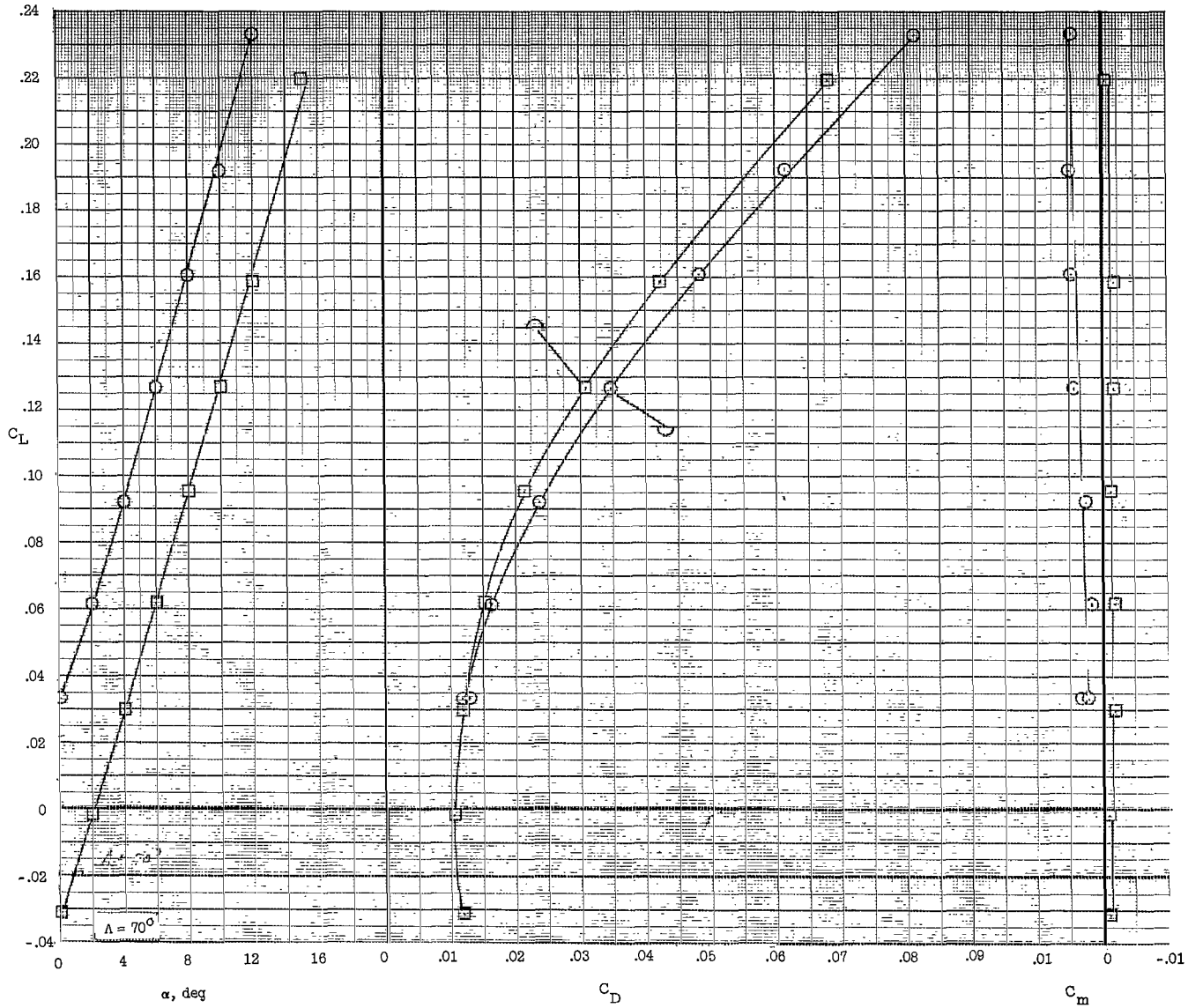

(e) Continued.

Figure 16.- Continued.

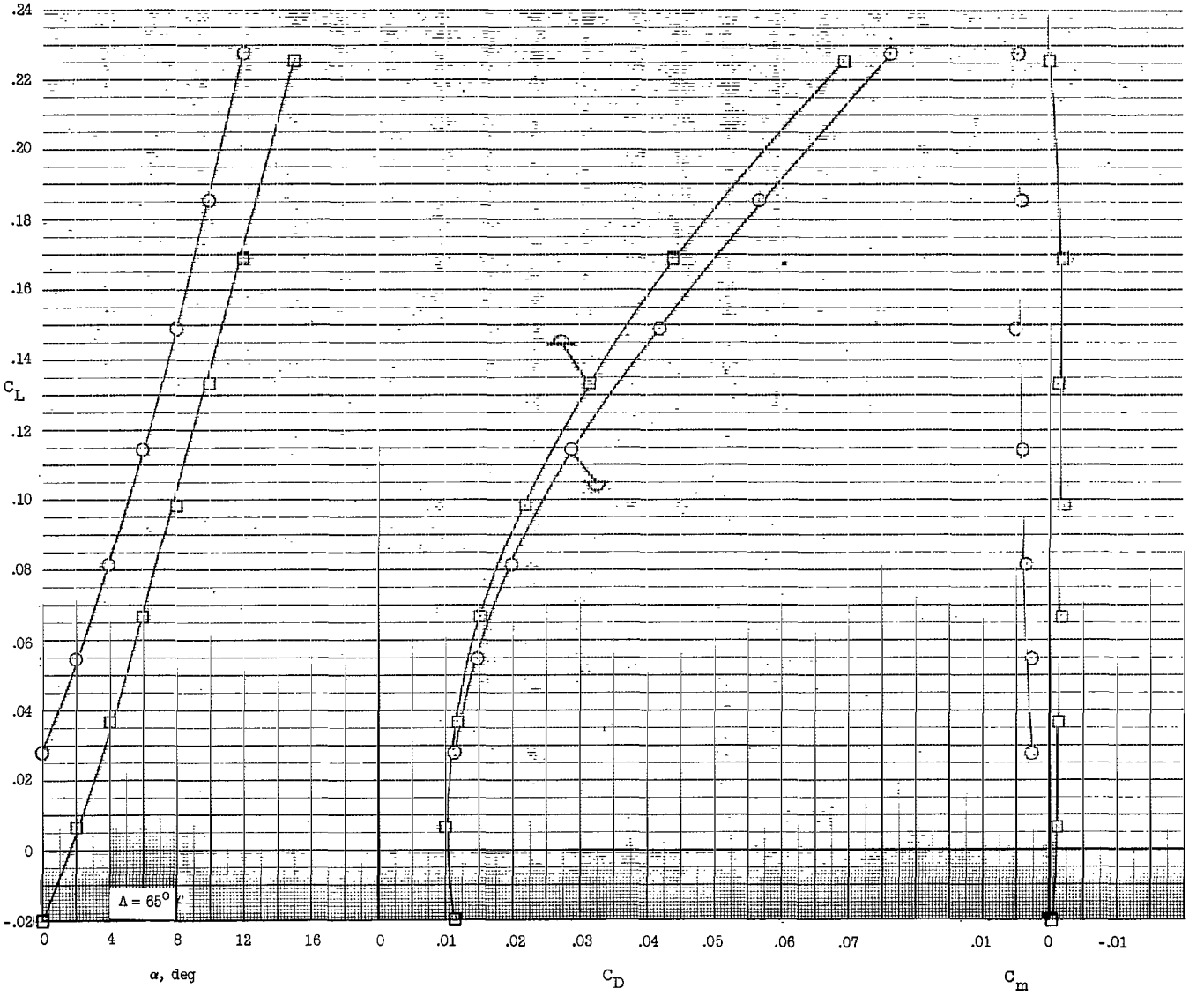

(e) Concluded.

Figure 16.- Concluded.

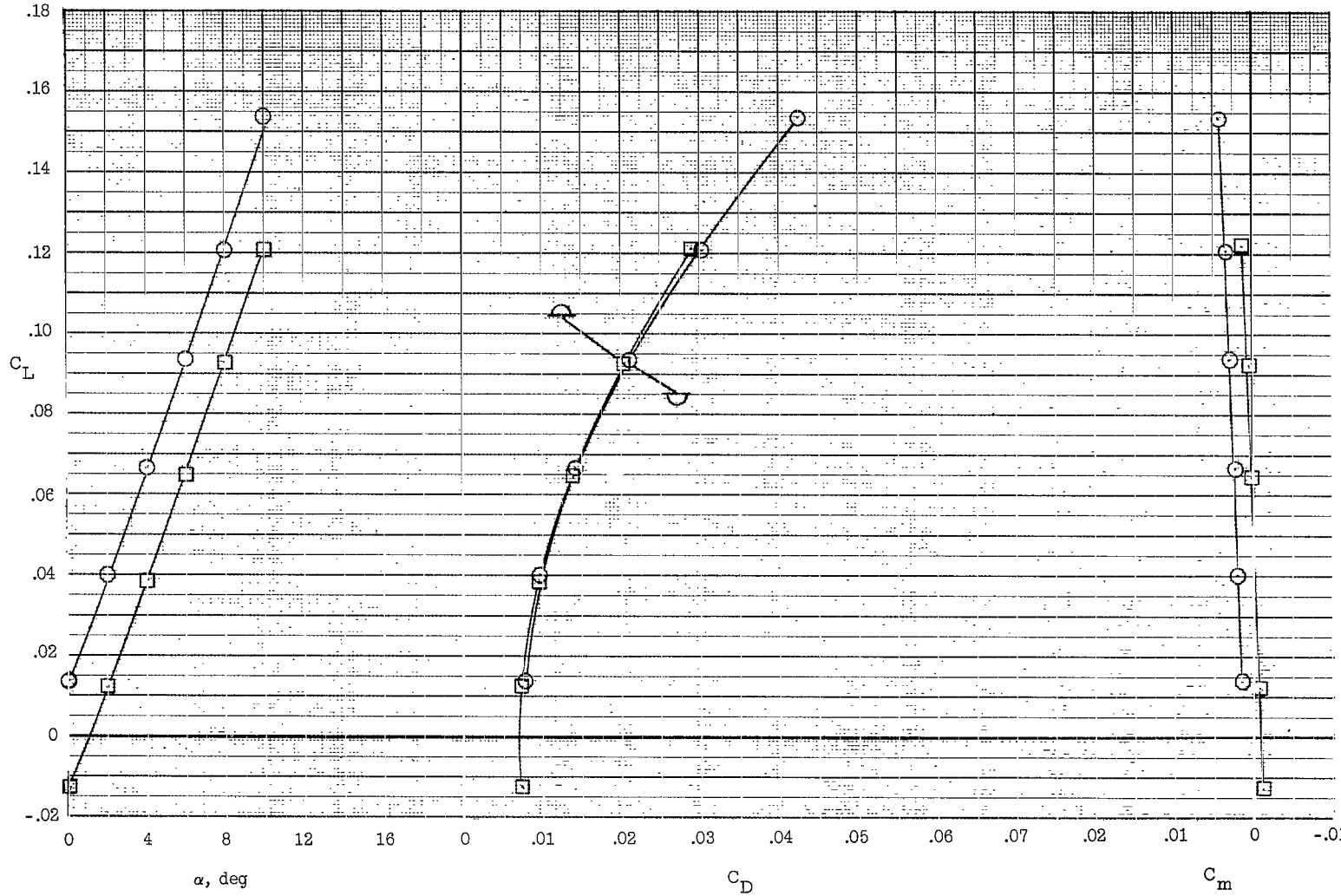

(a) $\tau = 1^\circ$.

Figure 17.- Aerodynamic characteristics of half-cone-wedge delta-wing configurations. $\Lambda = 75^\circ$.

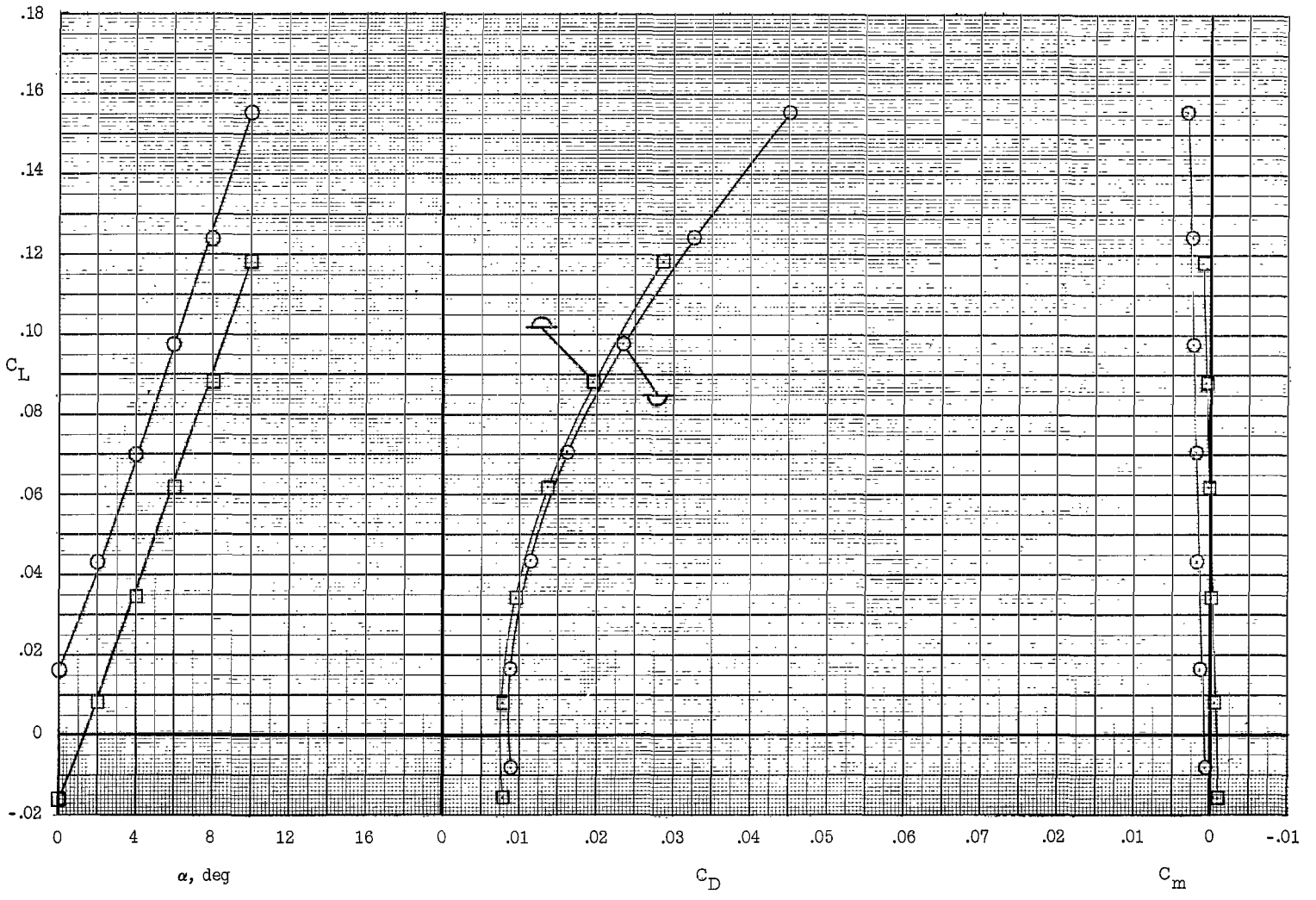

(b) $\tau = 2^\circ$.

Figure 17.- Continued.

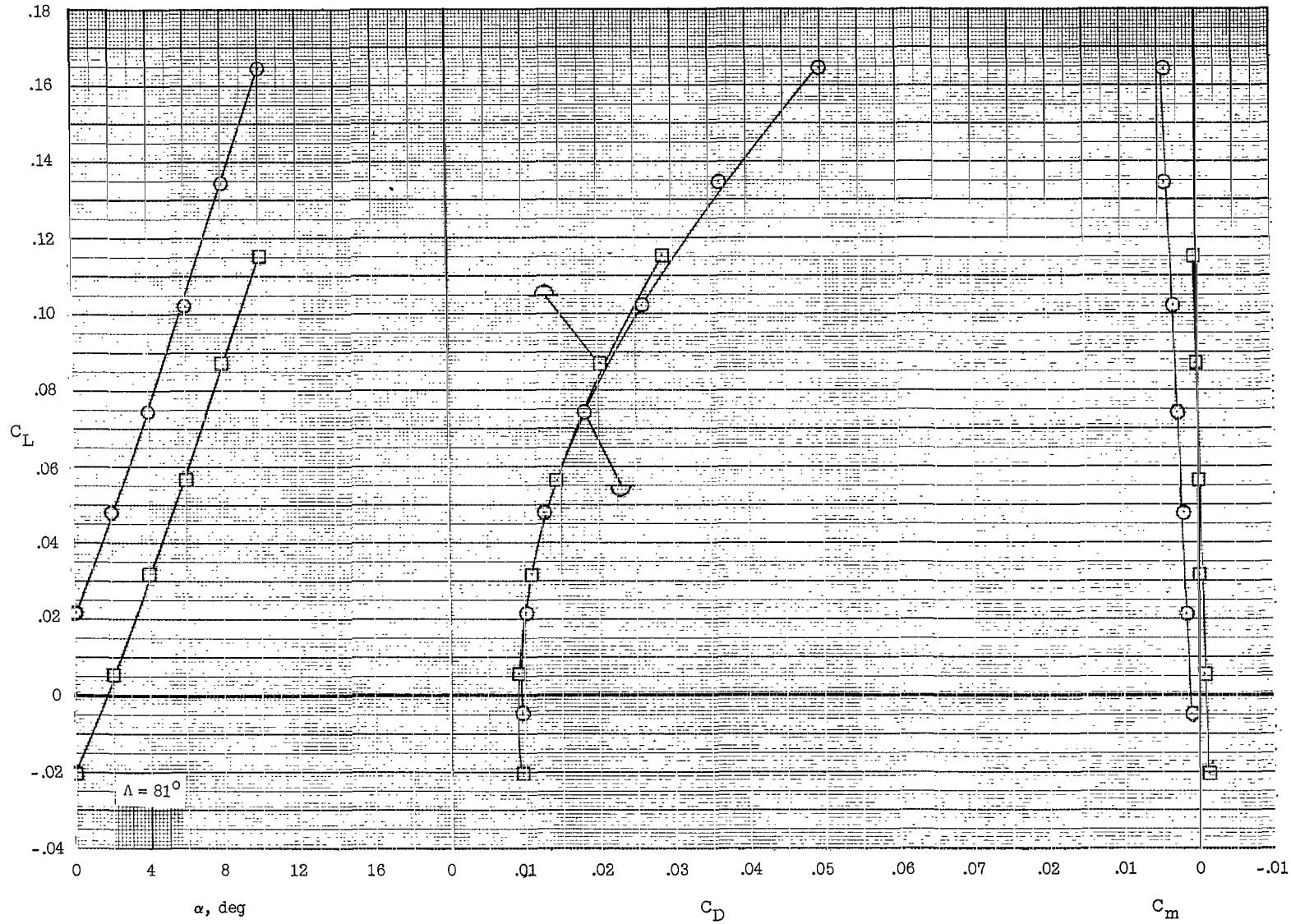

(c) $\tau = 3^\circ$.

Figure 17.- Concluded.

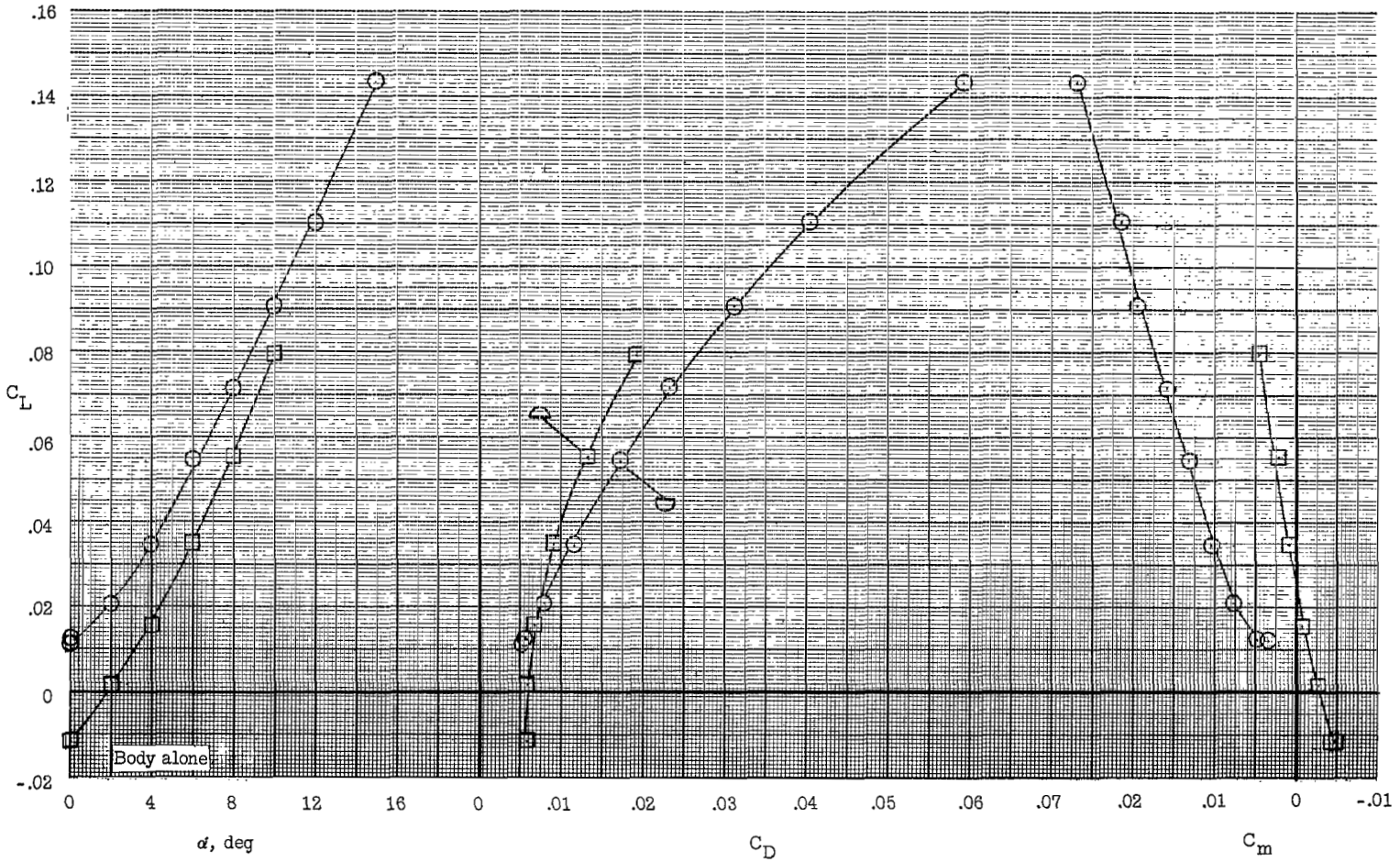

(a) $\theta = 6.05°$.

Figure 18.- Aerodynamic characteristics of half-cone-cylinder delta-wing configurations.

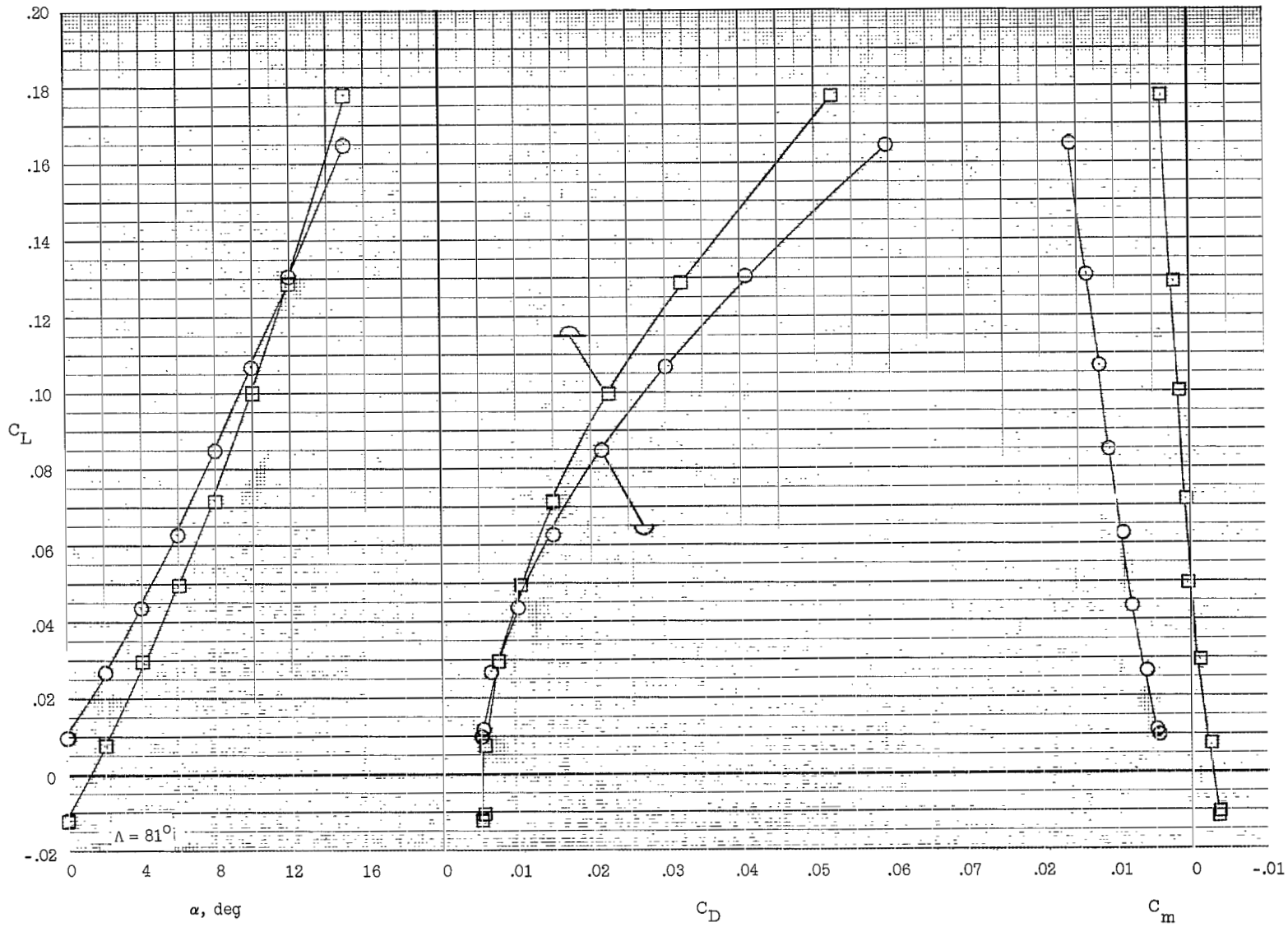

(a) Continued.

Figure 18.- Continued.

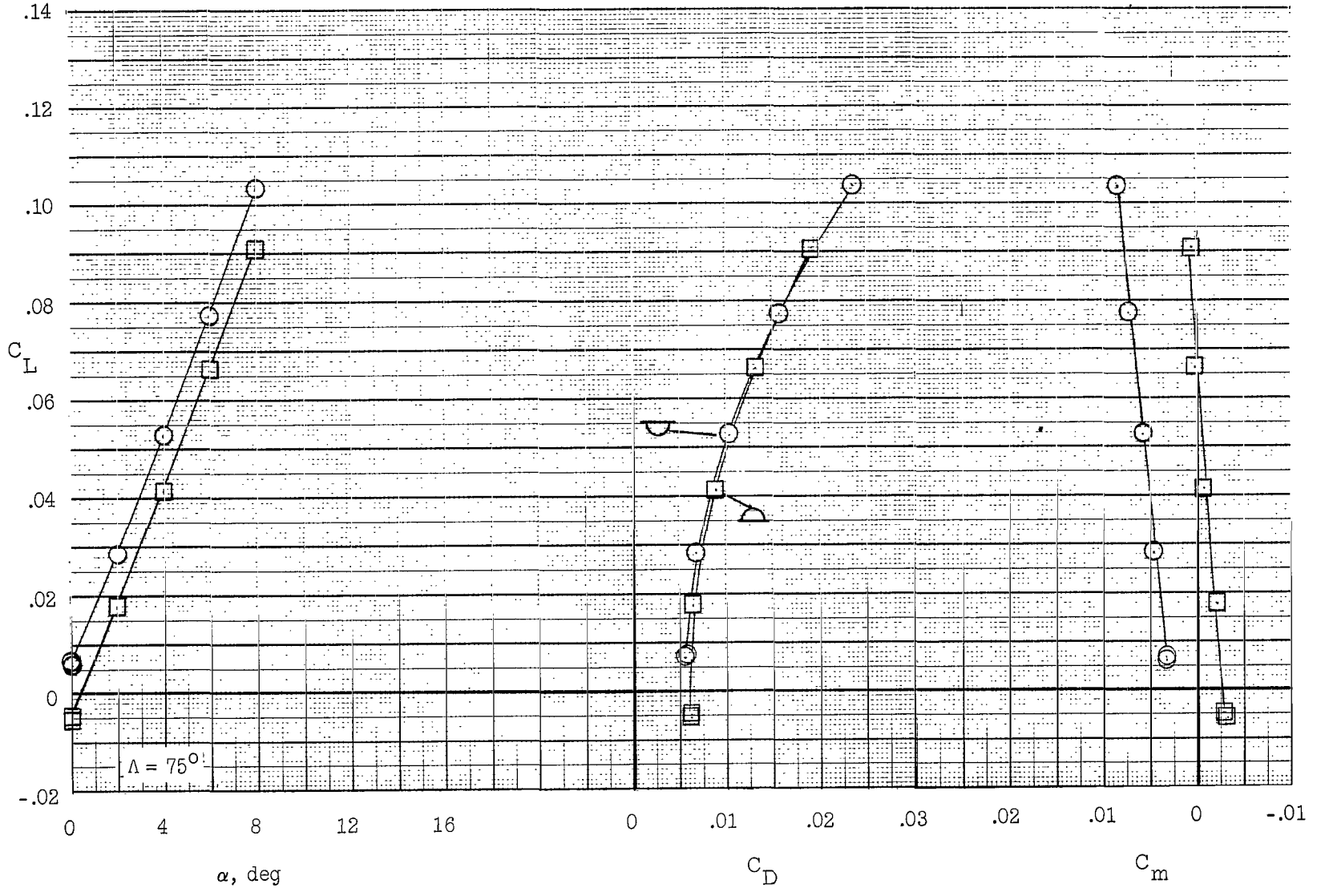

(a) Concluded.

Figure 18.- Continued.

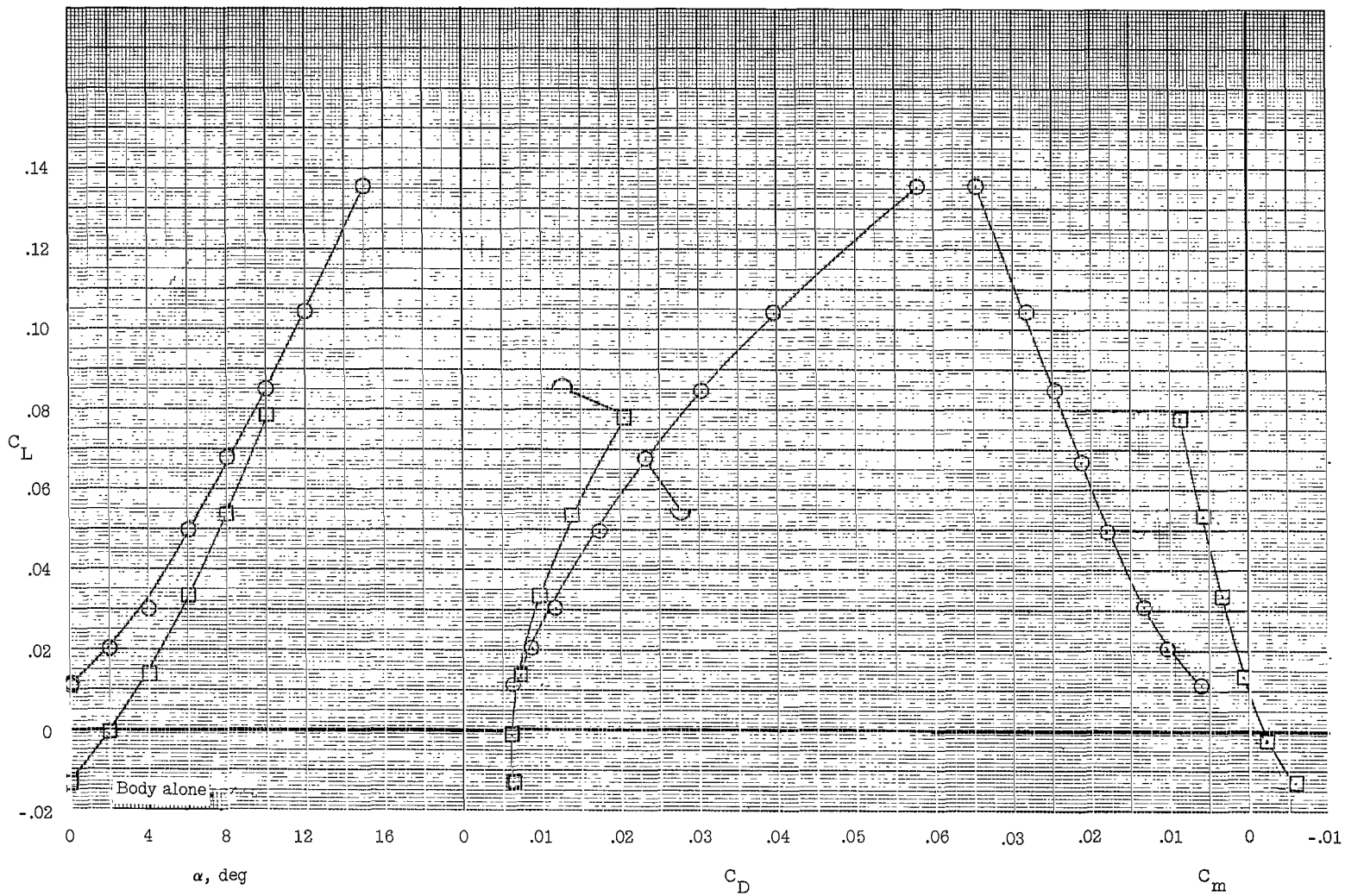

(b) $\theta = 7.06^{\circ}$.

Figure 18.- Continued.

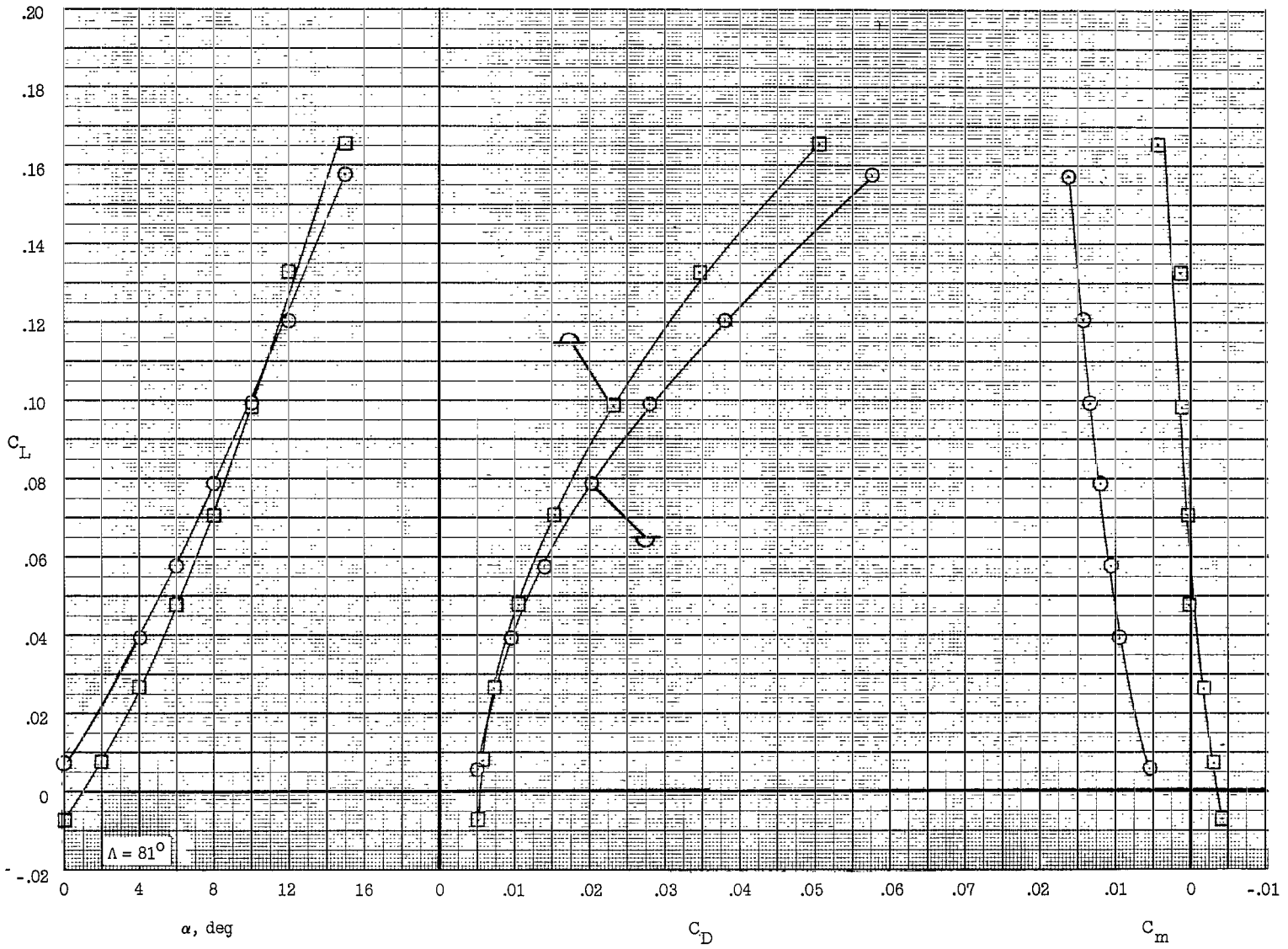

(b) Continued.

Figure 18.- Continued.

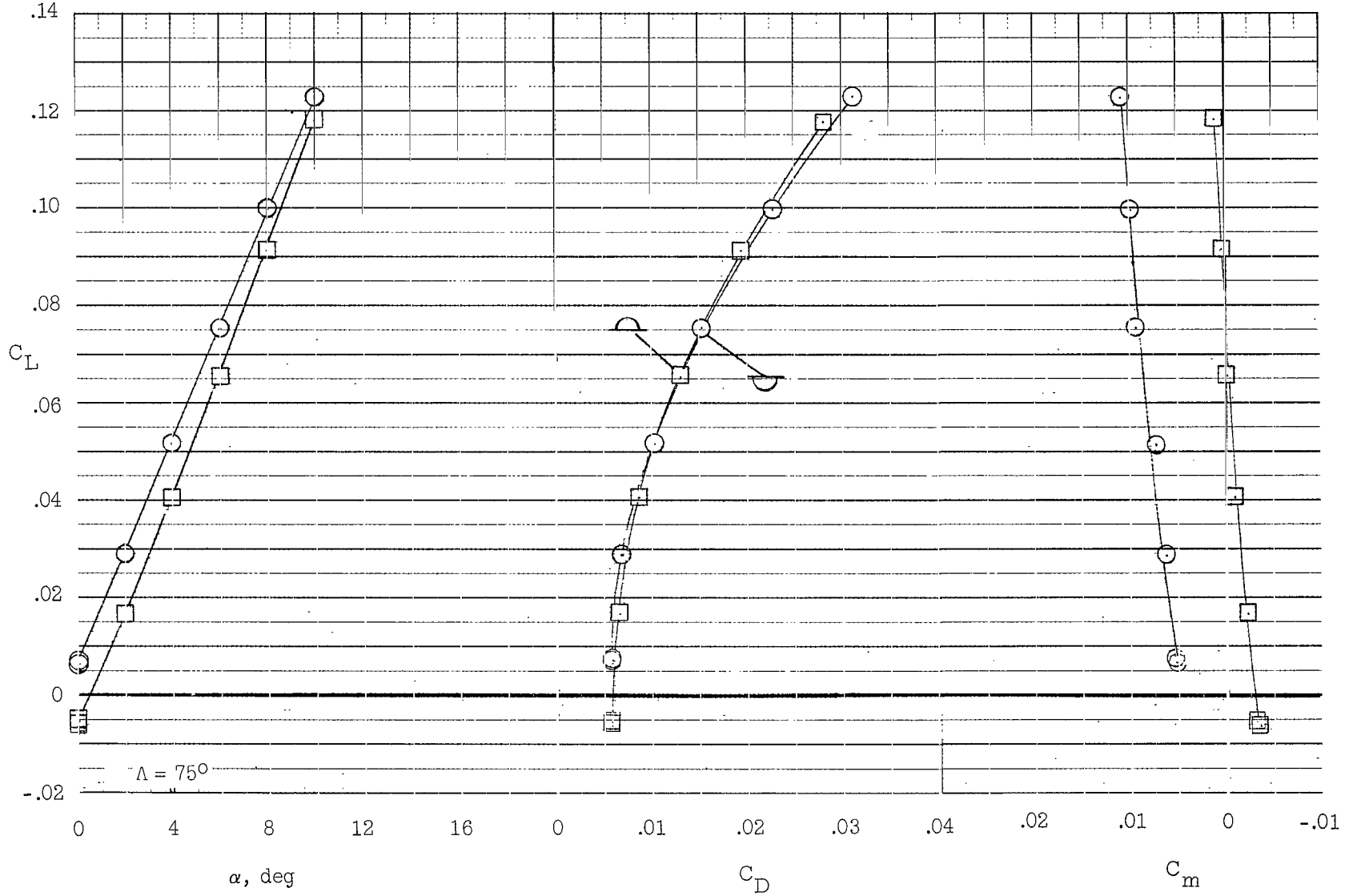

(b) Concluded.

Figure 18.- Continued.

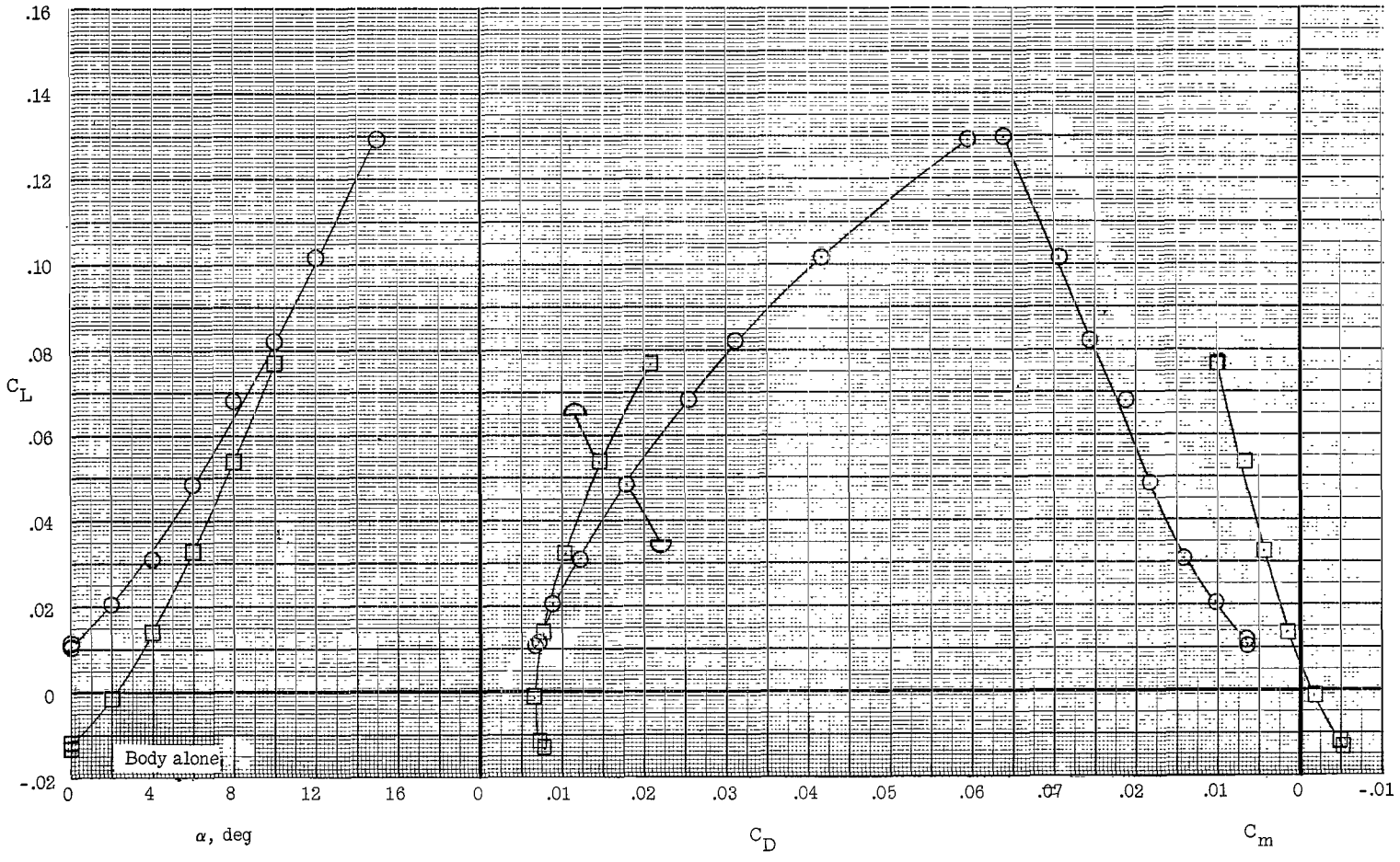

(c) $\theta = 8.49°$.

Figure 18.- Continued.

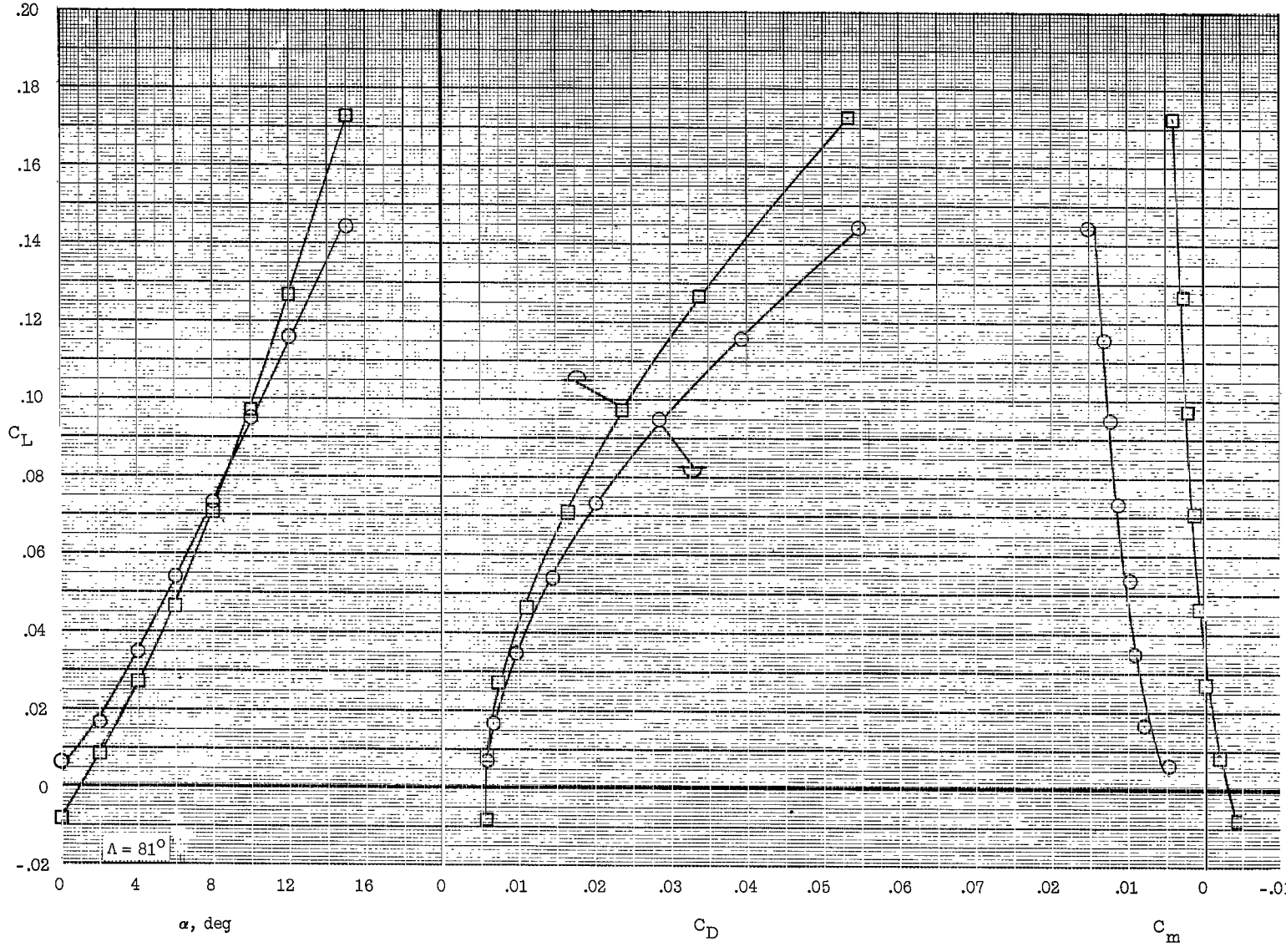

(c) Continued.

Figure 18.- Continued.

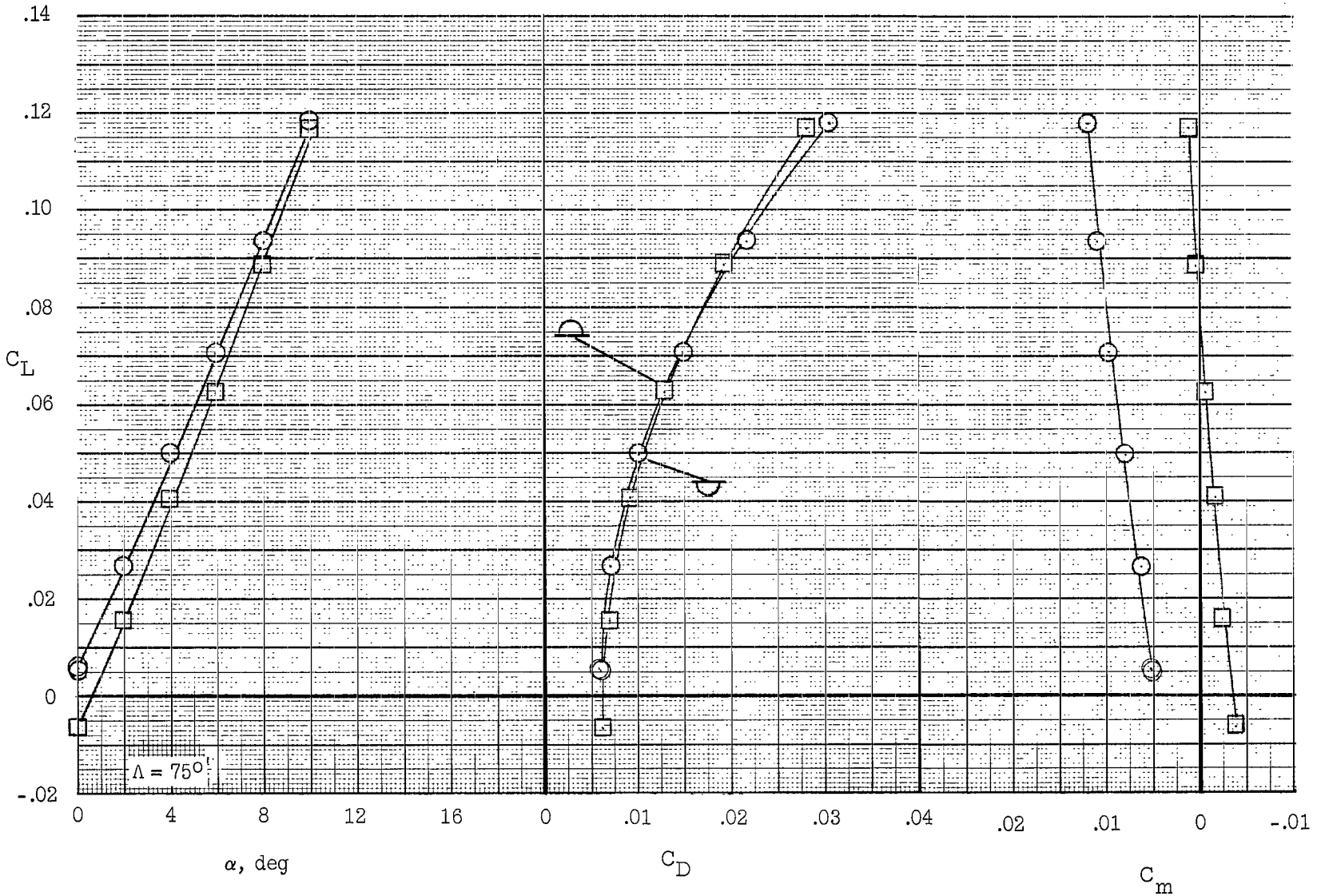

(c) Concluded.

Figure 18.- Continued.

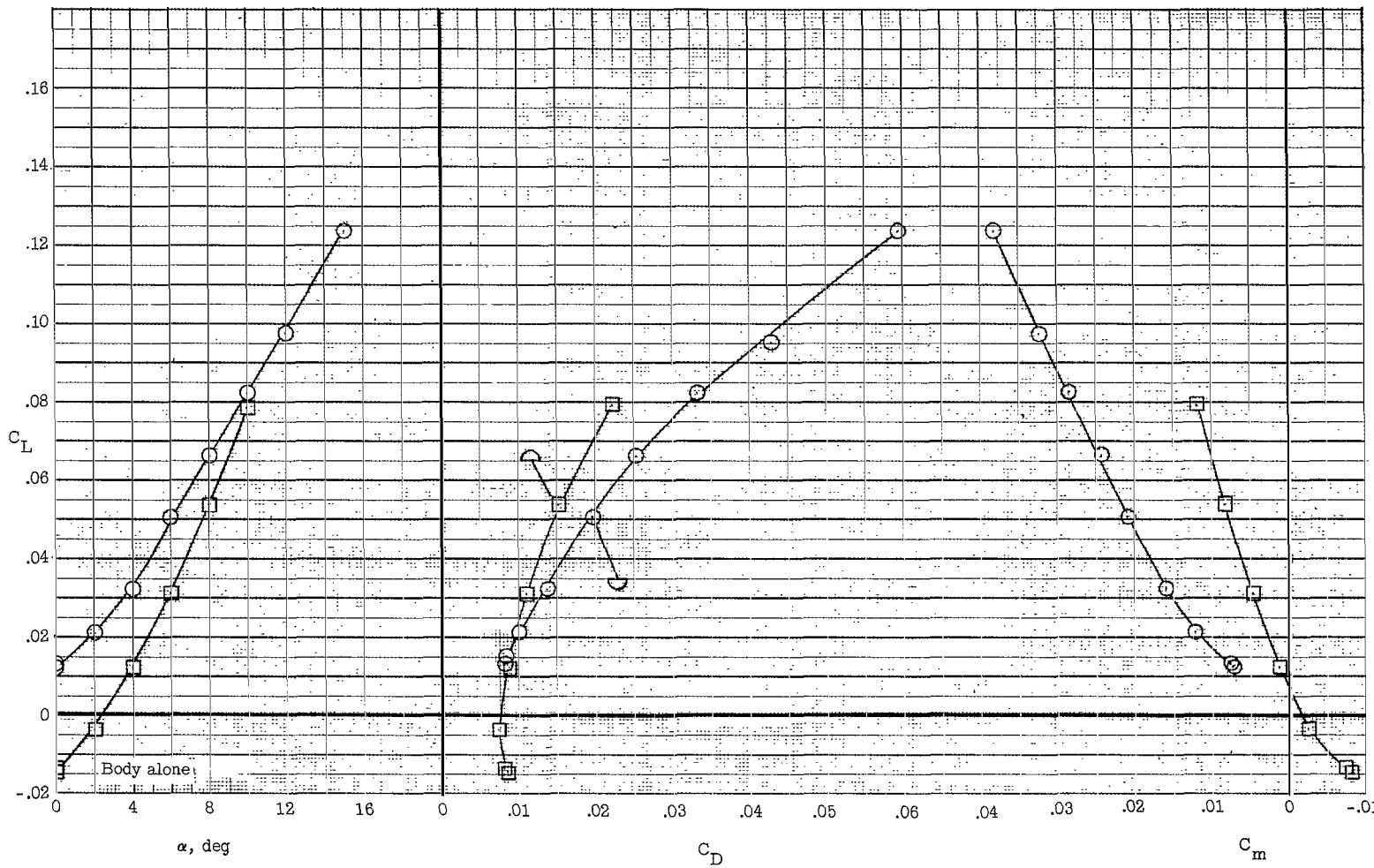

(d) $\theta = 8.85^{\circ}$.

Figure 18.- Continued.

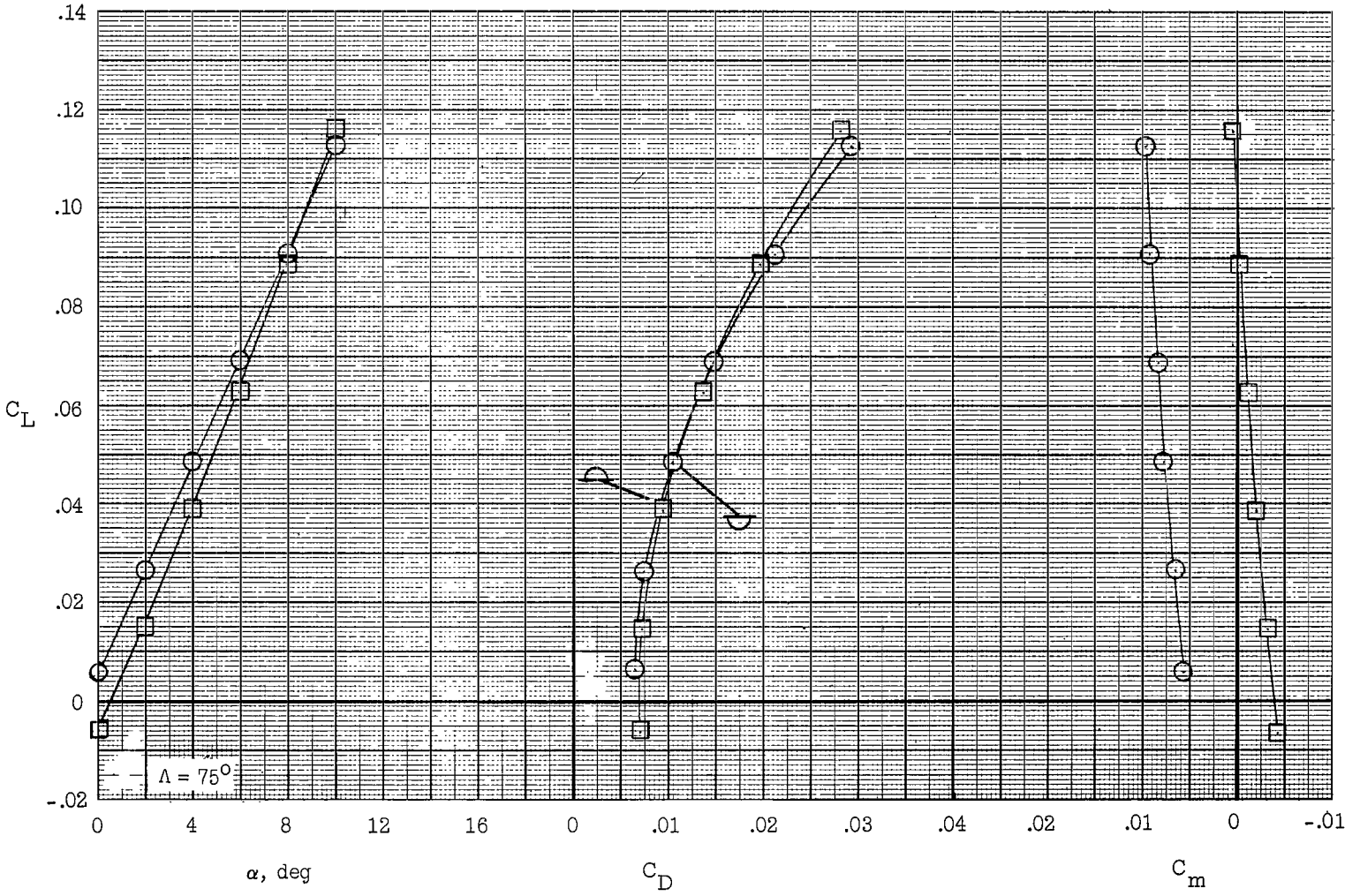

(d) Concluded.

Figure 18.- Concluded.

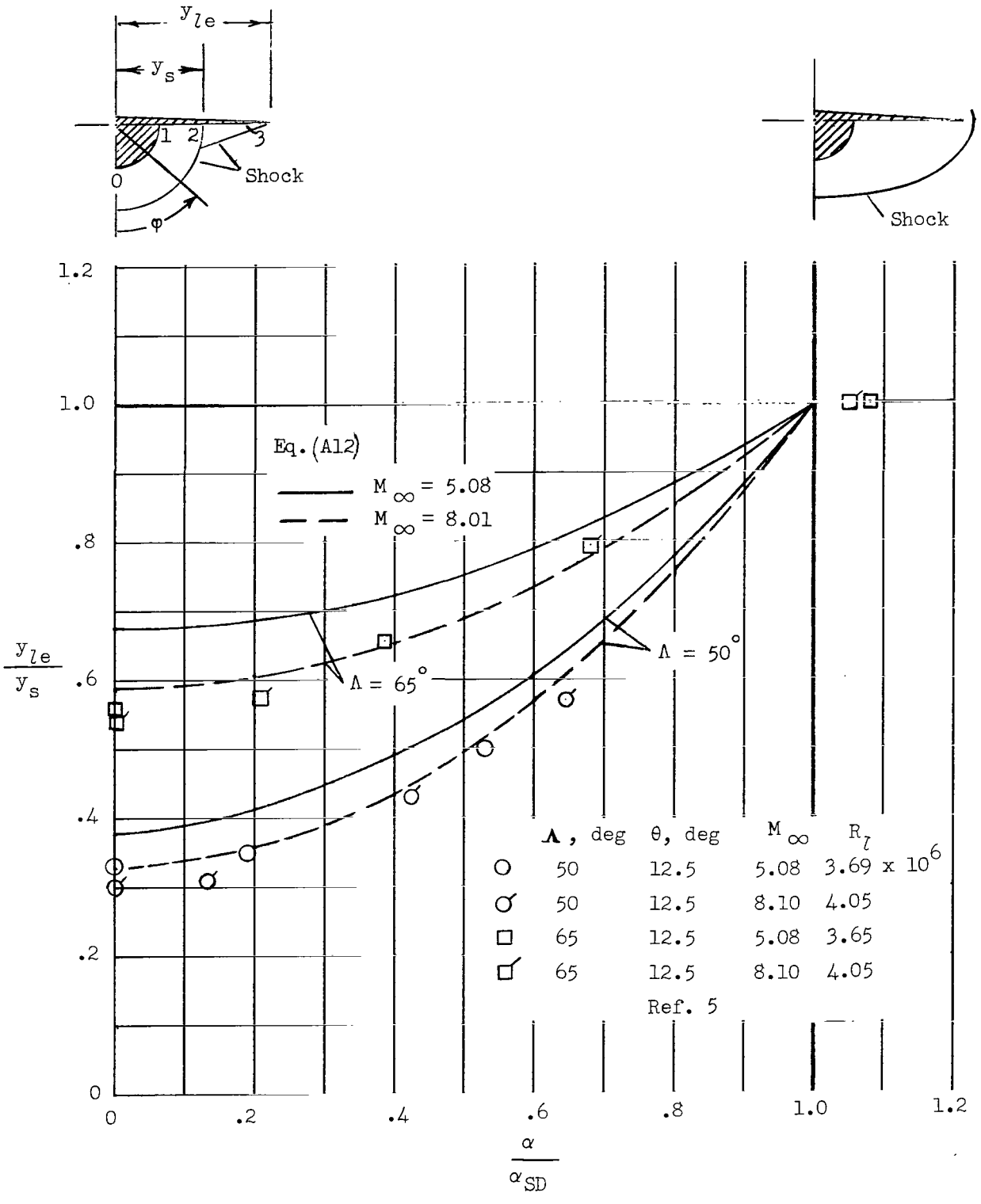

Figure 19.- Shock patterns about flat-top half-cone delta-wing configurations.

NASA-Langley, 1965 L-4377

2/22/05
50

"The aeronautical and space activities of the United States shall be conducted so as to contribute . . . to the expansion of human knowledge of phenomena in the atmosphere and space. The Administration shall provide for the widest practicable and appropriate dissemination of information concerning its activities and the results thereof."

—NATIONAL AERONAUTICS AND SPACE ACT OF 1958

NASA SCIENTIFIC AND TECHNICAL PUBLICATIONS

TECHNICAL REPORTS: Scientific and technical information considered important, complete, and a lasting contribution to existing knowledge.

TECHNICAL NOTES: Information less broad in scope but nevertheless of importance as a contribution to existing knowledge.

TECHNICAL MEMORANDUMS: Information receiving limited distribution because of preliminary data, security classification, or other reasons.

CONTRACTOR REPORTS: Technical information generated in connection with a NASA contract or grant and released under NASA auspices.

TECHNICAL TRANSLATIONS: Information published in a foreign language considered to merit NASA distribution in English.

TECHNICAL REPRINTS: Information derived from NASA activities and initially published in the form of journal articles.

SPECIAL PUBLICATIONS: Information derived from or of value to NASA activities but not necessarily reporting the results of individual NASA-programmed scientific efforts. Publications include conference proceedings, monographs, data compilations, handbooks, sourcebooks, and special bibliographies.

Details on the availability of these publications may be obtained from:

SCIENTIFIC AND TECHNICAL INFORMATION DIVISION

NATIONAL AERONAUTICS AND SPACE ADMINISTRATION

Washington, D.C. 20546